

# **Competing for the polarisation axis: implications for vascular remodeling**

Rui Augusto Barros Garcia

Thesis to obtain the Master of Science Degree in

## **Biomedical Engineering**

Supervisor(s): Prof. Susana Isabel Pinheiro Cardoso de Freitas

Dr. Vânia Cristina Henriques Silvério

### **Examination Committee**

Chairperson: Prof. Cláudia Alexandra Martins Lobato da Silva

Supervisor: Dr. Vânia Cristina Henriques Silvério

Members of the Committee: Dr. Sofia de Medina Aires Martins

**November 2017**









*“Se todos nós, Portugueses tivéssemos amor àquilo que fazemos,  
vivíamos num país de paraíso.”*

*quote by Augusto Moreira Ferreira Garcia*

*(de Jesus et al. 2012)*



# Acknowledgments

I would like to thank to my closest family and dear friends who supported me during this unusual and peculiar path.

To my parents for providing the education, values and love indispensable to the formation of character. To my lovely sisters who provided me delightful moments over the infancy and irreplaceable friendship for life. To Antero who has been a confident and a brother over the years. To the love of my life who has been a beacon in this recent past.

Abel, Filipa, Marta and Professor Luis Mira Vieira have showed unconditional support and friendship in this new critical stage of my life. To André, Carolina, Sofia, Miguel and Mafalda who have received me as one of their own and for the delicious and hard moments lived in academia. To Pedro and Ivo who have been invaluable friends and whose company I cherish.

For the INESC-MN family (Figure A.1) who provided a proficient environment and mutual aid during the internship. To Professor Susana Cardoso who nurtures this environment through regular meetings guiding the students thanks to her valuable hints and for the personal bet made. To Dr. Vânia Silvério that has been guiding my work and updating the work objectives diligently and pragmatically.

My special thanks to all of those who have shared this brief passage with me and enriched my life.



# Abstract

Angiogenesis or the formation of new blood vessels from existing ones plays a key role in physiological processes. Many existing pathologies are associated with its deregulation and the comprehension of the molecular mechanisms triggered in endothelial cells (EC) during angiogenesis remains an open field of research.

Blood flow and Vascular Endothelial Growth Factor (VEGF) have antagonist functions and modulate the polarity machinery of EC in retina angiogenesis to grow inwards and outwards, in the direction of the flow respectively. Franco hypothesize that Blood Flow and VEGF compete to determine the axis of polarization through Par3/Par6/aPKC (Par) complex. A microfluidic device was modelled and fabricated at INESC-MN Cleanroom facilities to test this hypothesis. The device simultaneously generates a VEGF gradient and a shear stress gradient, to evaluate the response of competing stimulus in cell polarization.

The influence of both shear stress and VEGF gradient on EC was simulated using a CFD commercial code. Averaged cross section velocities from  $0.1 \text{ mm} \cdot \text{s}^{-1}$  to  $20 \text{ mm/s}$  were imposed to the flow. As example, for an average cross velocity,  $U$ , of  $20 \text{ mm} \cdot \text{s}^{-1}$  the EC maximum shear stress for transient conditions was found to be  $2,5 \text{ Pa}$  and the transient regime establishment time in the VEGF gradient generator (GG) at the membrane pores was seen to be below  $4 \text{ s}$ .

The PDMS microfluidic device was fabricated by soft lithography and mechanically sealed. The experimental results determination of average flow velocity and concentration profile exhibited concordance with simulated.

## Keywords

Microfluidic Devices, Soft Lithography, Multi-Physics Simulation



## Resumo

A angiogénese ou criação de novos vasos sanguíneos a partir de vasos existentes desempenha um papel crucial nos processos fisiológicos. Várias patologias são associadas com a sua desregulação e a compreensão dos mecanismos moleculares despoletados nas células endoteliais (EC) durante a angiogénese permanece uma área de ativa investigação.

O fluxo sanguíneo e o fator de crescimento endotelial vascular (VEGF) possuem funções antagonistas e modulam a polaridade das EC na angiogénese da retina que crescem, respetivamente, para montante ou jusante. Franco (2016) propõe que o fluxo sanguíneo e VEGF modulam a direção de polarização através do complexo Par3/Par6/aPKC (Par). Foi fabricado e dimensionado um dispositivo microfluidico nas instalações de sala limpa do INESC-MN para testar esta hipótese. O dispositivo gera simultaneamente um gradiente de VEGF e um gradiente de tensão de corte que são estímulos antagonistas na polarização celular.

A influência de tensão de corte e gradiente de VEGF nas EC foi simulado com recurso a código comercial de CFD. As velocidades médias de escoamento impostas na secção foram de  $0,1 \text{ mm.s}^{-1}$  até  $20 \text{ mm.s}^{-1}$ . Para uma velocidade média da secção de  $20 \text{ mm.s}^{-1}$  a tensão de corte máxima encontrada foi  $2,5 \text{ Pa}$  e o tempo de estabelecimento de regime transiente para o gerador de gradiente de VEGF (GG) nos poros da membrana foi inferior a  $4 \text{ s}$ .

O dispositivo foi fabricado com recurso a *Soft Lithography* e selagem mecânica. A medição das velocidades médias da secção e do perfil de concentração exibiram concordância com as simulações.

## Palavras-Chave

Integração de Dispositivos Microfluídicos, Soft Lithography, Simulação Multi-Física





# Contents

Acknowledgments .....	iii
Abstract .....	v
Resumo .....	vii
Contents .....	ix
List of Figures .....	xi
List of Tables.....	xvii
List of Abbreviations and Symbols.....	xviii
1 Introduction .....	1
1.1 Research Motivation .....	1
1.2 Objectives.....	1
1.3 Thesis Outline.....	2
2 State of the Art .....	3
2.1 Anatomy and Angiogenesis.....	3
2.1.1 Eye Anatomy.....	3
2.1.2 Angiogenesis .....	4
2.2 Microfluidic Devices .....	8
2.2.1 Applications of Microfluidic Devices .....	8
2.2.2 Characterization of Microfluidic Devices.....	10
2.2.3 Mixing Techniques in Microfluidics.....	11
2.3 Microfabrication Techniques for Microfluidic Devices.....	12
2.3.1 Fabrication of elastomeric microfluidic devices .....	13
2.3.2 Bonding Techniques.....	17
2.4 Physical Principles of Microfluidics .....	19
2.4.1 Basic Concepts .....	19
2.4.2 Governing equations .....	23
2.5 Final Considerations .....	26
3 Materials and Methods.....	29
3.1 Microfluidic Device Overview.....	29
3.2 Microfluidic Technology.....	29
3.2.1 Mask Design .....	30
3.2.2 Hardmask patterning .....	32
3.2.3 PDMS molding .....	34
3.2.4 Replica Molding.....	36

3.3	Assembly Techniques .....	37
3.4	CFD Simulation.....	38
3.5	Experimental Setup.....	39
3.5.1	Generation of stable gradient using dye solution.....	39
3.5.2	Generation of a stable shear stress .....	41
3.6	Final Considerations .....	42
4	Results and Discussion.....	45
4.1	Microfluidic Technology.....	45
4.1.1	Hardmask patterning .....	46
4.1.2	PDMS Molding .....	47
4.1.3	Replica molding and Assembly.....	49
4.2	CFD Simulation.....	51
4.2.1	Pressure Balance.....	51
4.2.2	Characteristic Diffusion Time .....	52
4.2.3	Gradient Generator – Pore Diffusion.....	53
4.2.4	Gradient Generator - Mixer Efficiency .....	59
4.2.5	Shear Stress .....	63
4.3	Experimental Validation .....	70
4.3.1	Concentration gradient determination .....	70
4.3.2	Flow rate measurement.....	76
5	Conclusions and Future Work.....	79
6	References.....	83
A.	Annexes.....	87
	Group Photo.....	87
	Results and Discussion .....	88

## List of Figures

Figure 2.1 – (a) Structure of the human eyeball (Tortora et al. 2010). (b) Structure of the human and mice eyeball anatomy (Veleri et al. 2015). .....	3
Figure 2.2 – Genesis of vascular system (A – Vasculogenesis; B - Angiogenesis) (Lamallice et al. 2007).....	5
Figure 2.3 – Cellular mechanism of cellular sprouting (Herbert et al. 2012). .....	6
Figure 2.4 – (a) Schematic representation of pillar extension with three different results. (b) Intussusceptive pillars in the CAM imaged with scanning electron microscopy and confocal microscopy. (c) Finite element models of bifurcating vessels in the chick CAM where pillar extension emerged in low shear stress zone (De Spiegelaere et al. 2012). .....	7
Figure 2.5 – (a) Major steps of EC migration and (b) major signaling events associated to each step (Lamallice et al. 2007). .....	8
Figure 2.6 – Commercially available microreactors solutions. (a) 5-layer glass micro reactor from Micronit (2017). (b) Microreactor explorer kit from Sigma-Aldrich (2017). .....	9
Figure 2.7 -Commercially available microfluidic analytics solutions. (a) Vetscan LOC rotor based blood analyzer from Abaxis (1995). (b) LOC in-vitro molecular diagnostics from Magnumics (2013). .....	9
Figure 2.8 – (a) Schematic illustration of integrated microfluidic device composed by microbioreactors, breadboard, reservoir, bubble trap, physical sensors, and electrochemical biosensors. (b) Photograph of the PDMS integrated microfluidic device (B).(Zhang et al. 2017) .....	10
Figure 2.9 – Schematic of the (a) side view, (b) vertical sectional view and (d) perfusion system of the liver-on-a-chip. (c) Photograph of the channel with the PCL material. H. Lee and Cho (2016) .....	10
Figure 2.10 – (i) Stream splitting and recombination technique (Lin et al. 2015). (ii) Staggered herringbone mixer (SHM) created by Kwak with detailed pattern structures and flow directions (a), mixing quality over 2.5 cycles on SHM for different conditions (b) and top view images of SHMs efficiency after 1 cycle (c) (Kwak et al. 2016). .....	11
Figure 2.11 – (i) Schematic diagram of a single micro stirrer in the fluidic device (Ryu et al. 2004). (ii) T-junction with two pulsatile inlets with 90° phase difference simulation (a) and experimental results (b) (Ward et al. 2016). (iii) Schematic of the reversible optofluidic mixer with no mixing when ultraviolet (UV) is off (a) and mixed at the presence of UV due to the photosensitive water turns into the droplets, causing the mixing between two oil phases (b) (Venancio-Marques et al. 2013). .....	12
Figure 2.12 – Chemical structure of PDMS. ....	13
Figure 2.13 – Hardmask (glass substrate with thin flim layer of Aluminium), master mold (silica substrate with SU-8 PR layer) and PDMS microfluidic device. (Silverio et al. 2017) .....	14
Figure 2.14 – Pattern transfer with photolithography: (a) deposition of functional layer; (b) coating photoresist (positive or negative); (c) photolithography (dark field mask or clear field	

mask); (d) developing photoresist; (e) selective etching; (f) structure is transferred to functional layer (Nguyen et al. 2002). .....	15
Figure 2.15 – Fabrication of the master mold by photolithography. (Silverio et al. 2017).....	16
Figure 2.16 – Schematic of fabrication steps adopted in replica molding. (Silverio et al. 2017) .....	16
Figure 2.17 – Microfluidic devices require bonding / sealing of components, connection to pumping peripherals and electrical connection to actuators or sensors (Temiz et al. 2015). ....	17
Figure 2.18 – (a) PDMS on Glass microfluidic device for local delivery of a protein solution in a confined surface (Temiz et al. 2015). (b) Hybrid SU-8/PDMS self-assembling flexible microfluidic device at middle (Jamal et al. 2011). (c) Insertion of tubings in molded PDMS layers on a DNA purification chip at right (Hong et al. 2004).....	18
Figure 2.19 – (a) Mechanical lock based contact with electric socket at left (Yang et al. 2003). (b) Elastomeric frame with vacuum manifold at tubings inlet (Cooksey et al. 2009). ....	18
Figure 2.20 – (a) Reversible sealing by magnetic clamping (Tkachenko et al. 2009). (b) PDMS sealing of overflow microfluidics achieved by selective surface wettability (Ruiz et al. 2012). ...	19
Figure 2.21 - Bernoulli's law: energy conservation along a streamline. P is the pressure, and U is the velocity (Berthier et al. 2006). .....	20
Figure 2.22 - Different patterns of laminar and transitional flows behind a cylinder (Berthier et al. 2006).....	21
Figure 2.23 – Velocity profile in rectangular duct (Berthier et al. 2006). .....	21
Figure 2.24 - A sketch of the current density field $\rho v$ flowing through an arbitrarily shaped region. Any infinitesimal area $da$ is associated with an outward pointing unit vector $n$ perpendicular to the local surface. The current through the area $da$ is given by the product of $da$ and the projection $\rho v \cdot n$ of the current density on the surface unit vector. (Adapted from (Bruus 2007)). .....	25
Figure 3.1 – Individual component systems of the microfluidic device: (a) Shear Stress generator (SS), (b) PETE membrane and (c) Gradient Generator (GG). (d) Global view of microfluidic device reversible setup. (e) Section view of microfluidic device reversible assembly. (f) Section view of GG microfluidic device irreversible assembly. ....	30
Figure 3.2 – Top view of GG mask schematic, at left global view, at top right middle inlet detail and at bottom right column spacing detail. ....	31
Figure 3.3 – Top view of SS mask schematic, at left global view, at top right column spacing detail and at bottom right outlet detail. ....	32
Figure 3.4 - Disco DAD 321 Dicing Saw (DISCO™ 2011). and 5 * 5 cm <sup>2</sup> glass sample at right. (c) MKC ultrasonic baths MKC22. (Guyson™ 2017). ....	32
Figure 3.5 – (a) Nordiko 7000 broad ion milling system (Nordiko™ 2014). (b) Dektak 3030 profilometer at right (Dektak™ 2001). ....	33
Figure 3.6 – (a) Vacuum Bake/Vapor Prime System, Yield Engineering Systems (Yield Engineering Systems™ 2017). (b) SGV 88 series track system C&D Semiconductor Services	

(C&D Semiconductor Services™ 2017). Direct Writer Laser (DWL) lithography 2.0 system Lasarray, (c) global view and (d) sample holder in detail. ....	33
Figure 3.7 – (a) Wet bench in clean room. (b) Olympus BH3-MJL optical microscope (Olympus™ 2000) .....	34
Figure 3.8 – (a) JeLight UV cleaning machine 144AX (JeLight™ 2015). (b) Stuart digital hotplate SD160 (Stuart™ 2017). (c) FASTER BSC-EN laminar flow hood (FASTER™ 2017)...	35
Figure 3.9 – (a) Laurell WS-650-23 Spin Coater at left (Laurell™ 2017). (b) MicroChem SU-8 50 (MicroChem™ 2000). ....	35
Figure 3.10 – (a) UV 800W Curing Flood Lamp from UV technology limited (UV-light Technology™ 2017). (b) Sigma-Aldrich Poly(glycidyl methacrylate) (Sigma-Aldrich™ 2017). (c) Profilometer – Tencor Alpha Step 200 at right (Tenkor™ 2015). ....	36
Figure 3.11 – (a) Scientech laboratory balance SA-80 (Scientech™ 2017). Sylgard® 184 Pack with elastomer (b) curing agent (Dow Corning™ 2017b) and (c) silicone elastomer base (Dow Corning™ 2017a). ....	36
Figure 3.12 – (a) Bel-Art vacuum desiccator (Bel-Art™ 2017). (b) Memmert Universal Oven (Memmert™ 2007). ....	37
Figure 3.13 – (a) Schematic of micromilling fabrication processes. (adapted from Silverio and Freitas 2018). (b) Micromilling machine of INESC-MN. ....	37
Figure 3.14 – (a) SterliTech PETE Membrane Filters ((SterliTech™ 2017)). (b) Harrick Plasma Cleaner PDC 002 (Harrick Plasma™ 2017). ....	38
Figure 3.15 –(a) Rayner's blue concentrated dye (Rayner's™ 2011). (b) Olympus XC30 camera (Olympus™ 2017) coupled with inverted microscope model from Olympus. (c) Syringe pump from NE-300 SyringePump.com (SyringePump.com™ 2017). ....	39
Figure 3.16 – (a) Schematic illustrating the standard experimental setup for GG microfluidic device at left. (b) Images taken with microscope field of view at right. ....	40
Figure 3.17 – Experimental setup for the gradient generation determination, microfluidic device zoomed at left and global overview at right. ....	41
Figure 3.18 – Experimental setup for flow estimation in Shear Stress Generator with dimensions $4500 \times 100 \mu m^2$ . ....	42
Figure 3.19 – Experimental setup for flow estimation in Shear Gradient Generator with dimensions $3000 \times 100 \mu m^2$ . ....	42
Figure 4.1 – Top view of microfluidic device. The hydraulic circuit model simplification is defined by section of the Microfluidic device. In red GG sections, in grey the SS sections and in yellow the PETE membrane. ....	45
Figure 4.2 – (a) Microfluidic technology auxiliary components (Hardmask, SU-8 mold and PDMS microfluidic device) for SS. (b) Hardmask, SU-8 mold and PDMS microfluidic device for GG. ....	46
Figure 4.3 – Al deposit in glass substract. ....	46
Figure 4.4 – Glass substract after photolithography and some structure details at optical microscope for GG (a) and SS (b). ....	47

Figure 4.5 – Glass substract after aluminium wet etching and some details at optical microscope respectively for GG (a) and SS (d). Hardmask after photoresist strip and some details at optical microscope respectively for GG (b) and SS (e). Hardmasks final aspect respectively for GG (c) and SS (f). .....	47
Figure 4.6 – Profilometer measurement in GG sample at left. Profilometer tip in SS sample structure border at middle. GG sample detail on the mixer area at right. ....	48
Figure 4.7 – (a) PDMS scaffold composed by SU-8 mold and pocketed PMMA plate. GG (b) and SS (c)SU-8 resist molds on Si substrate coupled with PMMA plate. ....	49
Figure 4.8 – (a) Schematic on the last version of PMMA holder with microfluidic device. Top view of the (b) initial version and (c) Last version of PMMA holder. ....	49
Figure 4.9 – Top view of the PMMA microfluidic device holder ((a) – bottom plate, (b) – Middle plate, (c) – Top plate). The plates have through holes for bolt tightening and only the top plate has access holes for microfluidic device inlets and outlets. ....	50
Figure 4.10 – (a) First version of microfluidic device with major leakage. (b) Third and last version of microfluidic device with minor leakage issues. ....	50
Figure 4.11 – (a) Side view schematic of the GG PDMS structures bonding to PETE membrane (b) SS PDMS structure bonded to PETE membrane and glass substrate. (c) GG PDMS structure bonded to PETE membrane and glass substrate at right. ....	51
Figure 4.12 – (a) Side view of GG and membrane detail in red. (b) Travelling distances scheme of $x_1$ and $x_2$ in GG schematic. (c) Travelling times scheme of $t_{1c}$ and $t_{2d}$ for a mixed transport ruled initially by convection and afterwards by diffusion in GG. (d) Travelling time scheme of $t_{1d} + 2d$ for a mixed transport ruled by diffusion in GG. ....	53
Figure 4.13 - Top View of Gradient Generator (Left – Zoom In   Right – Global).....	54
Figure 4.14 – (a) Side View schematic and zoom in of GG with PDMS system, PETE membrane and glass surface where the channel saliences represent the membrane pores (b) 3D View of GG CFD model and boundary conditions. ....	56
Figure 4.15 – Computation of the overall diffusion time at the membrane pore. The “particle arrival times” are the times required to guaranty 95% of concentration in the paths inlet-bottom channel $t_1$ , pore top- pore bottom $t_2$ and inlet-pore bottom $t_{comp}$ . ....	57
Figure 4.16 – Vertical velocity profile at GG mid channel using numerical approximation (White 1991) at left. Velocity field on the model region of interest at middle. Vertical velocity profile at GG at the model inlet, mid-section and outlet comparison with imposed conditions at right. Note that the previous results considered a profile mean velocity of $20\text{ mm.s}^{-1}$ . ....	57
Figure 4.17 – Pressure surface on the model region of interest at left. Vertical velocity profile at GG at the model inlet, mid-section and outlet comparison with imposed conditions at right. Note that the previous results considered a profile mean velocity of $20\text{ mm.s}^{-1}$ . ....	58
Figure 4.18 – Concentration profiles at the pore bottom, pore middle, channel bottom wall and channel center. The computation was made considering the channel bottom and pore bottom. (a) Scenario 1: $U = 0.1\text{ mm.s}^{-1}$ & $D = 1 \times 10^{-9}\text{ m}^2.\text{s}^{-1}$ . (c) Scenario 2: $U = 0.1\text{ mm.s}^{-1}$ & $D =$	

5 × 10 <sup>-11</sup> m <sup>2</sup> .s <sup>-1</sup> . (b) Scenario 3: $U = 20 \text{ mm.s}^{-1}$ & $D = 1 \times 10^{-9} \text{ m}^2.\text{s}^{-1}$ . (d) Scenario 4: $U = 20 \text{ mm.s}^{-1}$ & $D = 5 \times 10^{-11} \text{ m}^2.\text{s}^{-1}$ .....	58
Figure 4.19 - 2D View of Gradient Generator CFD model and boundary conditions. ....	60
Figure 4.20 – (a) Top view of velocity profile of GG. (b) Spanwise velocity profile at GG mixer exit and membrane entrance. (c) Top view of velocity profile of GG at mixer exit. (d) Top view of velocity profile of GG at membrane entrance. Note that the previous results considered a profile mean velocity of 20 mm.s <sup>-1</sup> .....	61
Figure 4.21 – Top view of pressure profile of GG. Note that the previous results considered a profile mean velocity of 20 mm.s <sup>-1</sup> . ....	62
Figure 4.22 – The following results are obtained for inlets concentration of $cI1 = 1:2$ , $cI2 = 1:20$ and $cI3 = 1:200$ . (a) Top view of concentration profile of GG. (b) Spanwise concentration profile at GG mixer exit and membrane entrance. (a) and (b) considered a profile mean velocity of 20 mm.s <sup>-1</sup> and for a VEGF diffusion coefficient 5 × 10 <sup>-11</sup> m <sup>2</sup> .s <sup>-1</sup> . (c) Top view of concentration profile of GG. (d) Spanwise concentration profile at GG mixer exit and membrane entrance. (c) and (d) considered a profile mean velocity of 0,1 mm.s <sup>-1</sup> and for a small molecule diffusion coefficient 1 × 10 <sup>-9</sup> m <sup>2</sup> .s <sup>-1</sup> .....	62
Figure 4.23 - Top View of Shear Stress Generator (Left – Zoom In   Right – Global). ....	63
Figure 4.24 - 3D View of Shear Stress Generator CFD model and boundary conditions. ....	64
Figure 4.25 – (a) Top view of SS with 1D cuts at 15 µm height. (b) Front view cut of shear stress. (c) Parametrization of shear stress in a cell. ....	64
Figure 4.26 - Cell disposition (a) and Cell spacing (b) schemes. ....	65
Figure 4.27 - Top view of Shear Stress Generator in 7 configurations of cell disposition and cell spacing. ....	65
Figure 4.28 - Bar charts of shear stress parameters analysis in mesh size parametrization with average values and standard deviation. ....	67
Figure 4.29 - Bar charts of shear stress analysis for different cell configurations. ....	69
Figure 4.30 – (a) Image light intensity obtained for GG with DI water in all inlets at mixer exit in zone 1 ( $I_0$ ). (b) Image light intensity obtained for GG with dye solution with concentration 1:20 in all inlets in zone 1 ( $I_i$ ). ....	70
Figure 4.31 - Parametrization of relative light intensity with solution concentration. ....	71
Figure 4.32 – Image alignment in mixer outlet (zones 1,2 and 3) and membrane entrance (zones 4, 5 and 6). The coloured dash lines were slightly misaligned in the scheme to favour visualization. ....	72
Figure 4.33 – Concentration gradient determination in the mixer based on the relative light intensity for inlets with concentration ( $cI1 = 1:1$ ; $cI2 = 1:10$ ; $cI3 = 1:100$ ). Parametrization on velocity from top to bottom ( $U = 0.1$ ; $20.0 \text{ mm.s}^{-1}$ ). Measurement taken at mixer exit and membrane entrance, respectively left and right images.....	74
Figure 4.34 – Concentration gradient determination in the mixer based on the relative light intensity for inlets with concentration ( $cI1 = 1:2$ ; $cI2 = 1:20$ ; $cI3 = 1:200$ ). Parametrization on	

velocity from top to bottom ( $U = 0.1 ; 20.0mm.s^{-1}$ ). Measurement taken at mixer exit and membrane entrance, respectively left and right images.....	75
Figure A.1 – INESC-MN group picture taken in 2017-10-23. ....	87
Figure A.2 – 3D representation of water and VEGF-A molecules. ....	88
Figure A.3 – Concentration gradient determination in the mixer based on the relative light intensity for an inlet with concentration (Left Inlet 1:1   Middle Inlet 1:10   Right Inlet 1:100). Parametrization on velocity from top to bottom ( $U = 0.1 ; 1.5 ; 10.5 ; 20.0mm.s^{-1}$ ). Measurement taken at mixer exit and membrane entrance, respectively left and right images. ....	89
Figure A.4 – Concentration gradient determination in the mixer based on the relative light intensity for an inlet with concentration (Left Inlet 1:2   Middle Inlet 1:20   Right Inlet 1:200). Parametrization on velocity from top to bottom ( $U = 0.1 ; 1.5 ; 10.5 ; 20.0mm.s^{-1}$ ). Measurement taken at mixer exit and membrane entrance, respectively left and right images. ....	90



## List of Tables

Table 2.1 – Physico-Chemical properties of PDMS. (Tabeling 2005).....	14
Table 3.1 – Summary of mask types, features and characteristic features. ....	31
Table 3.2 – Inlet concentration and flow rates for the calibration step (left) and for the gradient determination (right). ....	41
Table 3.3 – Microchannel average velocity, individual inlet flow rate and estimated filling time for 1 <i>mL</i> volume. ....	42
Table 4.1 – SU-8 on the Silica Substrate profilometer assessment points on SS sample in top picture and on GG sample in bottom picture. The pink arrow indicates the order and place of the sample observations. ....	48
Table 4.2 – Parameters of the microfluidic device. ....	51
Table 4.3 – Pressure drop computation and average wall shear stress for enables a pressure balance. ....	52
Table 4.4 – CFD simulation time estimate. ....	53
Table 4.5 – Reynolds Number computation for limit cases. ....	54
Table 4.6 – Dimensional analysis of the flow. ....	55
Table 4.7 – Computation of effective diffusive time in membrane pores bottom.....	58
Table 4.8 – Reynolds Number computation for limit cases. ....	63
Table 4.9 – Cell configurations in shear stress CFD model. ....	65
Table 4.10 - Resume table of simulation parameters in mesh size parametrization. ....	66
Table 4.11 – Shear stress parametrization for mesh size analysis on Coarse, Normal and Fine meshes. Last two columns refer respectively to Chi-square inverse cumulative distribution function and condition verification with a 95% confidence. ....	67
Table 4.12 - Resume table of simulation parameters in cell disposition parametrization. ....	68
Table 4.13 – Shear stress parametrization for different cell configurations. ....	68
Table 4.14 – Mean values and standard deviations for relative intensity.....	70
Table 4.15 – Model fit parameter and interval of confidence. ....	71
Table 4.16 – Relative uncertainty of concentration determination for the six zones of GG and figures correspondence. ....	76
Table 4.17 - Flow estimation in Shear Stress Generator. ....	76
Table 4.18 - Flow estimation in Gradient Generator. ....	77
Table A.1 – Diffusion coefficient computation of water and VEGF-A molecules.....	88

## **List of Abbreviations and Symbols**

CFD – Computational Fluid Dynamics

PDMS – Polydimethylsiloxane

EC – Endothelial Cell

SS – Shear Stress

GG – Gradient Generator

# 1 Introduction

## 1.1 Research Motivation

In the last two decades, the development of microfluidic device for cellular applications has become generalized due to the easiness and low cost of fabrication, use of reagents at a lower scale, an improved control of parameters and dissemination of multi-physics simulations that can predict more accurately the behavior of traditional cell culture techniques. Presently the design of microfluidic platforms is becoming multi-disciplinary to meet higher requirements of researchers to manipulate cellular microenvironment.

In this context the emergence of organ-on-a-chip applications enables further research of living cells in physiological environment with organ and tissue models, by mimicking the parameters and stimulus-response relationships as also spatiotemporal dynamics. These microfluidic devices allow the incorporation of actuators and sensors that probe and recreate, the complex and dynamic relationships between cells and their local environment allowing the isolation of genetic disease determinants and cellular function modulators.

This project aimed the development of a microfluidic device based on polydimethylsiloxane (PDMS) for biomedical analysis, in a joint collaboration between Instituto de *Engenharia de Sistemas e Computadores – Microssistemas & Nanotecnologias* (INESC-MN) and *Instituto de Medicina Molecular* (IMM). The biomedical model of IMM aims to the use of Endothelial Cells, genetically modified in the Par3/Par6/aPKC (Par) complex modulation that plays multiple roles in several cell polarisation events.

The microfluidic device was designed to control simultaneously a VEGF gradient and a shear stress gradient experienced by a group of EC to evaluate the response of competing stimulus in cell polarization.

## 1.2 Objectives

The aim of this work consists in the fabrication and design of a microfluidic device which could simultaneously generate VEGF gradient and shear stress gradient to evaluate the response of competing stimulus in cell polarization.

The specific objectives of this work were the following:

- Draw and design small improvement to existing microfluidic device.
- Define conditions/parameters and simulate the microchannels flow.
- Use the Soft Lithography in microfabrication process of the device.
- Integrate PET membrane between the 2 PDMS devices.
- Simultaneously generate a concentration gradient and uniform shear stress in the EC in the Gradient Concentration (GG) and Shear Stress (SS) generators, respectively.
- Implement an experimental setup to access the microfluidic device for the flow rate and concentration gradient generated.

## 1.3 Thesis Outline

The present work focuses on the given themes: Anatomy and Angiogenesis, Microfluidic Technology with focus on concentration gradient and shear stress generation. These themes were approached on each of the present chapters.

Chapter 2 describes in detail the state of the art on Anatomy and Angiogenesis and Microfluidic Technology. Its last section refers to specific concepts required to design the microfluidic device.

The description of the materials and the methodologies used during this work is performed on Chapter 3.

Finally, Chapter 4 comprises the discussion of the main results obtained, from the microfabrication process to the analysis of the flow rate and concentration gradient generated.

The main conclusion withdrawn from the present work and future work improvements are proposed on Chapter 5.

## 2 State of the Art

For a comprehensive understanding of the microfluidic design directed towards endothelial cell study a theoretical introduction on broad topics is required. Section 2.1 presents a brief introduction on the eye anatomy and angiogenesis to present the main molecular pathways and anatomical restrictions imposed on “in vivo” conditions. Through section 2.2 of this chapter the state of the art of microfluidic device technology is reported ranging from fabrication to application. Finally, in section 2.4, the basic principles of microfluidics are deepened, namely, in the areas of fluid mechanics, focusing in the laminar and creeping flow regimes, and in mass transport.

### 2.1 Anatomy and Angiogenesis

Angiogenesis is an important process for the constitution of new blood vessels from existing ones and plays a crucial role in organogenesis and advanced embryonic and fetal development (Drake 2003). Disturbances in physiological angiogenesis mechanisms have a role in pathogenicity of some diseases such cancers, obesity and atherosclerosis. Research and study in angiogenesis has the potential to find cures to such diseases. The eye cornea is an avascular tissue, whose vessels can be simultaneously studied non-invasively with in vivo corneal angiogenic assays in animal models and in histological samples (Z. Tahergorabi et al. 2012). A brief overview of the eye anatomy and angiogenesis processes and molecular cues is required to understand the chemotactic and mechanotactic modulation of angiogenesis in simpler *ex vivo* models that motivates the present microfluidic design.

#### 2.1.1 Eye Anatomy

The adult human eyeball measures about 25 mm (Tortora et al. 2010) and is divided into three layers: fibrous tunic, vascular tunic, and retina (Figure 2.1 (a)). The fibrous tunic is the outer coat of the eyeball. It consists of an anterior cornea and a posterior sclera. The vascular tunic is the middle layer of the eyeball and is composed of the choroid, ciliary body, and iris. The choroid is a

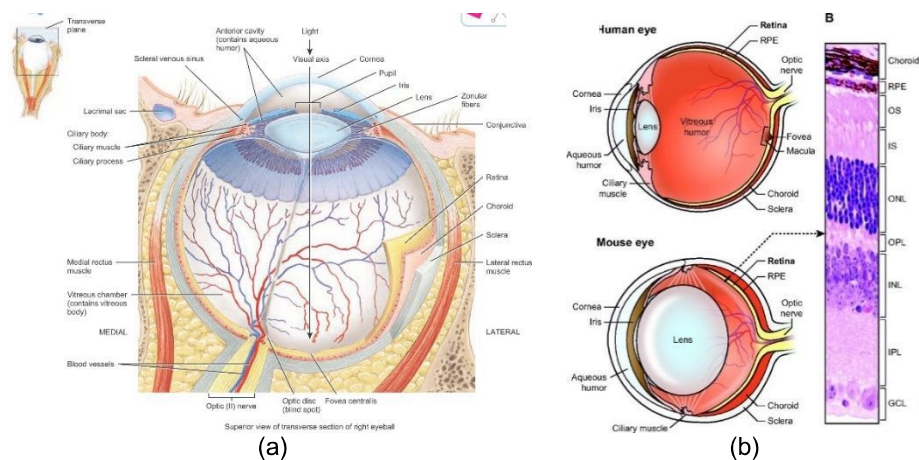


Figure 2.1 – (a) Structure of the human eyeball (Tortora et al. 2010). (b) Structure of the human and mice eyeball anatomy (Veleri et al. 2015).

thin membrane that lines most of the internal surface of the sclera. It contains many blood vessels that help nourish the retina. The third and inner coat of the eyeball, the retina, lines the posterior three-quarters of the eyeball and is the beginning of the visual pathway. It has two layers: the neural layer and the pigmented layer. The neural layer is a multilayered outgrowth of the brain. The pigmented layer of the retina is a sheet of melanin-containing epithelial cells located between the choroid and the neural part of the retina.

The adult mice eyeball measures about 2.5 mm (Henriksson et al. 2009) in diameter and present some differences regarding human eyeball size and anatomy (Figure 2.1 (b)). Nevertheless, the phylogeny proximity between species, the easy optical access to retinal vasculature and reproducibility make mice the best animal model for scalable basic biology studies of the angiogenesis.

## **2.1.2 Angiogenesis**

Angiogenesis is the growth of blood vessels from the existing vasculature. It occurs throughout life in any physiological condition, being more prominent during gestation. All metabolically active tissue in the body are within a few hundred micrometers range from a blood capillary, which is formed by the process of angiogenesis. Capillaries are needed in all tissues for diffusion exchange of nutrients and metabolites.

Endothelial cell migration is essential to angiogenesis. This motile process is directionally regulated by chemotactic, haptotactic, and mechanotactic stimuli and involves the degradation of the extracellular matrix (ECM) to enable progression of the migrating cells. It requires the activation of several signaling pathways that converge on cytoskeletal remodeling. Finally, it follows a series of events in which the endothelial cells extend, contract, and throw their rear toward the front and progress forward.

### ***2.1.2.1 Genesis of cardiovascular system***

Through embryonic development, the cardiovascular system is the first organ system to be formed (Lamalice et al. 2007). During this process, mesodermal cells differentiate into hemangioblasts leading to the formation of primitive blood islands (Figure 2.2 A). Then, the peripheral hemangioblasts differentiate into angioblasts, the precursors of endothelial cells. Following chemotactic and haptotactic activation, ECs migrate allowing the fusion of the blood islands and their remodeling into tubular structures, giving rise to the first primitive vascular plexus. These vascular plexuses remodel into larger vessels, through the process of vasculogenesis, which leads to vascularization of the embryo. In contrast to vasculogenesis, angiogenesis is a neovascularization process by which new blood vessels form from preexisting ones (Figure 2.2 B).

Angiogenesis is required in many physiological and pathological conditions and is regulated by a tight balance of pro- and antiangiogenic agents that trigger a cascade of events in which the migration of capillary EC play a crucial role. Cell culture systems enable the comprehension of basic cellular and molecular mechanisms but to capture the EC migration in physiologic context, an animal model is required, eg. zebra-fish and mouse embryo.

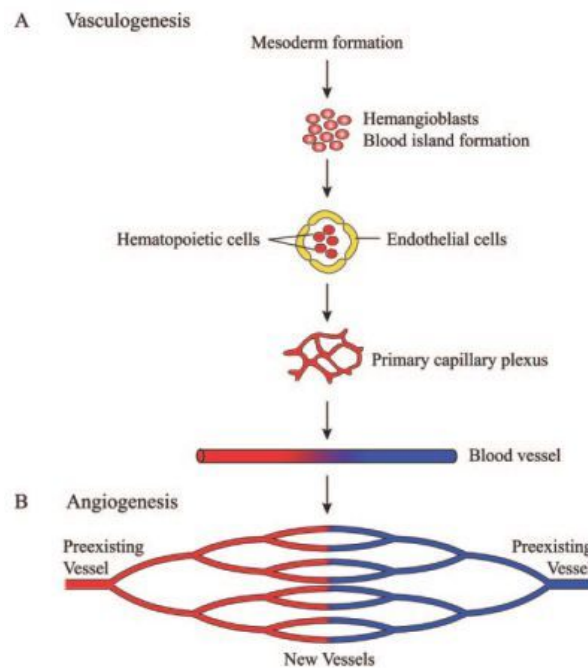


Figure 2.2 – Genesis of vascular system (A – Vasculogenesis; B - Angiogenesis) (Lamalice et al. 2007).

### 2.1.2.2 Angiogenic Process

Sprouting angiogenesis and intussusceptive angiogenesis both occur in utero and in adults. Sprouting angiogenesis is characterized by sprouts composed of ECs, which usually grow toward an angiogenic stimulus such as VEGFA and add blood vessels to portions of tissues previously devoid of blood vessels. On the other hand, intussusceptive angiogenesis involves formation of blood vessels by a splitting process in which elements of interstitial tissues invade existing vessels, forming transvascular tissue pillars that expand in low shear stress areas. Both types of angiogenesis are thought to occur in virtually all tissues and organs.

### 2.1.2.3 Sprouting Angiogenesis

Sprouting angiogenesis is initiated in poorly perfused tissues when oxygen sensing mechanisms detect a level of hypoxia that demands the formation of new blood vessels to satisfy the metabolic requirements of parenchymal cells.

In the absence of pro-angiogenic stimuli, endothelial cells (EC) are retained in a quiescent state. In addition, EC homeostasis is maintained by low-level autocrine vascular endothelial growth factor A (VEGFA) signaling (Figure 2.3 – a) (Ingber 2003).

The basic steps of sprouting angiogenesis include enzymatic degradation of capillary basement membrane, EC proliferation, directed migration of EC, tubulogenesis (EC tube formation), vessel fusion, vessel pruning, and pericyte stabilization.

During angiogenesis, elevated levels of exogenous pro-angiogenic factors (such as VEGFA and VEGFC) and of VEGF receptor 2 (VEGFR2) or VEGFR3 signaling select 'tip cells' (TC; blue) for

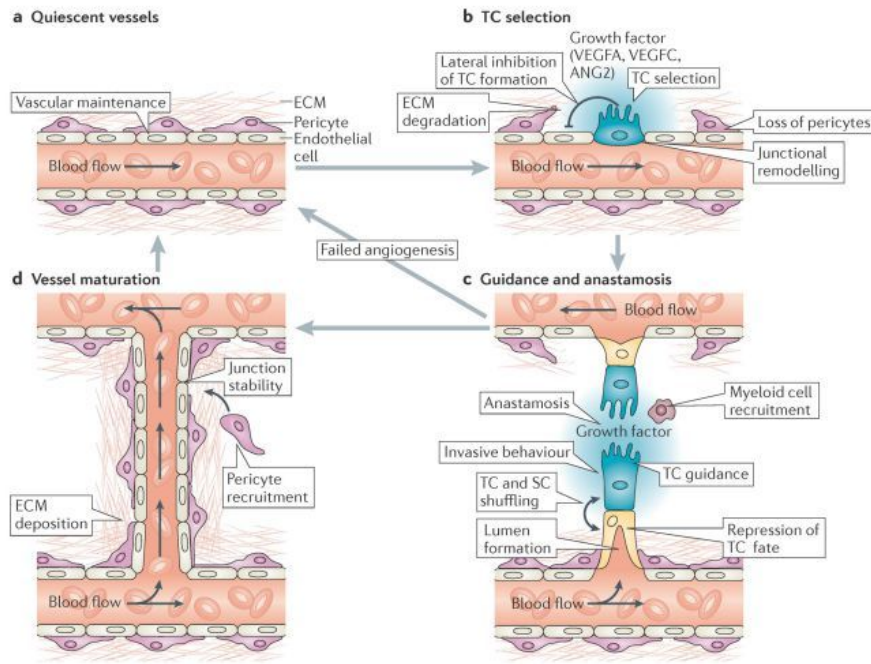


Figure 2.3 – Cellular mechanism of cellular sprouting (Herbert et al. 2012).

sprouting. By contrast, Delta-like 4–Notch signaling laterally inhibits TC fate in adjacent EC. TC sprouting behavior is facilitated by the vascular endothelial cadherin-mediated loosening of EC-EC junctions, matrix metalloproteinase-mediated degradation of extracellular matrix (ECM) and the detachment of pericytes (purple) (Figure 2.3 – b).

Invasive TC sprouting is guided by gradients of pro-angiogenic growth factors and various environmental guidance cues, such as semaphorins and ephrins. During sprout elongation, TC are trailed by endothelial ‘stalk cells’ (SC; yellow), which maintain connectivity with parental vessels and initiate partitioning-defective 3 (PAR3)-mediated vascular lumen morphogenesis. Expression of VEGFR1 and activation of Notch, Roundabout homologue 4 and WNT signaling in SC repress TC behavior to maintain the hierarchical organization of sprouting EC. Nevertheless, TC and SC may also shuffle and exchange positions during angiogenic sprouting. Upon contact with other vessels, TC behavior is repressed, and vessels fuse by the process of anastomosis, which is assisted by associated myeloid cells (Figure 2.3 – c).

Nascent perfused vessels are subsequently stabilized by the platelet-derived growth factor B-mediated recruitment of supporting pericytes, the strengthening of EC-EC contacts and the deposition of an ECM to re-establish a quiescent endothelial phenotype (Figure 2.3 – d).

The key signaling pathways and the molecular mechanisms of lumen morphogenesis and EC tip selection are active fields of fundamental science research (Herbert et al. 2012).

#### 2.1.2.4 Intussusceptive Angiogenesis

Intussusceptive angiogenesis is a dynamic intravascular process capable of dramatically modifying the structure of the microcirculation. The distinctive structural feature of intussusceptive angiogenesis is the intussusceptive pillar - a cylindrical microstructure that spans the lumen of small vessels and capillaries. The extension of the intussusceptive pillar appears to be a mechanism for pruning redundant



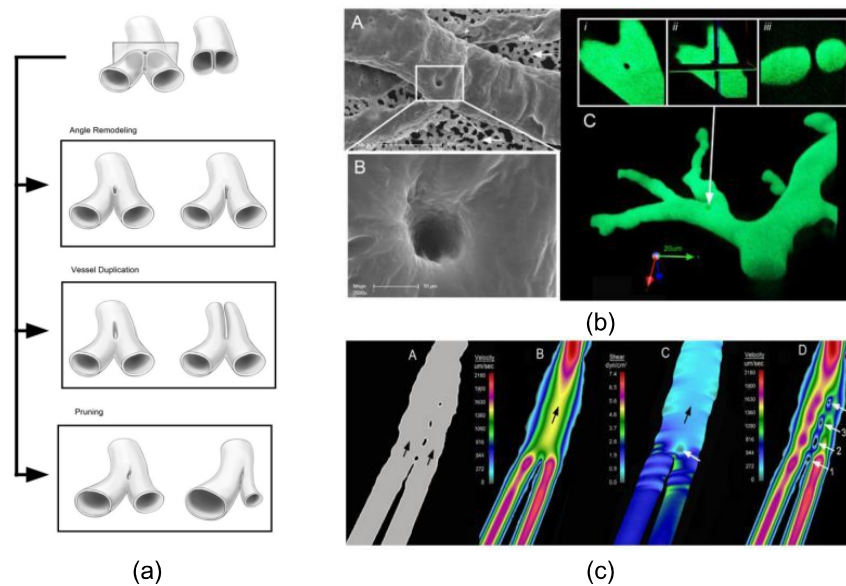


Figure 2.4 – (a) Schematic representation of pillar extension with three different results. (b) Intussusceptive pillars in the CAM imaged with scanning electron microscopy and confocal microscopy. (c) Finite element models of bifurcating vessels in the chick CAM where pillar extension emerged in low shear stress zone (De Spiegelaere et al. 2012).

or inefficient vessels, modifying the branch angle of bifurcating vessels and duplicating existing vessels (Figure 2.4 (a)). Despite the biological importance and therapeutic potential, intussusceptive angiogenesis remains a mystery, in part, because it is an intravascular process that is unseen by conventional light microscopy.

Intussusceptive pillar form preferentially in low shear stress areas oriented orthogonally to the bifurcation plane of branching vessels. Finite element models of animal models suggest that shear stress has an ideal range of triggering in the intussusceptive pillar (Figure 2.4 (c)). Its location could indicate the presence of blood-borne elements, such as endothelial progenitor cells, to microcirculation areas undergoing active angiogenesis. Intussusceptive angiogenesis can be stimulated in the chick chorioallantoic membrane (CAM) with application of VEGF-A, and there is little doubt that many growth factors and signaling systems are involved (Makanya et al. 2005)(C. Y. Lee et al. 2011).

#### 2.1.2.5 Endothelial cell migration

EC migration involves three major mechanisms, namely chemotaxis or the directional migration toward a gradient of soluble chemoattractants; haptotaxis which is the directional migration toward a gradient of immobilized ligands; and mechanotaxis or the directional migration generated by mechanical forces (Li et al. 2005).

Growth factors such as VEGF and basic fibroblast growth factor (bFGF) drive EC by chemotaxis, whereas haptotaxis is associated with increased EC migration activation in response to integrins binding with ECM component (Giroux et al. 1999)(Klemke et al. 1997). Mechanotaxis, which is initiated by fluid shear stress, modulates several steps of migration including extension at the leading edge, adhesion to the matrix, and release of adhesions at the rear (Li et al. 2005).

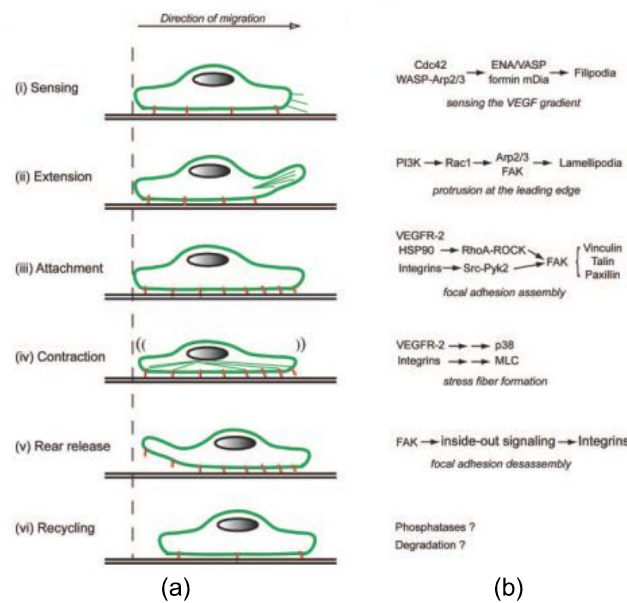


Figure 2.5 – (a) Major steps of EC migration and (b) major signaling events associated to each step (Lamallice et al. 2007).

EC migration can be divided in 6 sequential events (Figure 2.5 (a)):

- (i) Cdc42 dependent sensing of the motile stimuli by filopodia;
- (ii) cellular extension involving the Rac1-dependent formation of protruding lamellipodia;
- (iii) attachment of the protrusions to the extracellular matrix at focal adhesions;
- (iv) stress fiber-mediated contraction of the cell body allowing forward progression;
- (v) rear release by stress fiber-mediated traction forces;
- (vi) recycling of the adhesive and signaling components.

The major signaling events associated with each of these 6 steps are indicated in Figure 2.5 (b). Vascular wall shear stress varies along arterial tree, which is determined by flow velocity characteristics, ranges between 1 and 7 Pa (Theodoros et al. 2005). To study the effects of mechanotaxis and chemotaxis in EC a review on available microfluidic device solutions is addressed in the following section.

## 2.2 Microfluidic Devices

### 2.2.1 Applications of Microfluidic Devices

Microfluidic devices, also known as Biological Micro-Electro-Mechanical Systems (bioMEMS) are related to the manipulation and analysis of minute volumes. MEMS development over the past four decades allowed the miniaturization and appearance of novel analytical approaches of conventional laboratory processes to handle fluids in large scale laboratories at a submillimeter scale mainly in life sciences (Rosa 2010). The reduction of consumed reagents and samples and automation of processes (e.g. reagent / sample actuation, mixing, separation, filtration, reaction, control, monitoring, etc.) together with the integration of micro-to-nano elements (e.g. mechanical or electronic sensors and actuators)



*Figure 2.6 – Commercially available microreactors solutions. (a) 5-layer glass micro reactor from Micronit (2017). (b) Microreactor explorer kit from Sigma-Aldrich (2017).*

contribute for an overall high throughput and low cost devices (Silverio et al. 2017) (Samiei et al. 2016).

Amongst the life science applications of microfluidics devices three fields stand out: biotransformation, analytics and cellular assays. Biotransformation consists in the miniaturization of chemical or biological reactors handling liquids under controlled conditions (e.g. temperature, pH, etc.) to produce and concentrate a molecule of interest. Examples of microreactors can be seen in Figure 2.6.

Analytics concerns about the characterization of the molecule of analysis (e.g. biomolecules, proteins, nucleic acids, etc.) meeting high precision liquid manipulation and the fully automation and portability of complex analytical protocols (Figure 2.7). Some microfluidic clusters and commercial applications start emerging like the FastGene Project (Elveflow 2011) for Ebola detection, Abaxis for blood analyzer (electrolyte, immunoassay, and blood gas) (Abaxis 1995) and Magnomics (Magnomics 2013) for multiple pathogen detection in bovines.

Cellular assays aim to replicate adequate media conditions that enable viability and activity managing control parameters (e.g.  $pH$ , temperature, gas levels ( $O_2$ ,  $CO_2$ , etc.), nutrition and metabolite removal). Organ-on-a-chip are miniaturized microfluidic platforms for cellular assays designed to reproduce physiological and biological parameters of organ and tissue models (Figure 2.8). These platforms can fill the gap between conventional planar, static cultures used for preclinical animal models in drug screening and have the potential for personalized medicine applications. Zhang et al. (2017) developed an integrated automated modular PDMS microfluidic platform that incorporates physical and electrochemical immunobiosensors and miniaturized microscopes for human liver-cancer and heart-liver-on-chips.

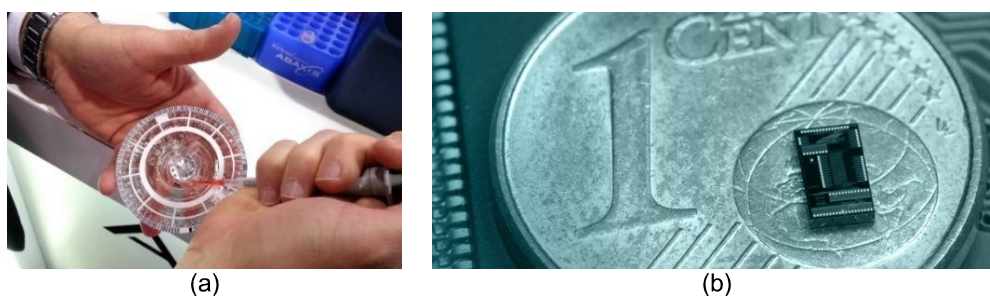


*Figure 2.7 -Commercially available microfluidic analytics solutions. (a) Vetscan LOC rotor based blood analyzer from Abaxis (1995). (b) LOC in-vitro molecular diagnostics from Magnomics (2013).*

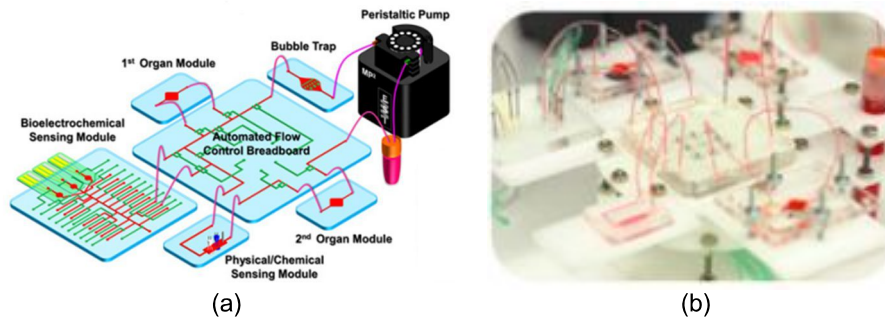


Figure 2.8 – (a) Schematic illustration of integrated microfluidic device composed by microbioreactors, breadboard, reservoir, bubble trap, physical sensors, and electrochemical biosensors. (b) Photograph of the PDMS integrated microfluidic device (B). (Zhang et al. 2017)

H. Lee and Cho (2016) developed a 3D bioprinting method that enables a one-step fabrication of Organ-on-a-chip without a secondary cell-seeding process that showed promising results in hepatocytes which exhibited enhanced liver function (Figure 2.9).

## 2.2.2 Characterization of Microfluidic Devices

According to the main liquid propulsion principle Stetten, Mark, and Haeberle (2010) divide microfluidic platforms in 5 groups: capillary, pressure driven, centrifugal, electrokinetic and acoustic systems (Stetten et al. 2010). The platform used in the work presented here is pressure driven.

A pressure driven laminar flow platform is characterized by liquid transport mechanism based in pressure gradient that leads to hydrodynamically stable laminar flow profiles in microchannels. Pressure source implementation can be internal or external and induced by syringes, pumps, pneumatic displacement of membranes, amongst others in a batch-wise or continuous mode.

Due to the laminarity of the flow in the microchannels over a wide range of flow rates and channel dimensions, pressure driven platforms enable assays implementation with: predictable velocity profiles, controllable diffusion mixing and stable phase arrangements (co-flowing streams). These platforms are suitable for continuous processing of samples enabling online monitoring of desired parameters and require the connection of a pressure source to the (disposable) chip.

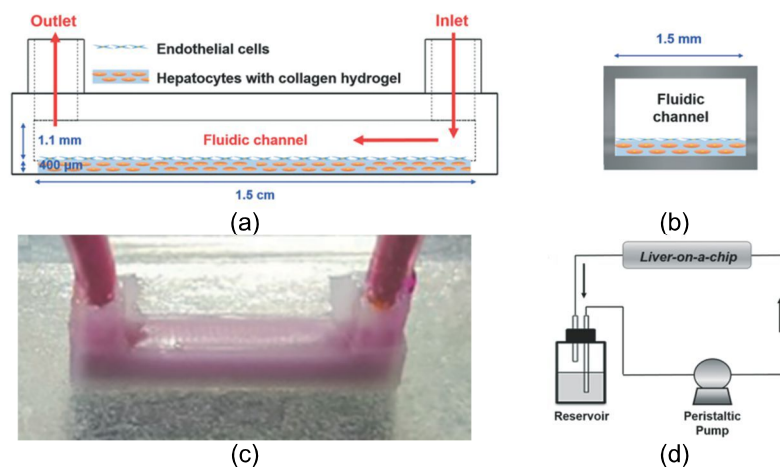


Figure 2.9 – Schematic of the (a) side view, (b) vertical sectional view and (d) perfusion system of the liver-on-a-chip. (c) Photograph of the channel with the PCL material. H. Lee and Cho (2016)



One of the key properties of PDMS is that it can be sealed to itself or to other substrates both in reversible or irreversible manner. Furthermore, PDMS can be casted in almost any shape and openings for fluidic and electrical connections which can be easily achieved through punching or cutting after curing.

Reusability, ease of clean and high pressure sealing resistance of microfluidic devices are attractive features for cell studies in research laboratories but difficult to reconcile. Some techniques like mechanical or magnetic clumping could be used to fulfill these requirements.

### 2.2.3 Mixing Techniques in Microfluidics

In microfluidic devices mixing presents a challenge due to its particular laminar flow nature, derived from low Reynolds numbers. The mixing enhancement techniques can be classified in passive mixing and active mixing (Ward et al. 2016).

Passive mixing techniques are easy to integrate but difficult to control after fabrication. These mixing techniques explore Taylor dispersion effect described in section 2.4.2.4 and include stream splitting and recombination, slanted wells or patterned grooves, hydrophobicity or surface modification and multiphase mixing enhancement. The T-junction system is the simpler one and relies solely in the diffusion transport of the concurrent inlets in the developing zone. The dilution network relies on the creation of several stream splitting and recombination levels to create a concentration profile at the mixer outlet less independent of flow rate (Figure 2.10 (i)). Kwak et al., (2016) tested a slanted well to create a complex concentration profiles with the convection-diffusion flow dependency on the 3D geometry (Figure 2.10 (ii)).

Active mixer techniques are more difficult to integrate and require external components to operate. These techniques include microstirrers, acoustic waves, flow pulsation, optofluidic enhancement, thermal enhancement and electrokinetic mixing enhancement.

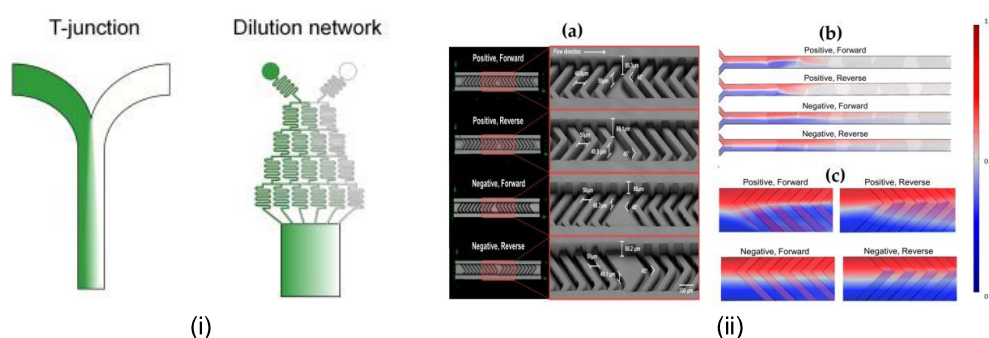


Figure 2.10 – (i) Stream splitting and recombination technique (Lin et al. 2015). (ii) Staggered herringbone mixer (SHM) created by Kwak with detailed pattern structures and flow directions (a), mixing quality over 2.5 cycles on SHM for different conditions (b) and top view images of SHMs efficiency after 1 cycle (c) (Kwak et al. 2016).

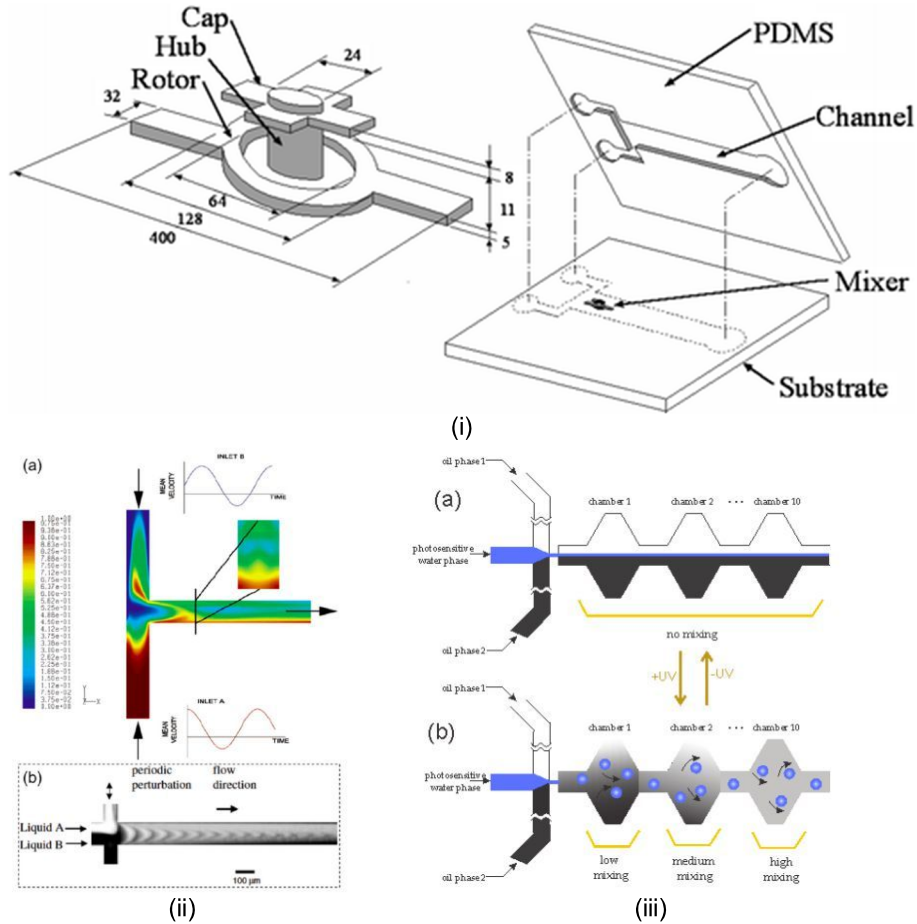


Figure 2.11 – (i) Schematic diagram of a single micro stirrer in the fluidic device (Ryu et al. 2004). (ii) T-junction with two pulsatile inlets with 90° phase difference simulation (a) and experimental results (b) (Ward et al. 2016). (iii) Schematic of the reversible optofluidic mixer with no mixing when ultraviolet (UV) is off (a) and mixed at the presence of UV due to the photosensitive water turns into the droplets, causing the mixing between two oil phases (b) (Venancio-Marques et al. 2013).

Ryu, Shaikh, Goluch, Fan, & Liu, (2004) a microstirrer that used a rotor to enhance the mixing of the inlets of a T-junction (Figure 2.11 (i)). Ward & Fan, (2016) imposed two pulsatile inlets with a 90° phase shift to enhance the diffusion, that reduced the distance required for the mixing and exhibited at a given developing distance a concentration profile less sensible to the phase of the inlet flow (Figure 2.11 (ii)). Venancio-Marques, Barbaud, & Baigl, (2012) created a system with 3 inlets with different immiscible phases in which one is constituted by photosensitive water solution. This system is activated when UV-light is used in the water that disrupts the balance and promote diffusion through the creation of water droplets that exhibit spanwise movement in the chamber and enable the solutions complete mixing in a small number of chambers (Figure 2.11 (iii)).

## 2.3 Microfabrication Techniques for Microfluidic Devices

The comprehensive design of microfluidic devices is a technically challenging task that is limited by the fabrication techniques and materials chosen. Fabrication techniques used for silicon-based microfluidic devices are mostly based in Micro-Electro-Mechanical-Systems (MEMS) methods, that adopted well established techniques in the integrated circuit (IC) industry (Silverio et al. 2017). This way

the first generation of microfluidics use inorganic materials (Silica and Glass) that compose “rigid” substrates.

The second generation of microfluidic devices resorts to polymeric materials, (thermoplastic e.g. (polymethyl methacrylate (PMMA)) and elastomers (e.g. polydimethylsiloxane (PDMS)). These materials compose “flexible” substrates that are simpler to process, more functional (transparent, biocompatible, etc.) and present a rapid and inexpensive prototyping solution. The increasingly sophistication of microfluidic techniques has evolved to include composite materials and modular configurations.

Lately the synergy between fundamental material development and new microfluidic capabilities has also expanded the fabrication strategies 3D (bio)printed composites (including particles and fibers) and organoids (Hou et al. 2017) in what it is likely to constitute the third generation of microfluidic devices.

### 2.3.1 Fabrication of elastomeric microfluidic devices

PDMS has become the most commonly used elastomer in rapid prototyping of microfluidic devices due to its simplicity and strong sealing to a myriad of materials, and additional useful properties like low cost, low toxicity, transparency from visible to near ultraviolet wavelengths and chemical inertness.

PDMS belongs to the group of siloxanes, where the skeletal atoms consist of an inorganic siloxane group and bear side groups of methyl (Figure 2.12). The repeating unit, the simplest repetitive structure, is  $[-Si(CH_3)_2O-]$ . PDMS has low interfacial free energy which is susceptible to protein adhesion. This protein fouling in PDMS can be tackled manipulating interfacial free energy with plasma treatment. Table 2.1 summarize its most important properties.

PDMS is permeable to gas and although gas permeability enables quick filling and therefore make it suitable for cell assays, it is also permeable to non-polar solutes which makes it inadmissible for some applications, eg cell signaling assays where some molecules can be absorbed. Despite having a low interfacial free energy, PDMS surface exhibits some fluorescence and some protein adsorption due to its hydrophobic nature specially in aqueous environments which can be solved with additional surface treatments. Additionally, properties of reticulated PDMS change with time which make aging effects difficult to anticipate.

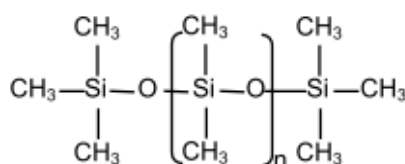


Figure 2.12 – Chemical structure of PDMS.

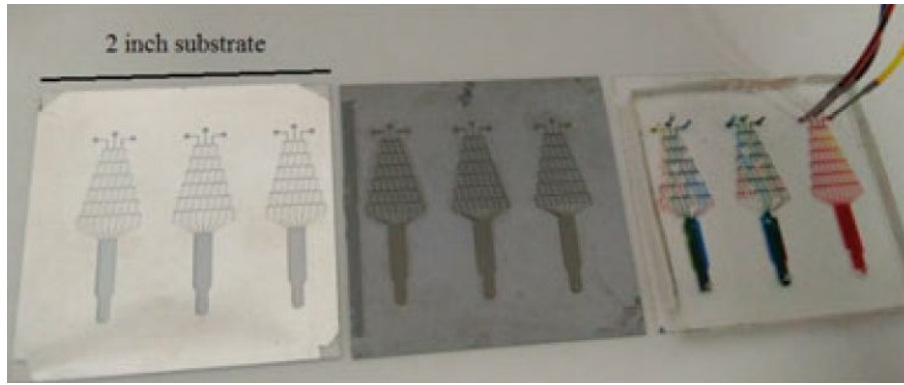


Figure 2.13 – Hardmask (glass substrate with thin flim layer of Aluminium), master mold (silica substrate with SU-8 PR layer) and PDMS microfluidic device. (Silverio et al. 2017)

Table 2.1 – Physico-Chemical properties of PDMS. (Tabeling 2005).

Property	Characteristic
Density	$\approx 0,9 \text{ kg/m}^3$
Optical	Transparent, between 300 nm and 2200 nm
Electrical	Insulating, breaking field $20 \text{ kV.cm}^{-1}$
Mechanical	Elastomeric, Young's modulus $\sim 750 \text{ kPa}$
Thermal	Insulating, thermal conductivity $\sim 0.2 \text{ W.m}^{-1}.\text{K}^{-1}$
Interfacial	Low surface energy ( $\approx 20 \text{ mN.m}^{-1}$ )
Permeability	Permeable to gas, apolar organic solvents, nearly impermeable to water
Reactivity	Inert, oxidizable by a plasma
Toxicity	Non-toxic

Microfabrication of a PDMS microfluidic device is composed by three main steps: hardmask patterning, master mold fabrication (both photolithography processes) and replica micromolding that lead to the production of several components (Figure 2.13). The hardmask defines the 2D geometry of the master mold and the photoresist (PR) coating and spinning defines the master mold height. Final geometry of the microfluidic device is defined when the elastomer is poured and cured in the master mold.

Hardmask is a metallic thin film layer (e.g. aluminium) in a transparent substrate (e.g. glass). Hardmask patterning is a LASER lithography process that used a positive photoresist in this project.

Lithography is a key technique for the fabrication of microscale structures. According to the type of energy beam it can be subdivided in photolithography, X-ray lithography, electron lithography or ion lithography (Nguyen et al. 2002). The comprehension of the lithography process is essential to understand the fabrication of microfluidic devices with more emphasis to photolithography that resorts to UV-light. This process is composed by three steps (Figure 2.14):

1. Positioning process which comprises:
  - a. Design of geometric pattern on a computer-aided design (CAD) software;



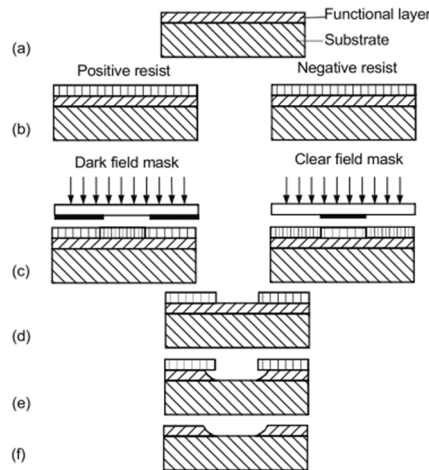


Figure 2.14 – Pattern transfer with photolithography: (a) deposition of functional layer; (b) coating photoresist (positive or negative); (c) photolithography (dark field mask or clear field mask); (d) developing photoresist; (e) selective etching; (f) structure is transferred to functional layer (Nguyen et al. 2002).

- b. Mask making to define the light pattern (that can be absent in case the process is maskless (e.g. LASER lithography));
  - c. Photoresist (PR light sensitive polymer) coating of the wafer adjusted to the desired thickness;
2. Exposure process: consisting in light (UV, LASER or electrons) exposition to the PR to define the geometric pattern and whom exposition time is defined by its energy absorption;
3. Development process: depending on PR type the geometric pattern is revealed by dissolving the soluble parts where:
  - a. Negative PR when exposed to light becomes insoluble to developer solution
  - b. Positive PR when exposed to light becomes soluble.

The minimum feature size (m.f.s.) depends on light wavelength, mask positioning and removal and PR development pattern.

After defining the hardmask, the process fabrication continues with soft lithography. It consists in several steps detailed below.

In this project the PR used was SU-8 that is a negative PR. The pre-treatment starts with a cleaning process followed with a thermal treatment to prevent any entrapped humidity at the surface (Figure 2.15 (a)). The PR is then dispensed and evenly distributed to the desired thickness by adjusting the time and spinning velocity of coating according to the kinematic viscosity (temperature dependent) of the PR (Figure 2.15 (b)). A soft-bake step is required to evaporate PR solvents and prevent later shrinkage and cracking of the PR coating (Figure 2.15 (c)). The soft-bake duration and temperature is adjusted according to the PR formulation and coating thickness. The PR coating is exposed to UV light through the hardmask to define the desired 2D pattern in the mold (Figure 2.15 (d)). The UV light energy exposure and duration is dependent on PR formulation, thickness and substrate material. To harden the insoluble regions of PR to the developer solution, a post-exposure bake step is performed (Figure 2.15 (e)). A slow cooling step is very important to avoid cracks due to thermal stresses. The development

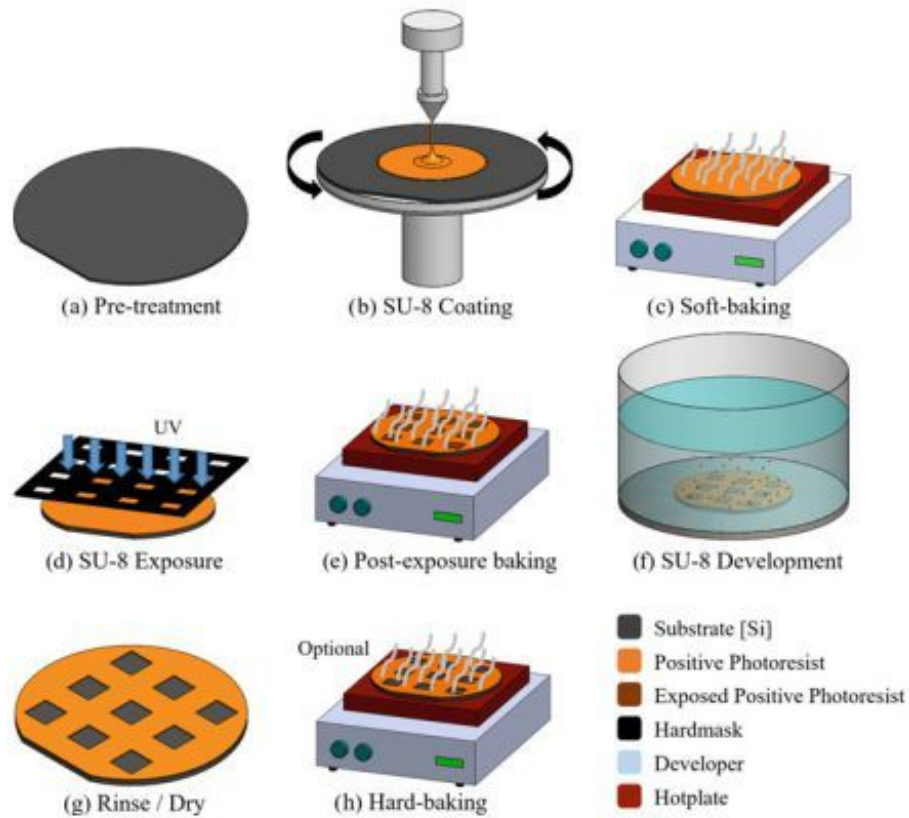


Figure 2.15 – Fabrication of the master mold by photolithography. (Silverio et al. 2017)

step is made to dissolve PR soluble regions and its duration depends both on PR dissolution rate and agitation conditions (Figure 2.15 (f)). The substrate is washed with isopropyl alcohol where the formation of white precipitate indicates an under-development. Finally, a final rinse with deionized water and blow drying (Figure 2.15 (g)). Master mold reusability can be extended using a final hard-baking step (Figure 2.15 (g)) that must be performed in similar manner as the previous bake steps.

The master mold can be reused several times in a method which is suitable for rapid prototyping and low-cost applications. In replica molding the prepolymer is crosslinked with the curing agent in a weight ratio of 10:1. The process starts with mixing of the parts to cure and a degassing process to remove bubbles formed previously. Finally, the mixture is poured over the master mold structure (e.g. a silica wafer with an inverse PR (e.g. SU-8) structure of the channel) and then cured at relatively “low” temperature (60°C to 80°C for several hours) (Figure 2.16). The cured structures can be peeled from the master mold and further bonded to a planar structure (clean glass, silica or another piece of activated PDMS) that will form the microchannel structures. The sealed channel can withstand pressure up to

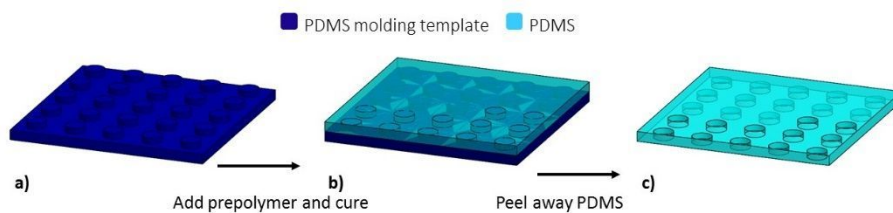


Figure 2.16 – Schematic of fabrication steps adopted in replica molding. (Silverio et al. 2017)

5 bar (Nguyen et al. 2002). The resolution of this technique can be less than 10 nm (Nguyen et al. 2002) but due to shrinkage related with aging phenomena values above 5  $\mu\text{m}$  are commonly accepted as minimum feature size (m.f.s.) (Tabeling 2005).

### 2.3.2 Bonding Techniques

The assembly of more complex microfluidic device components requires a three-step controlled process which can be divided into: bonding or sealing; supply of liquid, reagent and sample; and connection with electronic or microelectronic components (Figure 2.17).

Sealing in microfluidic devices is essential to maintain samples, solvents and reagents within defined volumes, to prevent uncontrolled spreading and evaporation of liquids along wettable areas from chips, to reduce contamination and biohazards, and to isolate and protect structures from dust or physical impacts (Temiz et al. 2015).

Sealing strategies can be subdivided based on conformal materials (PDMS), non-conformal polymers (plastics), hard materials such as glass and silicon, intermediate adhesive layers, and recently new prototyping technologies. Due to the scope of the present work only PDMS substrates sealing techniques will be addressed focusing on the possibility of process reversibility.

Amongst reversible techniques simple passive mechanical or heat treatment sealing can be suitable for low pressure flows, whilst the inclusion of microfluidic networks, valves and pumps resort to irreversible self-sealing of PDMS. Surface treatments can also be applied to replica molding technique in which PDMS surface layer can be exposed to a  $O_2$  plasma treatment where the device components (e.g. Silicon or Glass substrates) are placed in contact with PDMS. This assembly can create complex 3D microfluidic networks connecting multilayers by microfluidic vias. *Jamal (2011)* demonstrated a hybrid SU-8/PDMS self-assembly microfluidic device that spontaneously curve PDMS microfluidic network in cylindrical flow paths (Figure 2.18). Alternatively, the adhesive layer can be patterned to form the microfluidic layer that can be achieved through UV-curing adhesives, SU-8 and parylene.

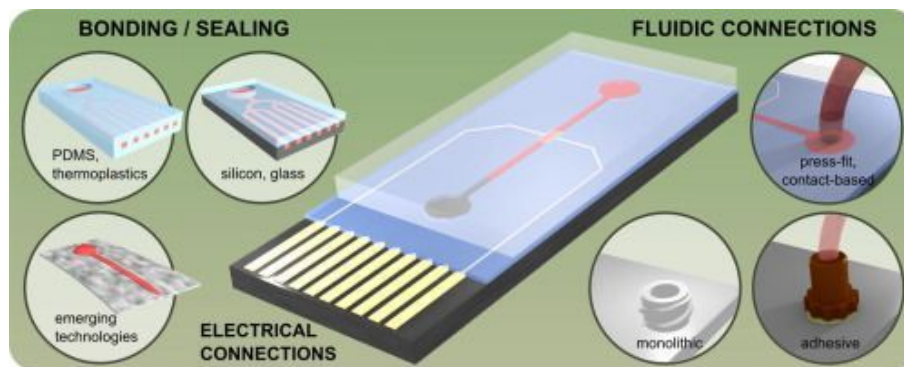


Figure 2.17 – Microfluidic devices require bonding / sealing of components, connection to pumping peripherals and electrical connection to actuators or sensors (Temiz et al. 2015).

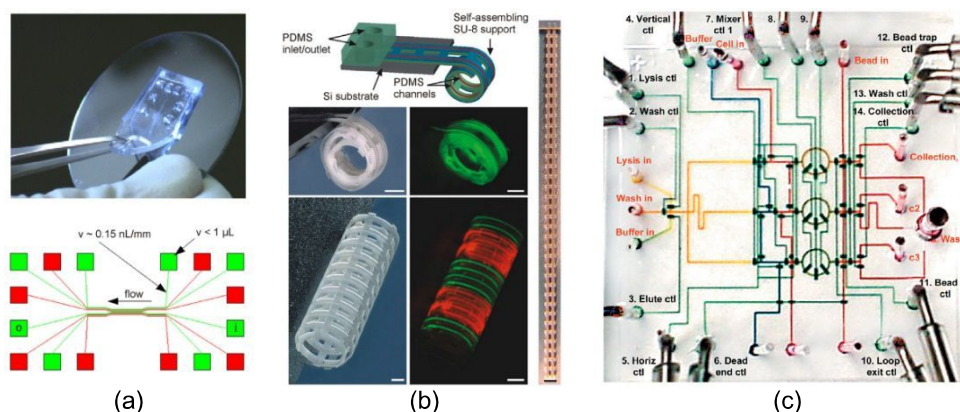


Figure 2.18 – (a) PDMS on Glass microfluidic device for local delivery of a protein solution in a confined surface (Temiz et al. 2015). (b) Hybrid SU-8/PDMS self-assembling flexible microfluidic device at middle (Jamal et al. 2011). (c) Insertion of tubings in molded PDMS layers on a DNA purification chip at right (Hong et al. 2004).

Reusability, ease of clean and high pressure sealing resistance of microfluidic devices are attractive features for cell studies in research laboratories but difficult to reconcile. Some techniques like mechanical or magnetic clumping could be used to fulfill these requirements.

Yang (2003) resorted to electrical socket to enable easy mechanical locking that withstand a limit pressure of  $200 \text{ kPa}$  (Figure 2.19 (a)). Cooksey (2009) developed a PDMS-based vacuum manifold that applies a negative pressure on the manifold and the chip that withstand a  $100 \text{ kPa}$  liquid pressure. The conformal contact between PDMS manifold and PMMA chip allows hundreds of fluidic interfaces simultaneously (Figure 2.19 (b)).

Tkachenko (2009) developed a reusable magnetic clumping microfluidic device system capable to withstand up to  $40 \text{ kPa}$  (Figure 2.20 (a)). Ruiz (2012) developed an elegant system capable of the

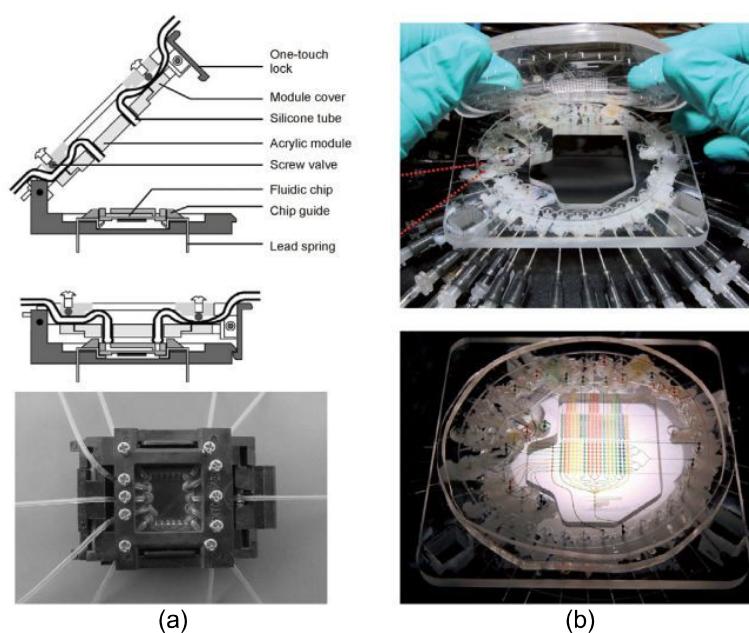


Figure 2.19 – (a) Mechanical lock based contact with electric socket at left (Yang et al. 2003). (b) Elastomeric frame with vacuum manifold at tubings inlet (Cooksey et al. 2009).



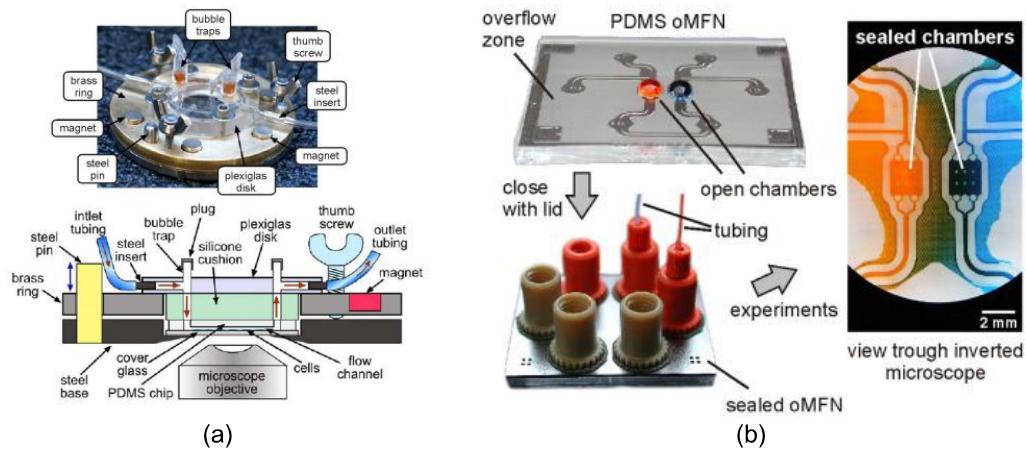


Figure 2.20 – (a) Reversible sealing by magnetic clamping (Tkachenko et al. 2009). (b) PDMS sealing of overflow microfluidics achieved by selective surface wettability (Ruiz et al. 2012).

solution during the sealing ideal for cell growth and with solution handling with a pipette. The latter was achieved using surface wettability at cell chambers (Figure 2.20 (b)).

## 2.4 Physical Principles of Microfluidics

A comprehensive knowledge on the physical mechanisms that rule the flow in microfluidic devices is required to enable an assertive design. Flow analysis, however, requires a multi-physics approach and the consideration of interactions due to scaling effects. Therefore, the exposition of fluid mechanics and mass transport principles is made in this section.

### 2.4.1 Basic Concepts

#### 2.4.1.1 The continuum approximation

In fluid mechanics and mass transport, properties like velocity, density and concentration vary at a molecular level, however to enable its modeling it is acceptable to consider the fluid as “continuous”. The range of volumes found in microfluidics range from 1 picoliter  $(100 \mu\text{m})^3$  to 1 milliliter  $(1 \text{ cm})^3$ . One picoliter contains approximately  $3 \times 10^{13}$  molecules of water enough to consider their average properties. Typically, for most properties the continuum approximation doesn’t break until the scale of molecular diameters is reached.

Therefore, the validity of the continuum hypothesis can be accepted, since it assumes that the macroscopic properties of the fluid are similar to a perfectly continuous fluid, although is composed by molecules.

This way, quantities such as momentum, energy and mass implicated in a small volume of fluid containing a sufficiently large number of molecules are to be defined as a result of the sum of the corresponding quantities for the molecules in the volume (Wei-Cheng et al. 2009).

#### 2.4.1.2 Bernoulli’s Principle

A common approximation used in hydraulics is the Bernoulli’s principle (Bernoulli 1738) that can relate pressure, velocity and height in a steady motion of an ideal fluid. This form can be derived

assuming the energy conservation along a streamline between two cross sections imposing one dimensional flow. Microflows in capillaries and microchannels are suitable for the Bernoulli's principle application if the flow is mainly one dimensional, the fluid incompressible and boundaries rigid (Figure 2.21). Global energy per unit volume ( 2.1 ) composed by kinetic ( $\frac{1}{2}\rho U_i^2$ ), potential ( $\rho g z_i$ ) and pressure components ( $P_i$ ) and the energy loss per unit volume between two points.

$$E_1 = E_2 + \Delta P \quad E_i = \frac{1}{2}\rho U_i^2 + \rho g z_i + P_i \quad (2.1)$$

Combining the expressions of ( 2.1 ) the final form ( 2.2 ) is obtained.

$$\Delta P = P_2 - P_1 \quad \frac{1}{2}\rho U_1^2 + \rho g z_1 = \frac{1}{2}\rho U_2^2 + \rho g z_2 + \Delta P \quad (2.2)$$

#### 2.4.1.3 Laminar and Creeping Flow

Microfluidics present almost always smooth laminar flow, that is characterized by parallel streamlines. Turbulent flow, however is characterized by its stochastic nature and the presence of eddies that disrupt parallel streamlines (Figure 2.22). The dimensionless number Reynolds number ( $Re$ ) determines the ration between inertia (convective forces) and viscous forces and is defined by ( 2.3 ), where  $D_h$  (m) is the hydraulic radius,  $U$  ( $m.s^{-1}$ ) the average velocity of the flow,  $\rho$  ( $kg.m^{-3}$ ) is the fluid density,  $\eta$  ( $Pa.s$ ) is the viscosity and  $\nu$  ( $m^2.s^{-1}$ ) the kinematic viscosity.

$$Re = \frac{UD_h}{\nu} = \frac{D_h U \rho}{\eta} \quad (2.3)$$

The hydraulic diameter is equal to  $D_h = \frac{4A_{cs}}{P_w}$  (m), where  $A_{cs}$  ( $m^2$ ) is the cross section area of the channel and  $P_w$  (m) is the wetted perimeter of the channel.

The Reynolds number can be used to predict the transition between laminar to turbulent regimes usually associated for  $Re \approx 2100$  in cylindrical channels. For most of microfluidic systems laminar regimes are observed since this value is low ( $Re < 10$ ). Creeping flow, also referred to as the Stokes flow problem, is the generic name given to flows with a very low Reynolds number approaching zero ( $Re \ll 1$ ) and represents a limiting case of laminar flow which occurs when viscous forces completely dominate inertia forces (Shah et al. 1978).

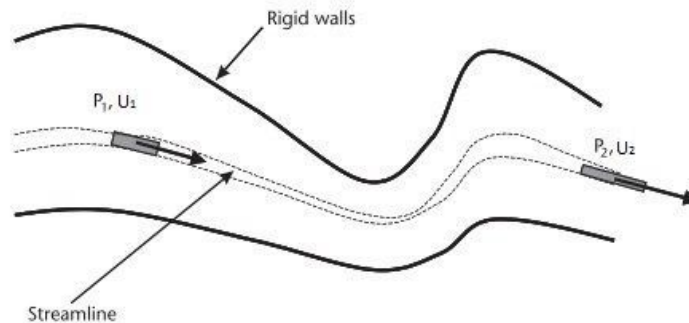


Figure 2.21 - Bernoulli's law: energy conservation along a streamline.  $P$  is the pressure, and  $U$  is the velocity (Berthier et al. 2006).

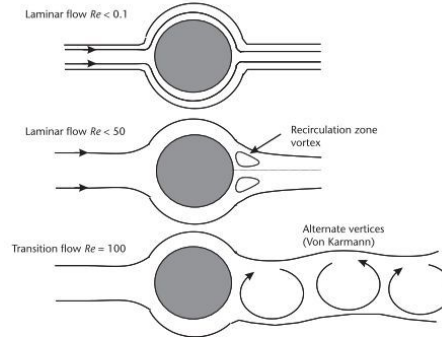


Figure 2.22 - Different patterns of laminar and transitional flows behind a cylinder (Berthier et al. 2006).

A Poiseuille flow occurs when the flow of a Newtonian fluid is steady, fully developed and pressure driven. The no-slip condition imposes zero fluid velocity in the vicinity of the wall due to the influence of viscous forces.

Therefore, the velocity profile for Poiseuille flow is paraboloid (Figure 2.23) and the maximum velocity is achieved in the center of the channel. In a rectangular channel the velocity profile can be approximated by ( 2.4 ) (Shah et al. 1978), where  $u_{max}$  is the maximum velocity,  $a$  and  $b$  the channel dimensions and  $s$  and  $r$  the exponents. The approximation is dependent on the aspect ratio  $\alpha = \frac{b}{a}$  and the final values are generally close to 2 for  $\alpha \leq 0.5$  and yield exponents  $s$  and  $r$  larger than 2 ( 2.5 ). The integration over the duct cross section velocity field results in ( 2.6 ) whose ratio is comprised between 1.5 to 2.

$$u(x, y) = u_{max} \left[ 1 - \left( \frac{x}{a} \right)^s \right] \left[ 1 - \left( \frac{y}{b} \right)^r \right] \quad (2.4)$$

$$s = 1.7 + 0.5 \times \alpha^{-1.4} \quad (2.5)$$

$$r = \begin{cases} 2, & \alpha \leq \frac{1}{3} \\ 2 + 0.3 \times \left( \alpha - \frac{1}{3} \right), & \alpha \geq \frac{1}{3} \end{cases}$$

$$\frac{u_{max}}{U} = \left[ \frac{s+1}{s} \right] \left[ \frac{r+1}{r} \right] \quad (2.6)$$

Pressure is dimensionally an energy-per-unit volume ( $J \cdot m^{-3}$ ). Along the flow occurs a redistribution of energy between pressure, inertia and gravity. The dissipative term due to friction at the wall is given by ( 2.7 ), where  $f$  is the dimensionless Fanning friction factor and  $L$  the duct length. For rectangular

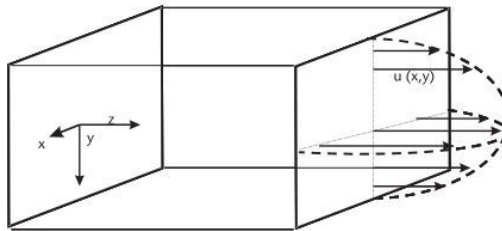


Figure 2.23 – Velocity profile in rectangular duct (Berthier et al. 2006).

ducts the friction factor depending on the aspect ratio ( $\alpha$ ) is given by the numeric approximation ( 2.8 ) (Shah et al. 1978).

$$\Delta P = f \frac{PL}{S} \left( \frac{1}{2} \rho U^2 \right) \quad (2.7)$$

$$f = \frac{24}{Re} (1 - 1.3553\alpha + 1.9467\alpha^2 - 1.7012\alpha^3 + 0.9564\alpha^4 - 0.2537\alpha^5) \quad (2.8)$$

In a fully developed flow, the wall shear stress can be obtained using the Bernoulli approach ( 2.2 ) along the pipe axis, using as dissipative term the friction and dividing the volume to yield ( 2.9 ).

$$\tau = \frac{R_h * \Delta P}{2L} \quad (2.9)$$

#### 2.4.1.4 Diffusion

Diffusion is the process by which a concentrated group of particles in a volume will spread out over time by Brownian motion, so that the average concentration of particles throughout the volume is constant (Beebe et al. 2002).

Microfluidic systems can combine diffusive transport with convective flow of the bulk fluid. The diffusion coefficient,  $D_\alpha$  ( $m^2/s$ ), given by Einstein law ( 2.10 ) for any particle depends on the hydraulic radius of the particle  $R_h$  ( $m$ ), the dynamic viscosity of the fluid  $\eta$  ( $kg.s^{-1}.m^{-1}$ ), the absolute temperature  $T$  ( $K$ ) and the Boltzmann's constant  $k_B$  ( $m^2.kg.s^{-2}.K^{-1}$ ). The dependence of particle hydraulic radius is dependent on the square root of the molecular weight ( $R_h \propto (m)^{\frac{1}{3}}$ ) so the diffusion coefficient for a large protein has about one or two orders of magnitude.

$$D_\alpha = \frac{k_B T}{6\pi\eta R_h} \quad (2.10)$$

Mass transport associated to diffusive transport is given by Fick's first law for steady state, binary ideals solutions with low concentrations and constant density ( 2.11 ), where  $c$  ( $mol/m^3$ ) is the particle concentration and  $J_\alpha^{diff}$  ( $kg.m^{-2}.s^{-1}$ ) the linear variation of the diffusive flux.

$$J_\alpha^{diff} = -D_\alpha \frac{\partial c}{\partial x} = \frac{k_B T}{6\pi\eta R_h} \quad (2.11)$$

From the simplified mass transfer equation, the transient state can be derived (Fick's second law) which at one dimension is given by ( 2.12 ).

$$\frac{\partial c}{\partial t} = D_\alpha \frac{\partial^2 c}{\partial x^2} \quad (2.12)$$

The diffusion of a small concentration burst of a substance in a solvent in a 1D geometry could be approximated to a Dirac dependent on  $x$  axis distance for initial condition. Solving the differential equation on time given the initial condition, results on ( 2.14 ) where the argument denominator represents the characteristic diffusion length  $x_c \approx \sqrt{4Dt}$ .

$$c(x, t_0) = c_0 \delta(t) \quad (2.13)$$

$$c(x, t) = \frac{c_0}{\sqrt{4\pi Dt}} e^{-\frac{x^2}{4Dt}} \quad (2.14)$$



In aqueous diluted solutions for polymer and proteins,  $D_\alpha$  is comprised between  $10^{-11}$  and  $10^{-10} \text{ m}^2.\text{s}^{-1}$  (Cussler 2007).

## 2.4.2 Governing equations

### 2.4.2.1 Continuity equation – Incompressible Fluids

The continuity equation entails the first fundamental equation of fluid mechanics and expresses the conservation of mass in classical mechanics. Considering a mass balance over an infinitesimal volume element  $\Delta x \Delta y \Delta z$  fixed in space, and arranging the expression to obtain the equation the equation of continuity, results in ( 2.15 ).

$$\delta_t \rho = -(\nabla \cdot \rho v) \quad ( 2.15 )$$

The vector  $\rho v$  is the mass flux, and its divergence is the net rate of mass efflux per unit volume. In microfluidic systems,  $\rho$  can be assumed constant in space and time due to low flow velocities, fluid is incompressible and there is a phase maintenance (Bruus 2006) simplifying the continuity equation ( 2.16 ).

$$\nabla v = 0 \quad ( 2.16 )$$

### 2.4.2.2 The Navier-Stokes equation – Incompressible fluids

The behaviour of the fluid particles in the system which they make part of can be explained fluid mechanics equations and can be further deduced by several approaches. One of these approaches is the starts from the Navier-Stokes equation, which describes the motion of fluids, liquids or gases. These equations consider that changes in momentum in infinitesimal volumes of fluid are simply the sum of dissipative viscous forces (friction), the differences in pressure, gravity and other forces acting inside the fluid, which is incompressible under laminar flow conditions with low Reynolds number ( 2.17 ).

$$\rho(\partial_t v + (v \nabla) v) = -\nabla p + \eta \nabla^2 v + f \quad ( 2.17 )$$

In this equation it can be pointed that the term on the left side of the equation is related to inertia, more precisely the first term is associated with the unstable acceleration and the second, the convective acceleration, and the terms on the right side correspond to the pressure gradient, viscosity and other forces, respectively.

### 2.4.2.3 Time-independent phenomena

The analysis of convective diffusive transport in microchannel considers incompressible fluid flow, and convective/diffusive transport of a passively advected scalar field are governed by the continuity, Navier-Stokes and species transport equations.

In this sense and since the whole basis of the simulation system used throughout the project to solve and obtain the velocity and concentration profiles simultaneously is based on the same principles, the following topics will be addressed in a detailed way.

#### 2.4.2.4 Convective-Diffusion equation

Considering an arbitrarily shaped, but fixed, region  $\Omega$  in the fluid (Figure 2.24).

The total mass  $M(\Omega, t)$  inside  $\Omega$  can be defined as an integral volume over the density  $\rho$ , where it has written the infinitesimal integration volume as  $dr$ .

$$M(\Omega, t) = \int dr \partial_t \rho(r, t) \quad (2.18)$$

Respecting mass conservation principle,  $M(\Omega, t)$  can only vary if mass is flowing into or out from the region  $\Omega$  through its surface  $\partial\Omega$ . The mass current density  $J$  in any point in space is given by (2.19), where  $v(r)$  is the Eulerian velocity field.

$$J(r, t) = \rho(r, t)v(r, t) \quad (2.19)$$

Considering the continuity equation and the Navier-Stokes equation for a homogeneous liquid with density  $\rho(r)$  and momentum density  $\rho(r)v(r)$ , the concept of the convection-diffusion equation is now extended to the case of a solution where several fluids are mixed each with density  $\rho_\alpha$ , defined as the actual mass per volume in the solution. The total density of the fluid is referred  $\rho$ , and the fluid velocity  $v$  is also described in terms of the total momentum density of the solution. Combining the continuity equation (2.15) for several homogeneous solutions contributions (2.20) to density still hold for heterogeneous solution (2.21).

$$\rho(r) = \sum_\alpha \rho_\alpha(r) \quad (2.20)$$

$$\delta_t \rho + (\nabla \cdot \rho v) = 0 \quad (2.21)$$

The concentration  $c_\alpha(r, t)$  of the solute is defined as the density fraction (2.22).

The mass current density  $J_\alpha$  for solute  $\alpha$  must be written in terms of a convection current density,  $J_\alpha^{conv}$ , associated to the global velocity field  $v$  of the solution, and a diffusion current density  $J_\alpha^{diff}$ , due to the random motion of the solute relative to the solution.

$$c_\alpha(r, t) = \frac{\rho_\alpha(r, t)}{\rho(r, t)} \quad (2.22)$$

$$J_\alpha = J_\alpha^{conv} + J_\alpha^{diff} = c_\alpha \rho v + J_\alpha^{diff} \quad (2.23)$$

The continuity equation for the solute density  $c_\alpha \rho$  and with the extra current density  $J_\alpha^{diff}$  added to the flux through the surface, can be calculated by (2.24). This equation can be true for arbitrary  $\Omega$  if the integrands are identical (2.25), which with (2.21) can be reduced to (2.26).

$$\int dr \partial_t (c_\alpha \rho) = - \int da n \cdot (c_\alpha \rho v(r, t) + J_\alpha^{diff}) = - \int dr \nabla \cdot (c_\alpha \rho v(r, t) + J_\alpha^{diff}) \quad (2.24)$$

$$\delta_t (c_\alpha \rho) = - \nabla \cdot (c_\alpha \rho v(r, t) + J_\alpha^{diff}) \quad (2.25)$$

$$\rho [\delta_t c_\alpha + v \cdot \nabla c_\alpha] = - \nabla \cdot J_\alpha^{diff} \quad (2.26)$$

In this sense, the diffusion current density is non-zero simply when gradients in the density of the solute is present. For weak solutions, it is only expected the lowest order gradients to play a role, which

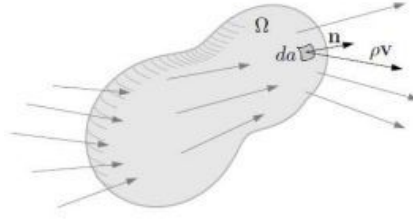


Figure 2.24 - A sketch of the current density field  $\rho v$  flowing through an arbitrarily shaped region. Any infinitesimal area  $da$  is associated with an outward pointing unit vector  $n$  perpendicular to the local surface. The current through the area  $da$  is given by the product of  $da$  and the projection  $\rho v \cdot n$  of the current density on the surface unit vector. (Adapted from (Bruus 2007)).

is expressed by Fick's law ( 2.11 ). Inserting Fick's law into ( 2.26 ), it is obtained the convection-diffusion equation for the concentration  $c_\alpha$  of solutes in weak solutions having a velocity field  $v$ , where the constant  $D_\alpha$ , corresponds to the diffusion constant for solute or in the solvent (Bruus 2007) in ( 2.27 ).

$$\delta_t c_\alpha + v \cdot \nabla c_\alpha = D_\alpha \nabla^2 c_\alpha \quad ( 2.27 )$$

Although there are several methods, such as the finite difference and the finite volume methods, for spatially discretizing differential equations over a solution domain the most common method for solving fluidic problems is the Finite Element Method (FEM). In this project, FEM was considered to solve this system of partial differential equations.

#### 2.4.2.5 Diffusion of momentum and Navier-Stokes

Convection-diffusion flow in the GG is responsible for the mass transport in GG so identifying the influence of momentum diffusion is further investigated. This way, identifying the momentum diffusion in the Navier-Stokes equation, that decelerates Poiseuille flow, where the Navier-Stokes equation can be admitted in a simpler form ( 2.28 ).

$$\rho \delta_t v_x = \eta \nabla^2 v_x \quad ( 2.28 )$$

The momentum density  $\rho v_x$ , results from the diffusion equation from ( 2.12 ) into the form ( 2.29 ), where the kinematic viscosity  $\nu (m^2 \cdot s^{-1})$  ( 2.30 ) is assumed as the diffusion constant for momentum.

Similarly with the ( 2.14 ), there is a momentum diffusion time  $T_0$  for diffusion where the characteristic length  $a$  can be the microchannel radius ( 2.31 ).

$$\rho \delta_t v_x = \eta \nabla^2 v_x \quad ( 2.29 )$$

$$\nu = \frac{\eta}{\rho} \quad ( 2.30 )$$

$$T_0 = \frac{a^2}{\nu} \quad ( 2.31 )$$

Consequently, the dimensionless ratio of the diffusivity  $\nu$  of momentum relative to the diffusivity  $D$  of mass results on the number, denoting as the Schmidt number ( $Sc$ ) ( 2.32 ). The Schmidt number associated with an intrinsic property of the solution, in contrast to the Reynolds number which due to its

dependence on the velocity is a property of the flow (Bruus 2007). In the context, the Péclet number ( $Pe$ ) is the product of the Reynolds number and the Schmidt number ( 2.33 ).

$$Sc = \frac{v}{D} = \frac{\eta}{\rho D} \quad ( 2.32 )$$

$$Pe = \frac{Lv_{avg}}{D} = Re \cdot Sc \quad ( 2.33 )$$

The Peclet number is a dimensionless number relevant in this study, because it relates the rate of advection of a flow to its rate of diffusion. Thus, it is possible to establish a relationship between molecular diffusion time,  $\tau_{diff} = \frac{L^2}{D}$  and the typical hydrodynamic transport time,  $\tau_{conv} = \frac{L}{v_{avg}}$  of a system.

For the canonical example of a simple diffusing species in uniform Poiseuille flow through a uniform circular pipe with no-flux boundary conditions the effective diffusion coefficient is computed. The concentration is assumed to be governed by the linear convective-diffusion equation and concentration and velocity written by a cross-sectional average quantities the effective diffusivity can be determined by ( 2.34 ).

$$D_{eff} = D(1 + \frac{1}{48} Pe^2) \quad ( 2.34 )$$

For high Peclet number ( $Pe > 1000$ ) the diffusion can be ignored, and a pure convection flow dispersion is observed (Huysmans et al. 2005). For low Peclet number ( $Pe < 1000$ ) a convection-diffusion flow dispersion is observed with the increasing influence of the diffusive component that leads to the increase of the bandwidth dependent on time by ( 2.35 ).

$$\tau_{eff} = 4\sqrt{\ln(2)}\sqrt{D_{eff}t} \quad ( 2.35 )$$

## 2.5 Final Considerations

A comprehensive review on the basic principles required to understand the present work were briefly reported. In the first section of this chapter a quick eye anatomy review was made to understand the reasons that make corneal epithelial cells of mice embryos suitable for this type of study. Afterwards the different types of angiogenesis processes were defined to support its importance in physiological conditions and to present the molecular pathway role of two (out of three) major mechanisms, mechanotaxis and chemotaxis, that rule EC migration that provided the motivation for this study.

In the second chapter section the basic the basic physical principles of fluid mechanics and mass transport are described and further deepened to understand the interaction between convection and diffusion in flow. The application of Bernoulli's principle is fundamental to compute the pressure loss along the flow and understand the pressure balance in the microfluidic device. The effect of Taylor dispersion is described to report the effect of shear stress in the effective diffusion coefficient dependent on the Peclet number.

In the third section of this chapter a brief state of the art is made from fabrication to applications of microfluidic device technology. The overview of the applications and characterization of microfluidic devices is made initially to introduce the technology followed by the microfabrication techniques focusing

in soft lithography and PDMS-PDMS bonding. Finally, a brief overview of mixing technique strategies employed are presented to support the gradient generator design.

The state of the art review enables a clearer comprehension of the methodologies adopted in the microfluidic device and methods used for its fabrication and testing.



## 3 Materials and Methods

Following the considerations made in section 2, the microfluidic device was fabricated by soft lithography techniques, mounted, characterized experimentally in the biolab and numerically in CFD models. The microfabrication of a PDMS microfluidic device is composed by three main steps: hardmask patterning, master mold fabrication and replica micromolding. The microfluidic design, fabrication and validation processes required are presented along the next three sections.

Sections 3.2 and 3.3 detail, respectively, microfabrication and bonding processes required for the creation of the microfluidic device. Section 3.4 discretizes the design process and respective assumptions made in the CFD commercial code required for the recreation of suitable models.

Section 3.5 describes the experimental setup conceived to test the microfluidic device and compares it with the idealized conditions simulated in the CFD commercial code. Additionally, the methods required for the CFD analysis are discriminated.

### 3.1 Microfluidic Device Overview

To enable microfluidic device global behavior and individual component testing two setups were considered. A reversible bonding to meet IMM requirements and an irreversible bonding to enable separate component assessment. A presentation of the individual components and both setups is presented in this section to provide a comprehensive view.

The components that compose the microfluidic device are the Shear Stress generator (SS) and Gradient Generator (GG) systems that have a U-shaped form to be produced in PDMS and a PETE membrane to be placed at the intersection of this channels.

The reversible assembly is composed by the placement from bottom to top of SS, PETE membrane and GG whose individual components are presented in Figure 3.1 (a), (b) and (c), respectively. The reversible assembly is depicted in Figure 3.1 (d) and (e). The cells are to be expanded in the PETE membrane facing the SS channel.

The irreversible assembly systems were made replacing one of the device systems for a glass substrate permanently bonded to the remaining device system and PETE membrane which is depicted in Figure 3.1 (f).

### 3.2 Microfluidic Technology

The microfabrication process was followed at Instituto de Engenharia de Sistemas e Computadores - Microsistemas & Nanotecnologias (INESC-MN) facilities, which comprises a 250 m<sup>2</sup> ISO 4 cleanroom for wafer processing according to ISO 14644-1:2015 standard classification. This standard set the air quality parameters (air particles) that are controlled by High Efficiency Particulate Air Filter (HEPA) that filters particles up to 0.3  $\mu$ m. The reproducibility of all the process are ensured by datasheet and initial training provided by INESC-MN investigators and process engineers.

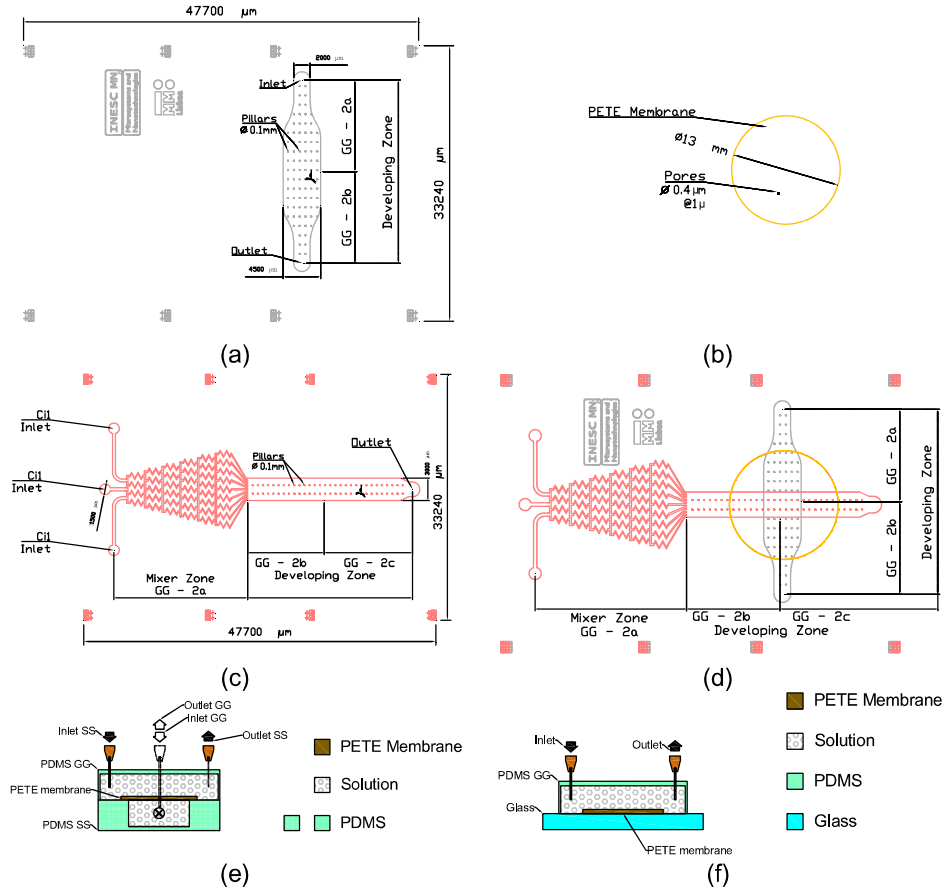


Figure 3.1 – Individual component systems of the microfluidic device: (a) Shear Stress generator (SS), (b) PETE membrane and (c) Gradient Generator (GG). (d) Global view of microfluidic device reversible setup. (e) Section view of microfluidic device reversible assembly. (f) Section view of GG microfluidic device irreversible assembly.

### 3.2.1 Mask Design

The mask design was made in a Computer-Aided Design (CAD) software, AutoCAD® 2017 software according to the INESC-MN good practices:

- mask substrate dimension;
- 5 mm safety margins derived from global fabrication process;
- alignment markers;
- appropriate dimension of mask elements based on the minimum feature size of the microfabrication process;
- several layers according to the microfluidic device component;
- auxiliary elements such as text or dimensions to clarify the drawing.

In the present work, three types of mask design were made, each set with its own specifications and dimensions, according to project requirements. The microfluidic device is composed by the following three elements: the Shear stress generator (SS), the Gradient generator (GG) and the PETE membrane. Table 3.1 summarizes the various SS and GG mask design types and respective characteristic dimensions and features developed during this work.



Table 3.1 – Summary of mask types, features and characteristic features.

Model	Structure	Length $L$ [ $\mu m$ ]	Width $W$ [ $\mu m$ ]	Height $H$ [ $\mu m$ ]	Pillar Diameter $\phi_c$ [ $\mu m$ ]
I	GG	40000	3000	100	NA
II	GG	40000	3000	100	100
III	SS	22100	4500	100	NA
IV	SS	22100	4500	100	100

During the design phase of all structures, the creation of auxiliary elements, such as a scale (or ruler along the length of the microchannel) and larger structures for inlet and outlet are considered good practices. The scale and alignment markers along the microchannel provide component alignment not only during structure handling but also for hole drilling and connector insertion in PDMS structure. Although the present mask design doesn't have a scale, the inclusion of pillar elements equally spaced provide both orientation alignment as well visual auxiliary markers. During the design phase extra care is required when inverting mask. Due to the scale of work the unit measures should be micrometers.

### 3.2.1.1 Gradient Generator

The GG schematic is presented in Figure 3.2 and has external dimensions that fit substrates common work dimension ( $5 \times 5 \text{ cm}^2$ ) and the external structural elements (a margin of at least  $0.5 \text{ cm}$ ) to provide safe handling, peeling and puncture of the PDMS system. The GG is composed by eight alignment marks, three inlets with diameter  $\phi_i = 1500 \mu m$ , one outlet  $\phi_o = 1500 \mu m$ , six levels of stream splitting with  $W_1 = 100 \mu m$  width and  $L_1 = 18100 \mu m$  long and a channel with  $W = 3000 \mu m$  width and  $L_2 = 22300 \mu m$  long. The inclusion of two lines of pillars with diameter  $\phi_c = 100 \mu m$  and longitudinal and transversal spacing of  $S_L = 742 \mu m$  and  $S_w = 1125 \mu m$  is necessary to avoid PDMS channel ablation.

### 3.2.1.2 Shear Stress Generator

The SS schematic is presented in Figure 3.3 and has the same external dimensions and external structural elements describe in the previous section. The SS is composed by eight alignment marks,

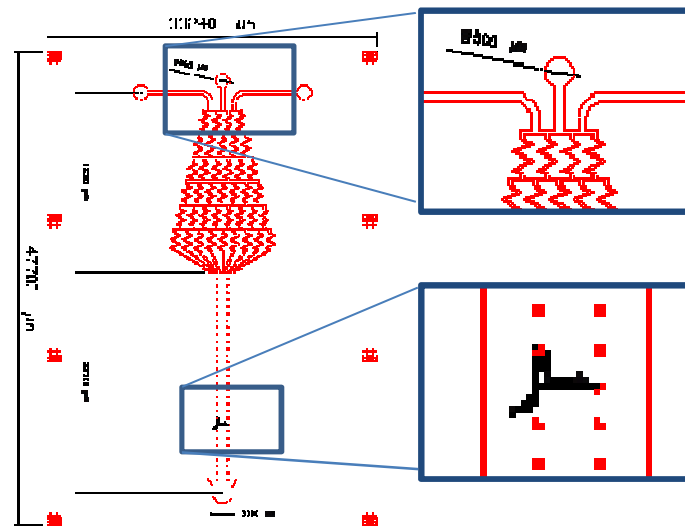


Figure 3.2 – Top view of GG mask schematic, at left global view, at top right middle inlet detail and at bottom right column spacing detail.

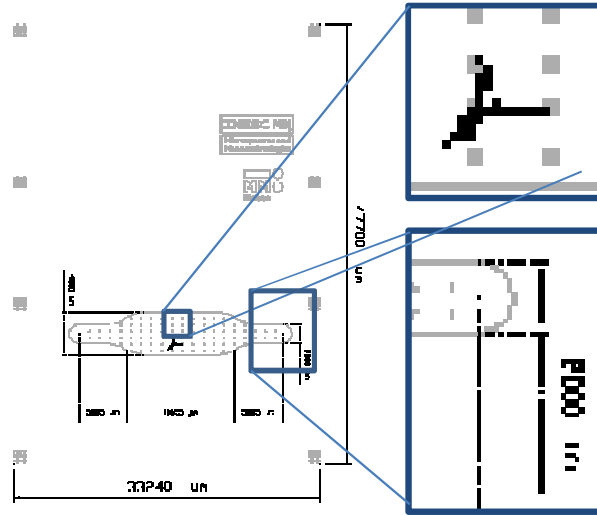


Figure 3.3 – Top view of SS mask schematic, at left global view, at top right column spacing detail and at bottom right outlet detail.

one inlet and outlet with diameter  $\phi_I = \phi_O = 2000\mu m$ , an inlet and outlet developing zones with dimensions  $W_I = W_O = 2000\mu m$  width and  $L_I = L_O = 5525\mu m$  long and a central channel with  $W = 4500\mu m$  width and  $L_2 = 11665\mu m$  long. The inclusion of two lines of columns with diameter  $\phi_c = 100\mu m$ , coincident with the SS, and longitudinal and transversal spacing of  $S_W = 742\mu m$  and  $S_L = 1125\mu m$ , to avoid PDMS channel ablation.

### 3.2.2 Hardmask patterning

To fabricate the master mold that provides the scaffold for PDMS microfluidic device a previous step of hardmask patterning is required. The hardmask patterning can be further subdivided in five steps: (1) glass substrate dicing cleaning and preparation, (2) Aluminum deposition, (3) photolithography, (4) Aluminum wet etching and (5) PR strip.

- 1) The glass substrate dicing, cleaning and preparation is made in the Wet bench of the grey area. The glass substrate used as holder, with dimensions  $50 \times 50\text{ mm}^2$  and diced in DISCO DAD 321 (Figure 3.4 (a)), was washed consecutively during 30 min in Acetone, isopropyl alcohol (IPA), deionized (DI) water in a ultrasound bath at 65°C in MKC22™ (Figure 3.4 (c)) followed by a blow dry. In this step additional care should be taken to avoid the persistence of glue residues.

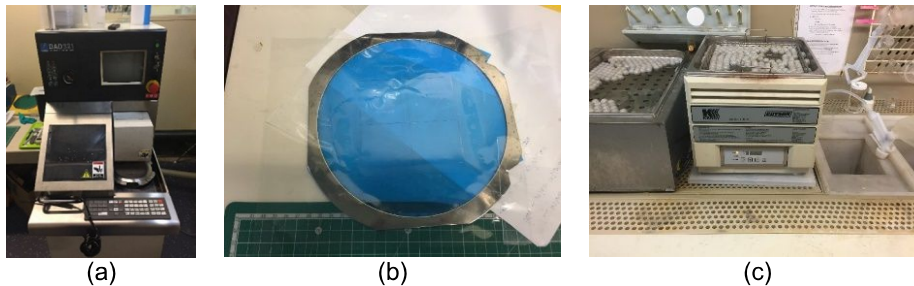


Figure 3.4 - Disco DAD 321 Dicing Saw (DISCO™ 2011). and  $5 \times 5\text{ cm}^2$  glass sample at right. (c) MKC ultrasonic baths MKC22. (Guyson™ 2017).

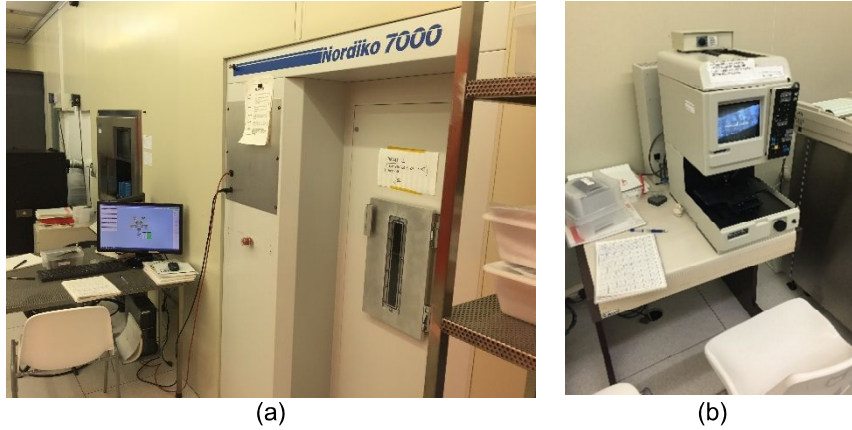


Figure 3.5 – (a) Nordiko 7000 broad ion milling system (Nordiko™ 2014). (b) Dektak 3030 profilometer at right (Dektak™ 2001).

- 2) The Aluminum deposition is performed in a clean room environment. The glass is fixed with duct tape, then placed at Nordiko™ 7000 (Figure 3.5), with the following program Mod 4 Function 8, 2 kW power, air flux of 50.0 sccm and pressure of 2.9 mTorr with the run 20212. After the deposition the duct tape is removed, and the substrate checked at a profilometer to access the thickness of the sample (Figure 3.5).

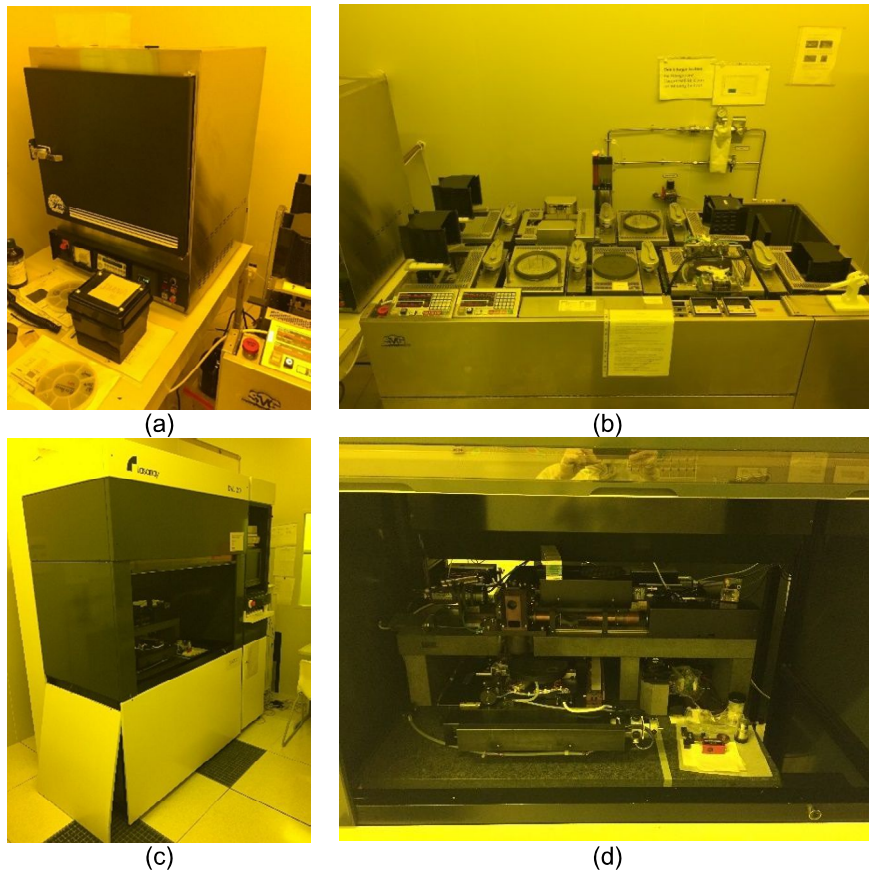


Figure 3.6 – (a) Vacuum Bake/Vapor Prime System, Yield Engineering Systems (Yield Engineering Systems™ 2017). (b) SGV 88 series track system C&D Semiconductor Services (C&D Semiconductor Services™ 2017). Direct Writer Laser (DWL) lithography 2.0 system Lasarray, (c) global view and (d) sample holder in detail.

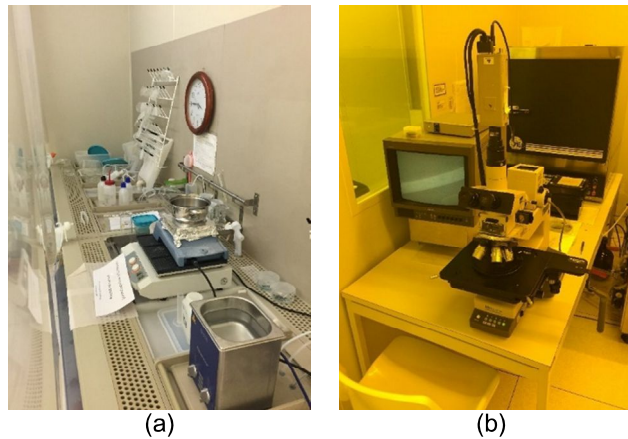


Figure 3.7 – (a) Wet bench in clean room. (b) Olympus BH3-MJL optical microscope (Olympus™ 2000) .

- 3) The photolithography starts by a simultaneous “one-stop” substrate dehydration and hexamethyldisiloxane (HMDS) deposition. It is performed in Vapor Prime Oven for 30 *min*, with a 5 *min* spraying HMDS and baking to improve the adhesion of the resist (an organic compound) to the substrate (a non-organic substrate) in Vacuum Bake/Vapor Prime System, Yield Engineering Systems™, Inc (Figure 3.6 (a)). The 1.5  $\mu\text{m}$  of positive PR coating was done at a SGV™ 88 series track system (Figure 3.6 (b)) with the recipe 6/2 at coating track, spinning for 5 *s* at 0.8 *krpm*, followed by 30 *s* at 2.6 *krpm* and a final soft-bake at 85°C for 1 *min*. The sample was exposed in Direct Writer Laser (DWL™) lithography 2.0 system (Figure 3.6 (c)), using a 90 *mW* power, 422 nm wavelength laser (near Ultraviolet light (UV)) with energy indicator of 65 and focus +30. The development step was made is done at a SGV™ 88 series track system (Figure 3.6 (b)) with the recipe 6/2 at coating track, baking at 110°C for 1 *min*, cooling for 30 *s* and a development for 1 *min*. To verify a correct development the sample was checked in the Olympus™ microscope BH3-MJL (Figure 3.7 (b)).
- 4) The Aluminum wet etching was performed at the wet bench of the clean room. The Aluminum etchant is TechniEtch™ Al 80 MOS at room temperature for 3.5 *min* and agitation with ultrasounds (Figure 3.7) followed by a DI water washing and compressed air drying.
- 5) The PR strip was performed in the wet bench of the grey area. The glass substrate cleaning was made with Microstrip™ 3001, 65°C and ultrasounds bath (Figure 3.4 (c)) for 20 *min*. A final washing was made using IPA, DI water and a compressed air drying.

### 3.2.3 PDMS molding

PDMS molding requires the fabrication of a master mold that was performed in the biolab facility. The process is composed by several steps. Starts with the Silica substrate cleaning and preparation, followed by a dehydration bake, SU-8 pouring and substrate spinning, a pre-bake and soft bake, an UV exposure with the previous hardmask, a post-exposure bake, a development step and final cleanup. Apart from the Silica substrate cleaning and preparation that is performed in the wet bench of the grey area, the remaining steps are done in the biolab facilities.



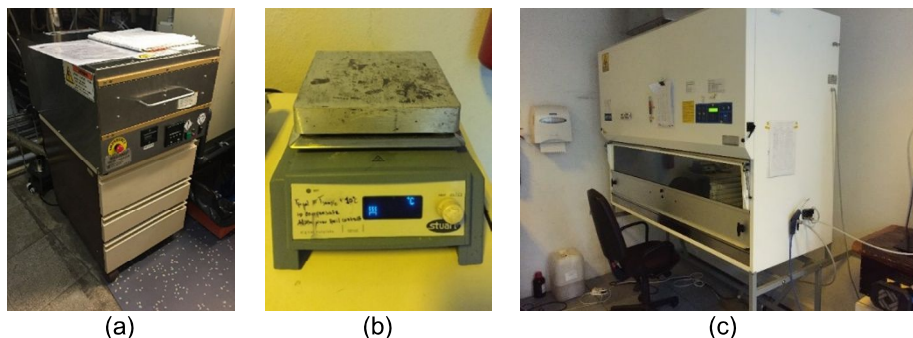


Figure 3.8 – (a) JeLight UV cleaning machine 144AX (JeLight™ 2015). (b) Stuart digital hotplate SD160 (Stuart™ 2017). (c) FASTER BSC-EN laminar flow hood (FASTER™ 2017).

The Silica substrate was washed consecutively during 30 *min* in Alconox solution, deionized (DI) water in a ultrasound bath at 60°C in MKC22™ (Figure 3.4 (c)) followed by a blow dry and an UVO cleaning (Figure 3.8 (a)) during 15 *min*.

A dehydration bake was performed in a hotplate (Figure 3.8 (b)) at 110°C during 5 *min* followed by a cooling step to room temperature.

The SU-8 50 negative resist (MicroChem, n.d.) Figure 3.9) pouring on the Silica substrate and two spinning steps were performed. The first one was performed at rotational speed of 500 *rpm* during 10 *s* and with rotational acceleration of 100 *rpm/s* and the second one at rotational speed of 1200 *rpm* during 30 *s* and with rotational acceleration of 300 *rpm/s* to ensure a SU-8 resist thickness of 100  $\mu\text{m}$ .

In the hotplate (Figure 3.8), a pre-bake step of 10 *min* at 65°C was conducted, followed by a post-bake of 30 *min* at 95°C and finishing with a cooling step of 10 *min*.

An UV-exposure (Figure 3.10) was made on the SU-8 on Silica substrate protected by the hardmask used in the previous section. The two samples were aligned and fixed using duct tape to the polymer holder. The exposure was made at during 74 *s* with a 5.95  $\text{mW} \cdot \text{cm}^{-2}$  radiance.

A post-exposure bake was done in the hotplate (Figure 3.8), with a pre-heat of step of 1 *min* at 65°C was conducted, followed by a post-exposure bake of 10 *min* at 105°C and finishing with a cooling step of 10 *min*.

The development of the SU-8 mold was performed with Polyglycidyl methacrylate (PGMA Figure 3.10) during 10 *min* with manual agitation, followed by an IPA rinse a blow air dry. The samples were

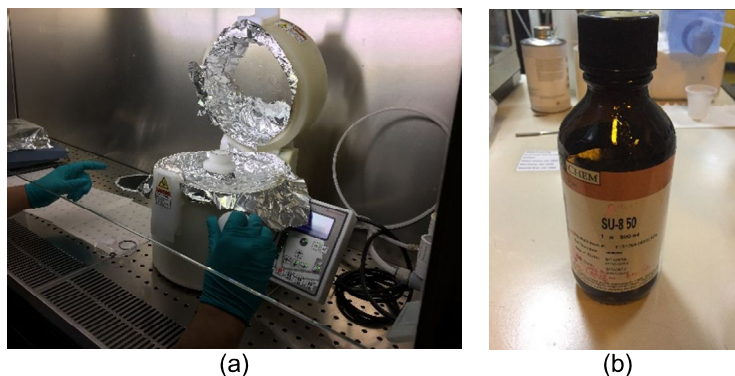


Figure 3.9 – (a) Laurell WS-650-23 Spin Coater at left (Laurell™ 2017). (b) MicroChem SU-8 50 (MicroChem™ 2000).

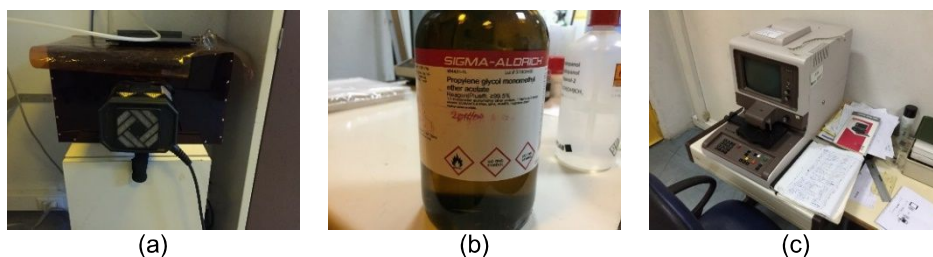


Figure 3.10 – (a) UV 800W Curing Flood Lamp from UV technology limited (UV-light Technology™ 2017). (b) Sigma-Aldrich Poly(glycidyl methacrylate) (Sigma-Aldrich™ 2017). (c) Profilometer – Tencor Alpha Step 200 at right (Tenkor™ 2015).

placed at the profilometer (Figure 3.10) to assess the effective thickness of the SU-8 resist on the Silica substrate.

### 3.2.4 Replica Molding

The PDMS devices for SS and GG were prepared in a mold consisting of two SU-8 molds onto 2" Si plus one PMMA plate for mold thickness. The SU-8 mold is fabricated by soft lithography and the PMMA plate is fabricated by micromilling.

The PDMS molding is composed by the following steps who can be performed in parallel starting with PDMS preparation, mold cleaning, scaffold assembly, scaffold filling, baking and peeling and mold cleaning. Except for the mold cleaning step that is performed in the wet bench, the remaining steps are done in the biolab facilities.

The PDMS molding starts with the PDMS formulation Sylgard™ 184, which is composed by a liquid silicon rubber base and a curing agent. The base and curing agent were measured (Figure 3.11) in a 10: 1 ratio by weight, according to the Sylgard 184 silicone elastomer datasheet (Figure 3.11), and mixed thoroughly by hand for about 1 min. The mixture was degassed in a vacuum desiccator (Figure 3.12 (a)) until all air bubbles were removed.

The Silica mold substrate was washed consecutively using IPA and DI water followed by a blow dry.

The master mold was assembled with duct tape to a micromachined PMMA plate to ensure the correct PDMS height and lateral dimensions (scaffold). The PDMS was poured over the scaffold after

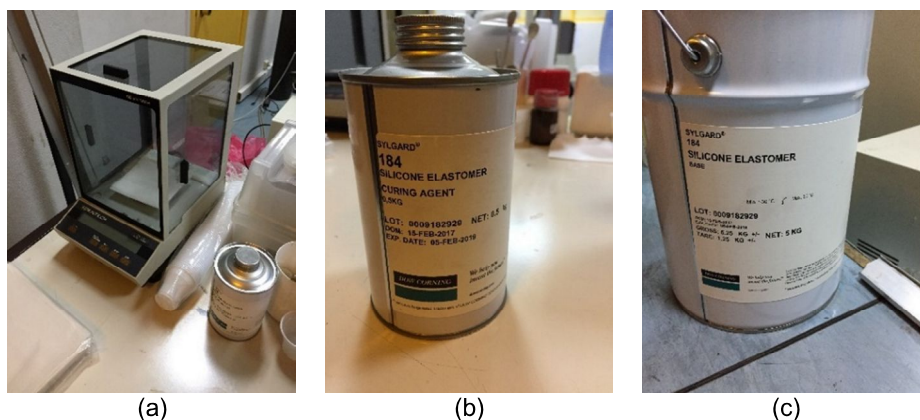


Figure 3.11 – (a) Scientech laboratory balance SA-80 (Scientech™ 2017). Sylgard® 184 Pack with elastomer (b) curing agent (Dow Corning™ 2017b) and (c) silicone elastomer base (Dow Corning™ 2017a).

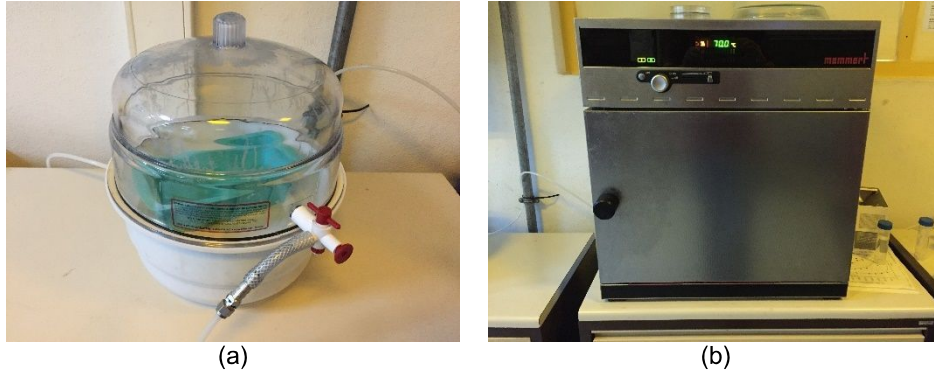


Figure 3.12 – (a) Bel-Art vacuum desiccator (Bel-Art™ 2017). (b) Memmert Universal Oven (Mettmert™ 2007).

degassing and placed in the oven at 70°C for 2 h (Figure 3.12 (b)). After curing the elastomer, the crosslinked PDMS was removed from the scaffold using a cutter and tweezers paying extra care to the borders to avoid PDMS residues in the scaffold. Using a needle with size equal to or below the metal connectors used, holes in the PDMS at the inlet and outlet areas were made in the GG by turning gently to stick and remove.

The Silica mold substrate was first cleaned, removing persistent PDMS residues from the peeling and washed consecutively using IPA and DI water followed by a blow dry to enable further use.

### 3.3 Assembly Techniques

For testing purpose, two types of microfluidic assemblies were considered to ensure the constitution of a reversible assembly that fit the needs of the final device and an irreversible assembly that could provide the maintenance of the laboratorial conditions required for its complete study.

Micromilling is a subtractive fabrication process that relies in rotating cutting tools to remove the bulk material. The cutting tools (e.g. endmill or drill) move along a worktable with the workpiece in the XY directions (horizontal plane) and a spindle to secure, rotate and positioning the cutting tool in the Z direction (vertical direction) (Figure 3.13 (a)). For a micrometric scale the milling control is a CNC (computer numeric control) that enables automation, repeatability and precision. The geometric patterns can be configured through the conversion of a CAD drawing to make directly the microfluidic channels or the molds used in other fabrication techniques.

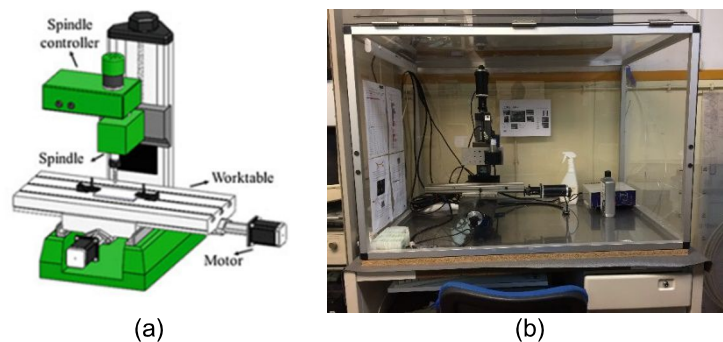


Figure 3.13 – (a) Schematic of micromilling fabrication processes. (adapted from Silverio and Freitas 2018). (b) Micromilling machine of INESC-MN.



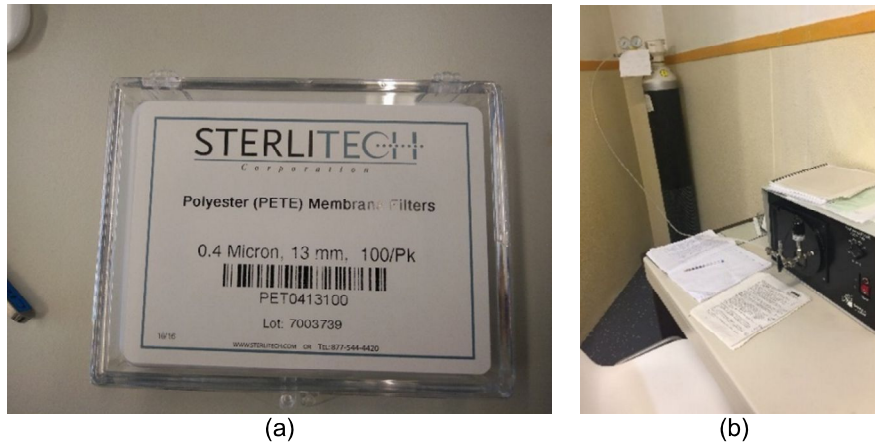


Figure 3.14 – (a) SterliTech PETE Membrane Filters ((SterliTech™ 2017)). (b) Harrick Plasma Cleaner PDC 002 (Harrick Plasma™ 2017).

The irreversible assembly accomplished by bonding in the UVO cleaner while the reversible assembly is achieved by mechanical sealing of the PMMA holder micromachined.

For irreversible assembly microfluidic device, the PDMS structures were washed consecutively using IPA and DI water followed by a blow dry. Afterwards, GG and PETE membrane (Figure 3.14 (a)) were placed at the Plasma Cleaner (Figure 3.14 (b)) during 45 s at medium intensity with the contact surface for bonding facing up. The exposed surfaces were aligned and placed in contact to match the final mounting. A secondary surface plasma treatment was repeated to bond the coupled components (GG and PETE membrane) to SS. The device was stored for 24 h prior to use to enable an effective bonding.

The reversible assembly microfluidic device consisted in a previous washing step consecutively using IPA and DI water followed by a blow dry. A second step of alignment of SS, PETE, GG in the PMMA holder and finally, the components were mechanical sealed tightening a set of screws.

### 3.4 CFD Simulation

Presently available CFD solutions are a valuable tool to predict for simulate microfluidic devices behavior that contribute for its efficient and optimized design.

Several solutions are only possible due to the incorporation of complex channel geometries whose optimization is possible at a numerical level. These solutions avoid the fabrication of all iterative steps taken to achieve the final design with the right geometry, material properties, boundary conditions and numerical discretization it is possible to predict at some extent the behavior of the microfluidic device.

These models reproduce a compromise between the computing power required and the accuracy gain. This way model simplifications are acceptable provided that experimental validation is made, and the dominant physical effects are included on analysis assumptions.

To compute the shear stresses and concentration gradients experienced by the EC on the microfluidic device through the project, CFD commercial software was used. The microchannel was designed in the software or imported from CAD Software and was used to define both Subdomain and Boundary Settings. After, simulation computation its results were adjusted in post-processing. The simulations were computed in a laptop with an Intel(R) Core(TM) i7 CPU Q 740 with 4 cores processors with 1.73GHz each.



According to this experimental setup, two model types must be considered, one with mass transport to access the concentration gradient sensed by the EC through the PETE membrane pores and concentration profile along an alignment and other to study the shear stress distribution along the EC for a given flow according to a determined cell distribution. Four models were used to study the transient pore diffusion which took approximately 4 h for model. Sixteen CFD models were used to study the concentration profile gradient along alignments that took approximately 6 min each. Eight CFD models were used to access the wall shear stress in EC which took 12 h for computation.

## 3.5 Experimental Setup

As referred in section 2.1.2.5 chemotaxis plays a role in the EC migration modulating the direction toward a gradient of soluble chemoattractant. In this context, one of the objectives of this study was the creation of a steady-state gradient, to validate the effect of the molecular gradient along the microchannel width extension of the GG.

### 3.5.1 Generation of stable gradient using dye solution

To obtain the generation of gradients in the microchannel of the microfluidic structure, initially a computational fluid dynamics simulation was made in a CFD commercial software.

In the experimental context, the PDMS devices, which fabrication process was described previously in section 3.2, were tested with DI water and Rayner's™ blue dye (Figure 3.15 (a)). All experiments were performed with an inverted microscope from Olympus™ and incorporated digital color camera Olympus XC30 (Figure 3.15 (b)).

Room temperature was controlled at 22 °C. The cleaned device was inserted on the microscope. In this device, settled with an irreversible assembly setup, polyethylene tubes (Instech Solomon™) were inserted on the GG outlet and inlets metallic connectors, with an Eppendorf™ tube for waste (Figure 3.16). The syringe pumps (NE-300, SyringePump.com™) (Figure 3.15 (c)), that were previously calibrated for the syringe diameter, (U-100 Insulin, 1mL d 4.1 mm, Codan™) were placed in the inlets with the flow rates ranging from 0.6 – 120  $\mu\text{L} \cdot \text{min}^{-1}$ .

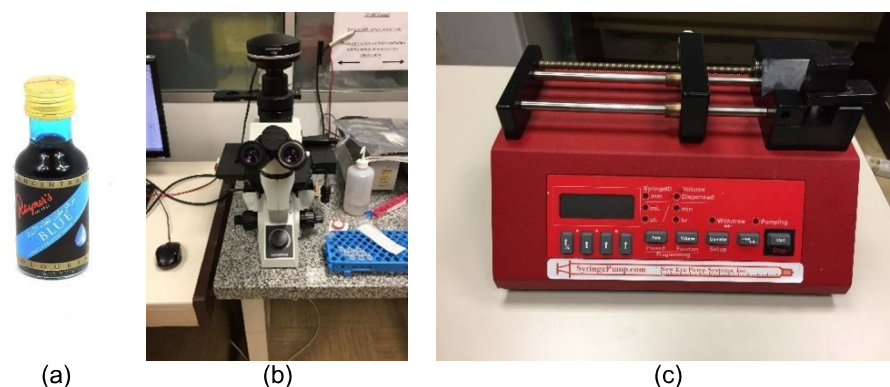


Figure 3.15 –(a) Rayner's blue concentrated dye (Rayner's™ 2011). (b) Olympus XC30 camera (Olympus™ 2017) coupled with inverted microscope model from Olympus. (c) Syringe pump from NE-300 SyringePump.com (SyringePump.com™ 2017).

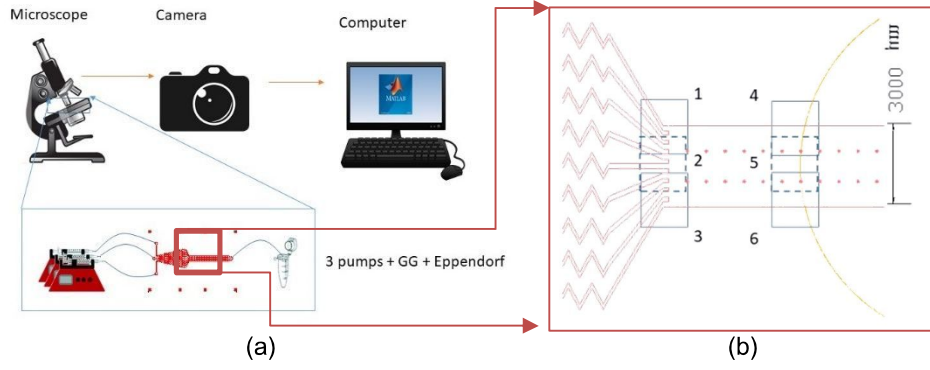


Figure 3.16 – (a) Schematic illustrating the standard experimental setup for GG microfluidic device at left. (b) Images taken with microscope field of view at right.

The microchannel device was focused on microscope with the larger possible field of view (FOV) 4X magnification. The process of filling was made from the entrance of the inlet. It was considered a settling time of 1 min. To observe the GG main microchannel two alignments were chosen, the first at the mixer exit and the second at the membrane entrance. Three pictures per alignment had to be taken considering a superposition area between consecutive pictures since the FOV didn't cover all channel extension (Figure 3.16 (b)).

In these experiments an exposure time of 540 ms was used to minimize photobleaching. Each image was post-processed in MATLAB 2015 (b) for:

- aligning the consecutive images using reference points;
- computing the intensity ( $I_i$ ) using the RGB intensity along a given alignment ( 3.1 ) for the pure DI water solution and non-mixed concentrated solutions with concentrations ranging from 1:1 to 1:200;

$$I_i = \frac{0.2126 \times R + 0.7152 \times G + 0.0722 \times B}{3} \quad (3.1)$$

- computing the relative intensity ( $\frac{I_i}{I_0}$ ) of a concentrated solution relative to the correspondent DI water solution along a given alignment homogenizing the results for a constant length vector;
- computing relation between the image intensity ( $I$ ) and the concentration of known solutions ( $c_i$ ) using an exponential relation ( 3.2 ). Note that the brightness was homogenized relative to a DI water solvent ( $I_0$ ).

$$\frac{I}{I_0}(c_i) = a + b \times e^{-c \cdot c_i} \quad (3.2)$$

- estimating the concentration of an unknown concentration profile in the mixer due to a combination of different inlet concentrations and flow rates using the relation ( 3.2 ) computed.

The experimental setup overview can be observed in Figure 3.17.



Figure 3.17 – Experimental setup for the gradient generation determination, microfluidic device zoomed at left and global overview at right.

The inlet concentrations and flow rates considered both for the calibration step and for the gradient determination are summarized in

Table 3.2.

Table 3.2 – Inlet concentration and flow rates for the calibration step (left) and for the gradient determination (right).

Calibration Step	Inlet Concentration $\{c_{I1} ; c_{I2} ; c_{I3}\}$	Inlet Flow Rate $[\mu L \cdot min^{-1}]$	Gradient Test	Inlet Concentration $\{c_1 ; c_2 ; c_3\}$	Inlet Flow Rate $[\mu L \cdot min^{-1}]$
1	{0 0 0}	9,000	1	{1:1 1:10 1:100}	0,600
2	{1:200 1:200 1:200}	9,000	2	{1:1 1:10 1:100}	9,000
3	{1:100 1:100 1:100}	9,000	3	{1:1 1:10 1:100}	63,0
4	{1:20 1:20 1:20}	9,000	4	{1:1 1:10 1:100}	120,0
5	{1:10 1:10 1:10}	9,000	5	{1:2 1:20 1:200}	0,600
6	{1:2 1:2 1:2}	9,000	6	{1:2 1:20 1:200}	9,000
7	{1:1 1:1 1:1}	9,000	7	{1:2 1:20 1:200}	63,0
			8	{1:2 1:20 1:200}	120,0

### 3.5.2 Generation of a stable shear stress

The flow rate was determined for both the GG and the SS to measure the average velocity and to determine indirectly the shear stress at the microfluidic device walls. The average flow rate was determined measuring the mass of DI water in the Eppendorf™ placed at the outlet and considering the average water density at the room temperature 22°C to compute the water volume and dividing it by the elapsed time during the experiment according:

$$V_i = \frac{m_{fi} - m_{ii}}{\rho} \quad t_i = t_{fi} - t_{ii} \quad Q_i = \frac{V_i}{t_i} \quad (3.3)$$

The experimental setup for both the SS and GG can be observed respectively in Figure 3.18 and Figure 3.19.

The flow rates set at the inlets were made to match the channel cross section average velocities and are presented along with the estimated time to fill the 1mL Eppendorf™ in Table 3.3.

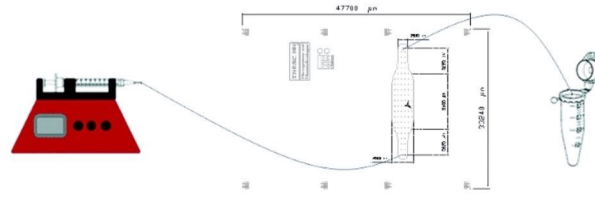


Figure 3.18 – Experimental setup for flow estimation in Shear Stress Generator with dimensions  $4500 \times 100 \mu\text{m}^2$ .

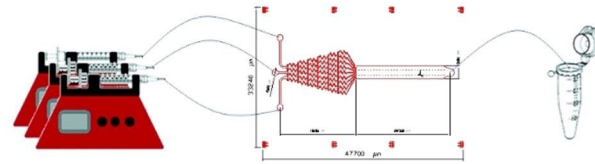


Figure 3.19 – Experimental setup for flow estimation in Shear Gradient Generator with dimensions  $3000 \times 100 \mu\text{m}^2$ .

Table 3.3 – Microchannel average velocity, individual inlet flow rate and estimated filling time for 1 mL volume.

GG Test	Average Velocity [mm. s <sup>-1</sup> ]	Inlet Flow Rate [uL. min <sup>-1</sup> ]	Filling Time [min]	SS Test	Average Velocity [mm. s <sup>-1</sup> ]	Inlet Flow Rate [uL. min <sup>-1</sup> ]	Filling Time [min]
1	0,1	0,6	555,0	1	0,1	2,7	370,4
2	1,5	9	37,0	2	1,5	40,5	24,7
3	10,5	63	5,3	3	10,5	283,5	3,5
4	20	120	2,8	4	20	540	1,9

## 3.6 Final Considerations

A brief description of the design assumptions, and fabrication process of the microfluidic device were depicted in this chapter. The first section is devoted to the fabrication process composed by hardmask patterning, mold fabrication and PDMS casting. The process starts with the hardmask patterning of Aluminum in a glass substrate through a photolithography process developed in a clean room environment providing the 2D geometry. This hardmask is used in a subsequent photolithography process to enable the creation of a master mold in a resist (SU-8) that provides the volumetry of the mold. Finally, the PDMS is poured in the master mold enabling several replica molding.

The second section describes the reversible or irreversible assembly of the microfluidic device that and the aim of the development of the latter device that enabled the reproducibility of the experiments.

The third section was dedicated to the computational simulation of the microfluidic device components. The pre-design considerations made, and the simplifications assumed are depicted establishing a compromise between computing power and model accuracy.

Finally, the fourth section describes the experimental setup and respective procedures, that provides the validation of the project requirements.

The shear stress experienced by the EC is assessed indirectly through the flow rate measurements and channel geometry discrimination. The concentration gradient along a channel alignment is assessed through image processing analysis with an initial calibration. The microscope FOV limited the direct assessment of the concentration profile that had to be tackled with an initial processing step.



## 4 Results and Discussion

In this chapter, the fabrication, design and validation processes of the microfluidic device will be detailed with the presentation of the results.

The three main process steps of PDMS microfabrication are characterized in the section 4.1 namely the hardmask patterning, PDMS molding and replica molding. Section 4.2 is devoted to the CFD simulation of microfluidic device to estimate the mass transport at a microscale in the membrane pores in the GG and the shear stress sensed by an array of cells in the SS. Finally, in section 4.3 the validation of the physical processes is detailed in the experimental setup.

### 4.1 Microfluidic Technology

The first objectives of this work include the design and fabrication of a microfluidic device using Soft Lithography. The fabrication of a PMMA holder that enabled the mechanical sealing of the microfluidic device resorted to micromilling described in section 3.3. The material chosen for microfluidic device fabrication was PDMS due to rapid prototyping, low cost, competent mechanical and optical properties and biocompatibility as described in section 2.3.1. The microfluidic device components are depicted in Figure 4.1 as well as the hydraulic circuit sections along with its geometric properties.

Additionally, for experimental purposes the individual structures were chemically bonded to PETE membrane and glass substrate using plasma cleaner (Figure 3.14 (b)) accordingly section 3.3. A global overview of the microfluidic technology process is presented in Figure 4.2 for SS and GG components.

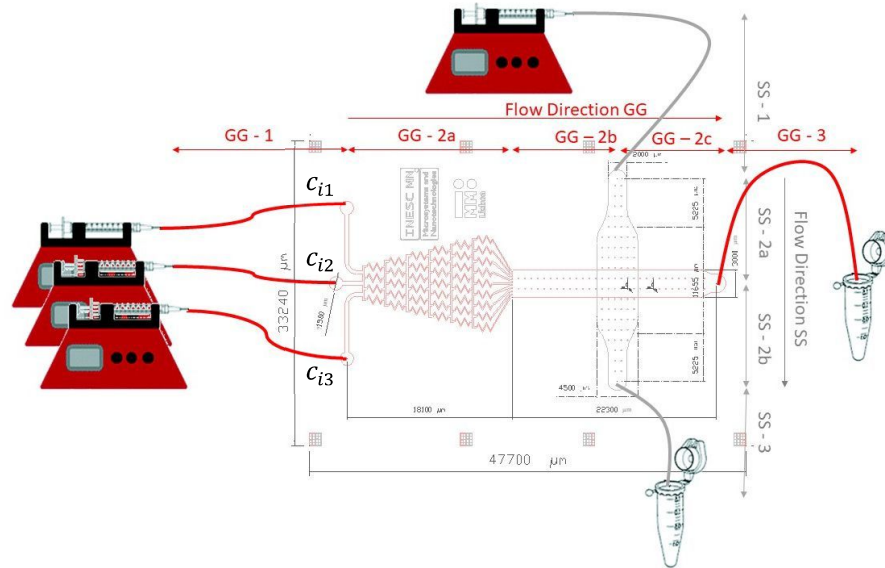
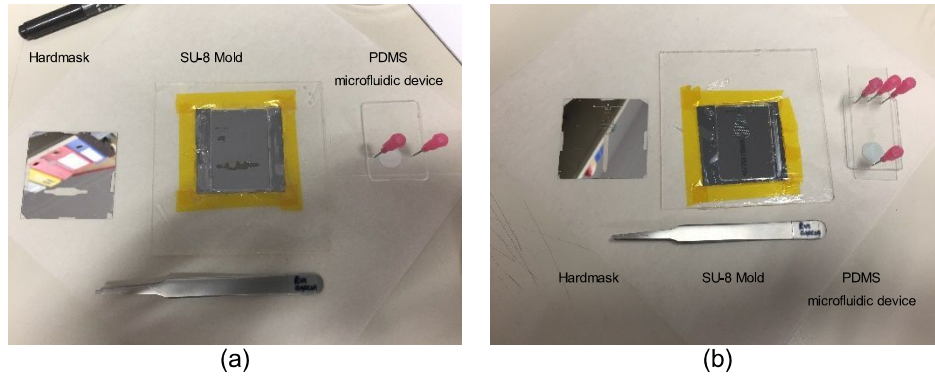


Figure 4.1 – Top view of microfluidic device. The hydraulic circuit model simplification is defined by section of the Microfluidic device. In red GG sections, in grey the SS sections and in yellow the PETE membrane.





*Figure 4.2 – (a) Microfluidic technology auxiliary components (Hardmask, SU-8 mold and PDMS microfluidic device) for SS. (b) Hardmask, SU-8 mold and PDMS microfluidic device for GG.*

The inclusion of anti-fouling pillars was a strategy adopted both in GG and SS PDMS systems to avoid channel ablation due to the large width to height ratio in the cross section, respectively 30: 1 and 45: 1, and the membrane deflection on the PDMS systems intersection. The intricate network created in the GG improves the mixing efficiency since the shear stress involved have a spanwise component that enhances the diffusion. The GG and SS systems are disposed in a perpendicular way, so the concentration gradient imposed by GG on the PETE membrane and shear stress imposed by SS have opposite directions enabling the study of simultaneous modulation of mechanotaxis and chemotaxis in EC.

#### 4.1.1 Hardmask patterning

The first step in the hardmask patterning consisted in the glass substrate cleaning and preparation performed at the wet bench and where the appearance of residues on the substrate should be avoided at any cost. The second step consisted in the deposition of a 1500 Å Aluminum film on the glass substrates (Figure 4.3) at Nordiko™ 7000 (Figure 3.5). A dummy sample scratched with a marker was made to access the layer thickness.

Photolithography process starts with resist deposition at the SVG™ 88 series track system (Figure 3.6 (b)), followed by an UV-light exposure in the DWL™ lithography 2.0 system (Figure 3.6 (c)) and development at SVG™ 88 series track system. The sample structure development was verified in Olympus™ microscope BH3-MJL (Figure 3.7 (b)) and is presented in Figure 4.4.



*Figure 4.3 – Al deposit in glass substrate.*



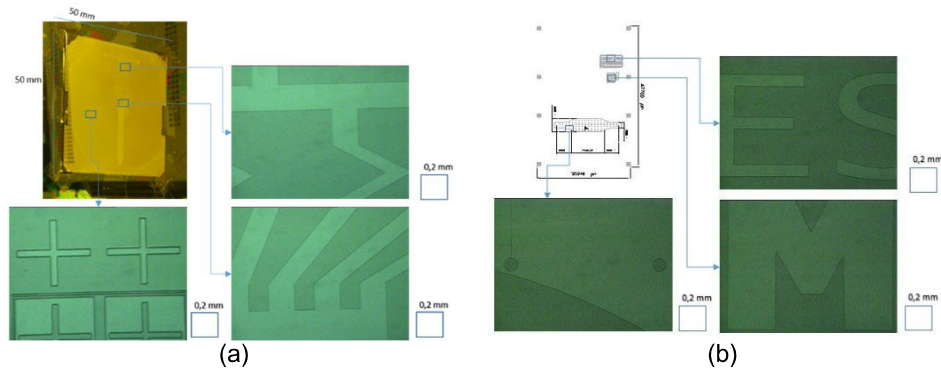


Figure 4.4 – Glass substract after photolithography and some structure details at optical microscope for GG (a) and SS (b).

The Aluminum wet etching was performed with TechniEtch™ Al 80 MOS at the wet bench of the clean room (Figure 4.5 – (a) and (d)). The PR strip was performed with Microstrip™ 3001 in the wet bench of the grey area followed by a final washing with IPA, DI water and a compressed air drying (Figure 4.5 – (c) and (f)).

As it can be observed in Figure 4.4 and Figure 4.5 the definition of the smaller 2D structures were all defined since the m.f.s. is around  $100\text{ nm}$  and the m.f.s. of the SS and GG is about  $5000\text{ nm}$  in the anti-fouling pillars.

### 4.1.2 PDMS Molding

PDMS molding starts with the Silica substrate cleaning and preparation in the wet bench of the grey area, by a dehydration bake in a hotplate (Figure 3.8 (b)) and finally by a cooling step. The SU-8 resist is poured in the cooled Silica substrate and then subjected to a spinning process that defines the film thickness. The Silica substrate is subjected to a pre- and soft-bakes to evaporate the solvent to make the SU-8 photoresist more solid.

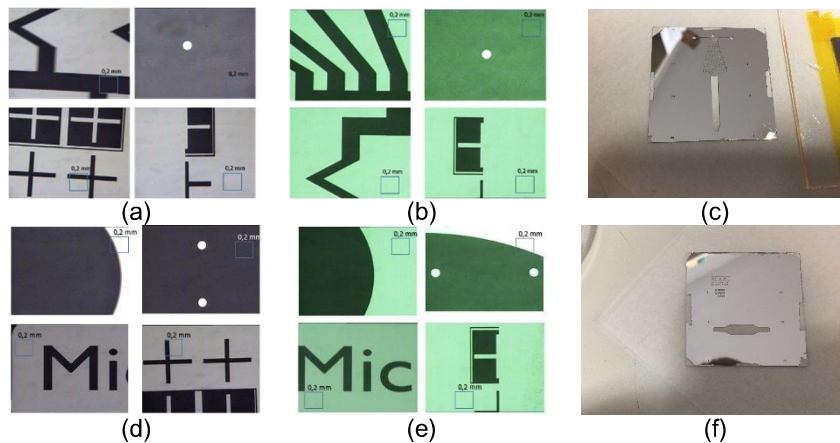
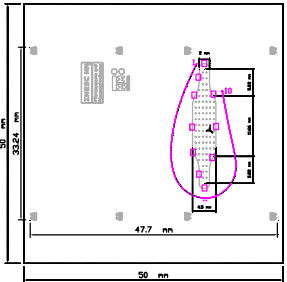
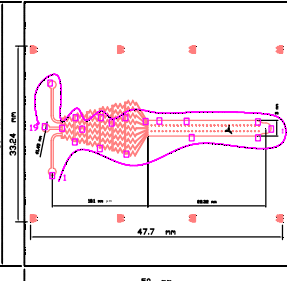


Figure 4.5 – Glass substract after aluminium wet etching and some details at optical microscope respectively for GG (a) and SS (d). Hardmask after photoresist strip and some details at optical microscope respectively for GG (b) and SS (e). Hardmasks final aspect respectively for GG (c) and SS (f).

To define the microchannels pattern, an UV exposure (Figure 3.10 (a)) with the hardmask made previously is performed, followed by a post-exposure bake. A development step with PGMA was made to reveal the microchannels patterns after which a final cleanup was made.

The microchannels height and width were verified at the profilometer (Figure 3.10 (c)) to assess the effective thickness of the SU-8 on the Silica substrate. The average thicknesses of the SS and GG samples were respectively  $th_{SS} = 108,0 \mu m$  and  $th_{GG} = 97,8 \mu m$  whose measurements can be observed in Table 4.1.

*Table 4.1 – SU-8 on the Silica Substrate profilometer assessment points on SS sample in top picture and on GG sample in bottom picture. The pink arrow indicates the order and place of the sample observations.*

Observation	Sample SS $th [\mu m]$	Sample GG $th [\mu m]$	Sample SS on top Sample GG on bottom
1	104,0	101,5	
2	108,0	103,0	
3	104,0	105,3	
4	109,2	106,8	
5	112,4	90,6	
6	109,4	83,7	
7	108,2	86,8	
8	107,1	103,8	
9	107,0	86,2	
10	106,4	86,1	
11		103,9	
12		104,6	
13		111,2	
14		110,2	
15		84,8	
16		86,9	
17		85,6	
18		107,4	
19		109,3	
Average	108,0	97,8	

The SS sample thickness is slightly larger due to the fact that the initial protocol consider a thickness of  $150 \mu m$  of SS sample, that had to be corrected for lower values due to the SU-8 50 limitations (MicroChem™ 2000) comprehended between 50 to  $120 \mu m$ . Several procedures like velocity spinning adjustments and two steps SU-8 deposition and exposure were taken to override this limitation with little success. The smaller structures like the anti-fouling columns and mixer microchannels have a good resolution as depicted in Figure 4.6 and didn't show greater distortion at the edges. The final aspect of SU-8 resist molds in Si substrate is presented in Figure 4.7 (b) and (c).

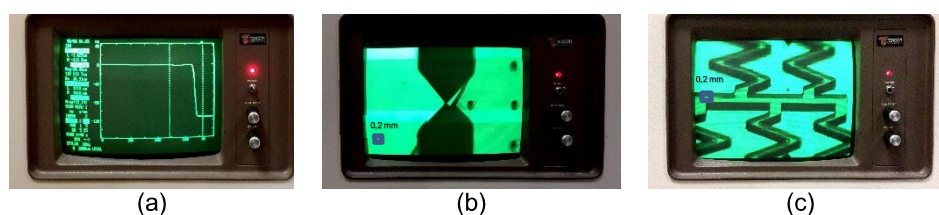


*Figure 4.6 – Profilometer measurement in GG sample at left. Profilometer tip in SS sample structure border at middle. GG sample detail on the mixer area at right.*

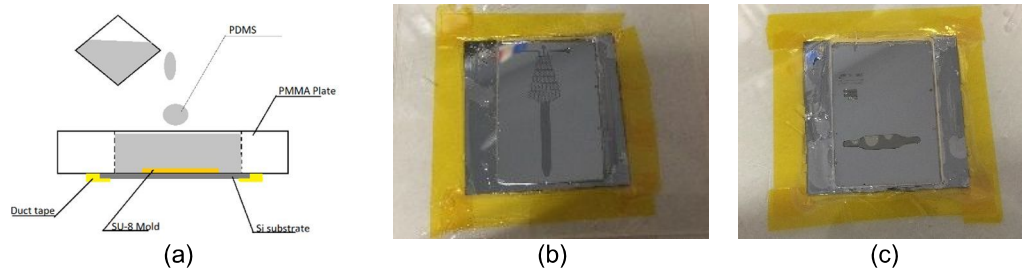


Figure 4.7 – (a) PDMS scaffold composed by SU-8 mold and pocketed PMMA plate. GG (b) and SS (c) SU-8 resist molds on Si substrate coupled with PMMA plate.

### 4.1.3 Replica molding and Assembly

The PDMS device components for SS and GG were prepared in a mold consisting in the SU-8 mold onto 2" Si plus one PMMA plate for mold thickness (Figure 4.7 (a)).

The replica molding was performed in the biolab facilities and consisted on the PDMS preparation, mold cleaning, scaffold assembly, scaffold filling, baking and peeling and mold cleaning.

Several SS and GG PDMS samples were produced to enable a comprehensive study of the microfluidic device. The PDMS devices were pierced with a metallic connector before assembly. The assembly could be reversible or irreversible. The reversible assembly is composed by mechanical sealing in the PMMA holder device micromachined while the irreversible assembly is composed by structures cleaning and bonding in the UVO cleaner.

The PMMA holder fabricated for the reversible mechanical sealing had to be adapted through the design process. The initial version was composed by two PMMA plates with a pocket on the bottom. This version has been discarded since the optical properties of the mechanism would be compromised in posterior microscope observation. The second version was composed by three PMMA plates, with metallic bolts to mechanically seal the mechanism (Figure 4.8 – (a)).

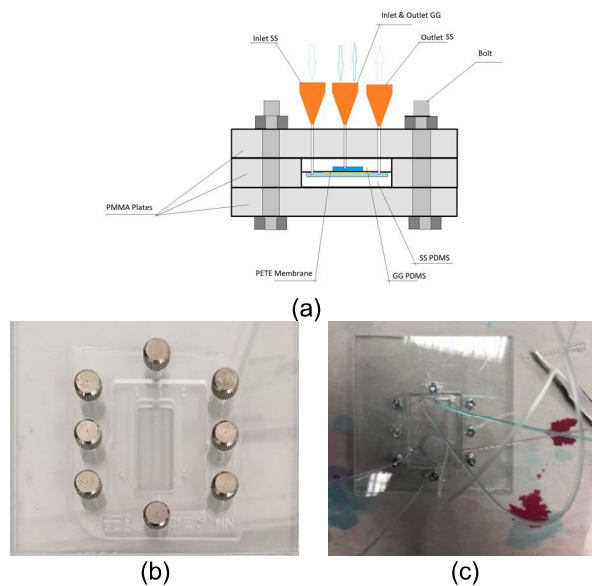


Figure 4.8 – (a) Schematic on the last version of PMMA holder with microfluidic device. Top view of the (b) initial version and (c) Last version of PMMA holder.

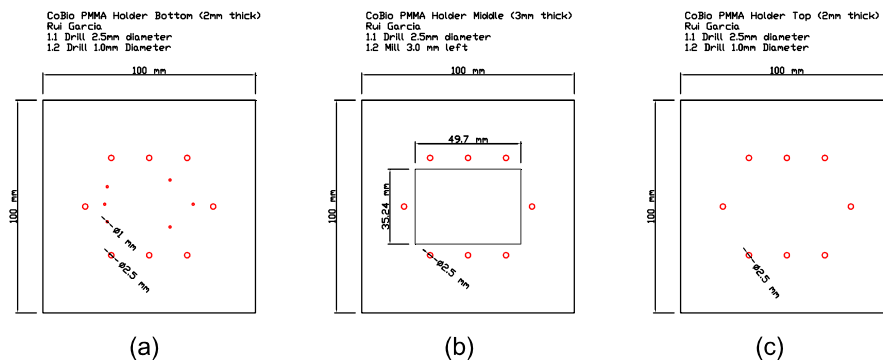


Figure 4.9 – Top view of the PMMA microfluidic device holder ((a) – bottom plate, (b) – Middle plate, (c) – Top plate). The plates have through holes for bolt tightening and only the top plate has access holes for microfluidic device inlets and outlets.

This holder couldn't stand more than 10 assemblies due to the wear of PMMA threads. The third and definitive version of the holder was built using through holes and metallic bolts and nuts (Figure 4.8 – (b) and (c)).

The microfluidic device exhibited some leakages between the PDMS structures and PETE membrane (Figure 4.10 – (a)). An additional compression was achieved with additional acrylic sheets to fill any gap between PDMS and PMMA holder reducing the leakage problem (Figure 4.10 – (b)). The assemblage of the PDMS device consisted in mounting the GG, the membrane and then the SS because this way the alignment was more efficient.

The irreversible assembly of individual PDMS systems enabled the effective flow rate on the device without leakages. The SS and GG individual PDMS structures bonding to PETE membrane and glass substrate are presented in Figure 4.11.

Plasma activation creates a weak bond between the PETE membrane and the PDMS microfluidic device (Aran et al. 2010) that isn't suitable for high pressure applications. In the microfluidic experiments performed the membrane zone didn't blister for low flow rates, however, for higher flow rates, used for microchannels clearance, the membrane zone blister. If this structure was to be used in higher pressure domain, a one-step chemical modification (amine-PDMS linker) at room temperature followed by corona treatment could be applied to increase the performance (Wu et al. 2014).

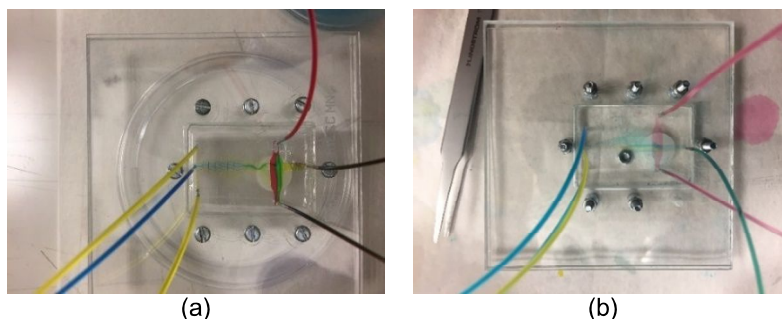


Figure 4.10 – (a) First version of microfluidic device with major leakage. (b) Third and last version of microfluidic device with minor leakage issues.

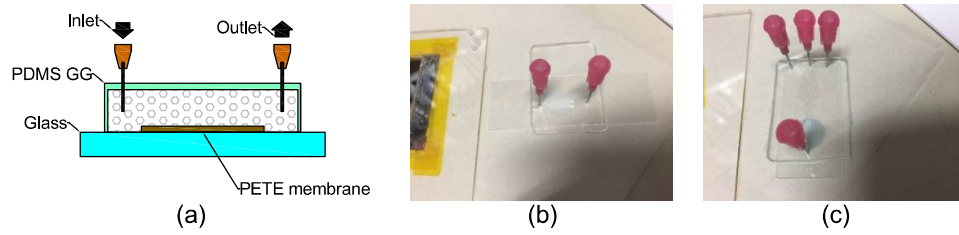


Figure 4.11 – (a) Side view schematic of the GG PDMS structures bonding to PETE membrane (b) SS PDMS structure bonded to PETE membrane and glass substrate. (c) GG PDMS structure bonded to PETE membrane and glass substrate at right.

## 4.2 CFD Simulation

### 4.2.1 Pressure Balance

PDMS has a Young modulus below  $1 \text{ MPa}$  (see Table 2.1) which make it suitable for low pressure microfluidic applications the pressure balance between the SS and GG in the membrane zone is critical to avoid additional membrane deflections or leakages. Pressure loss was computed over the hydraulic circuit using the Bernoulli principle assuming that the fluid (water) is incompressible, the flow is steady and that friction by viscous forces is negligible using the section dimensions and channel geometry of microfluidic device channel and polyethylene tubing the. The hydraulic circuit sections are depicted in Figure 4.1 and its geometric properties in Table 4.2.

The Bernoulli principle application is valid for most of the hydraulic circuit except for transition zones due to cross sectional variation and the mixer zone (GG - 2a) of GG. In this area the goal is to mix the inlets using viscous forces, however it has a null effect on the membrane pressure. To determine the pressure in the membrane only channel sections (SS - 3) and (SS - 2b) in SS and sections (GG - 3) and (GG - 2c) in GG must be considered.

Table 4.2 – Parameters of the microfluidic device.

Structure	Channel Section	Extension [mm]	Shape	Diameter [mm]	Width [mm]	Height [mm]	Area [mm <sup>2</sup> ]	Perimeter [mm]
Gradient Generator	GG - 1	150	Cylindrical	0,86	-	-	0,58	2,70
	GG - 2a	19,3	Rectangular	-	0,2	0,1	0,02	0,60
	GG - 2b	11,5	Rectangular	-	3	0,1	0,30	6,20
	GG - 2c	10,8	Rectangular	-	3	0,1	0,30	6,20
	GG - 3	150	Cylindrical	0,86	-	-	0,58	2,70
Shear Stress	SS - 1	150	Cylindrical	0,86	-	-	0,58	2,70
	SS - 2a	12,5	Rectangular	-	4,5	0,1	0,45	9,20
	SS - 2b	12,5	Rectangular	-	4,5	0,1	0,45	9,20
	SS - 3	150	Cylindrical	0,86	-	-	0,58	2,70

The dimension of the channel extension was considered the projection over the flow direction. Due to presence of microchannel bifurcation levels in the mixer section of GG (GG - 2a) of bifurcation the flow was considered divided by several small microchannels in its extension with dimensions  $0.2 \times 0.1 \text{ mm}^2$ . The values of pressure drop for each region of the flow is given in Table 4.3. The

extension of the polyethylene tubing was also considered since it represents about 1/3 of the pressure drop ( 2.7 ) on the SS and less than 4% of on the GG. The discrepancy is due to the section constriction in the mixer area of the GG that is made to enable a better mixing resulting in a larger pressure drop as detailed in Table 4.3 that are performed for a SS mean fluid velocity  $U = 20.0 \text{ mm.s}^{-1}$  that yields a flow rate in section SS-2a and SS-2b of  $540 \mu\text{L.min}^{-1}$ .

*Table 4.3 – Pressure drop computation and average wall shear stress for enables a pressure balance*

Structure	Channel Section	$D_h$ [mm]	$U$ [mm.s <sup>-1</sup> ]	$Re$ [–]	$f$ [–]	$\Delta p$ [Pa]	$\tau$ [Pa]
<b>Gradient Generator</b>	GG - 1	0,86	4,2	2,40	6,7	33	0,09
	GG - 2a	0,13	56,8	4,98	3,2	2366	8,17
	GG - 2b	0,19	24,6	3,13	5,1	290	2,44
	GG - 2c	0,19	24,6	3,13	5,1	272	2,44
	GG - 3	0,86	12,7	7,19	2,2	99	0,28
<b>Shear Stress</b>	SS – 1	0,86	15,5	8,77	1,8	121	0,35
	SS - 2a	0,20	20,0	2,57	6,2	251	1,96
	SS - 2b	0,20	20,0	2,57	6,2	251	1,96
	SS – 3	0,86	15,5	8,77	1,8	121	0,35

From Table 4.3 it is possible to conclude that for all microchannels the flow is laminar. The wall shear stress was computed according to ( 2.9 ).

To balance pressure in the PETE membrane, the flow rate of SS and GG must be set to the relation ( 4.1 ). The pressure loss in polyethylene and mixer areas isn't negligible. The calculated averaged wall shear stress for the SS surface in the PETE membrane area (SS - 2a and SS – 2b) found to be  $1.96 \text{ Pa}$ .

$$Q_{GG} = 0.82 * Q_{SS} \quad (4.1)$$

## 4.2.2 Characteristic Diffusion Time

An estimate of the time required to simulate the VEGF diffusion at the membrane pore provides an order of magnitude of the process and limits the time of CFD simulation ( $t_{sim}$ ) used to assess the effective concentration diffusion. The transport will be convective-diffusive and not separately convective or diffusive. However, to estimate the concentration establishment time some simplification must be made.

Two hypotheses were considered, a mixed transport ruled initially by convection in the channel ( $x_1$ ) and afterwards by diffusion ( $x_2$ ) and a pure diffusion transport ruled solely by diffusion over the distance ( $x_1 + x_2$ ). Note that since the pore is closed at the bottom the convective transport in this part is excluded. The schematic of travelling distance is depicted in Figure 4.12 (a).

Considering the convective transport, the particle velocity considered was 1/5 of the average velocity derived from the paraboloid velocity profile in the effective diffusive time computation and the particle travelling time ( $t_{1c}$ ) computation is straight forwarded. The diffusive time constant is estimated using the relation  $\tau = \frac{x_c^2}{4 * D}$ . The characteristic length ( $x_c$ ) is the membrane thickness or inlet-pore distance and the



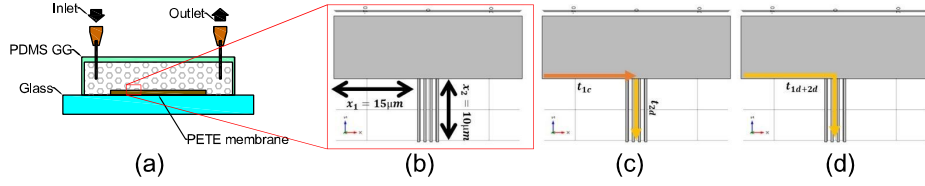


Figure 4.12 – (a) Side view of GG and membrane detail in red. (b) Travelling distances scheme of  $x_1$  and  $x_2$  in GG schematic. (c) Travelling times scheme of  $t_{1c}$  and  $t_{2d}$  for a mixed transport ruled initially by convection and afterwards by diffusion in GG. (d) Travelling time scheme of  $t_{1d+2d}$  for a mixed transport ruled by diffusion in GG.

diffusion coefficients,  $D$ , of water which is a small molecule and a large protein like VEGF. The convective time is at least five times the characteristic diffusive time in the pore ( 4.2 ), resulting in 0.13 [s] for a small molecule and 2.50 [s] for a large protein.

$$t_i = 5 \times \tau_i \quad (4.2)$$

The simulation time was computed as the minimum between the sum of effectives convective ( $t_{1c}$ ), diffusive ( $t_{2d}$ ), and effective diffusive path times ( $t_{1d+2d}$ ). The schematic of travelling times is depicted in Figure 4.12 (c) and (d).

Table 4.4 – CFD simulation time estimate.

Scenario	Average Velocity $U$ [mm/s]	Diffusion Coefficient $D$ [m <sup>2</sup> /s]	Inlet Pore Distance $x_1$ [μm]	Convective Time $t_{1c}$ [s]	Membrane thickness $x_2$ [μm]	Diffusive Time $t_{2d}$ [s]	Diffusive Time $t_{1d+2d}$ [s]	Simulation Time $t_{sim}$ [s]
1 Water	0,1	1,00E-09	15	0,75	10	0,13	0,78	0,78
2 VEGF	0,1	5,00E-11	15	0,75	10	2,50	15,63	3,25
3 Water	20	1,00E-09	15	0,00375	10	0,13	0,78	0,13
4 VEGF	20	5,00E-11	15	0,00375	10	2,50	15,63	2,50

From Table 4.4 it is possible to conclude that the effective diffusive transport time ( $t_{sim}$ ) is lower than convective time in scenarios 2, 3 and 4. However, in scenario 1 the influence of the diffusive transport is dominant due to the lower velocity and higher diffusion coefficient. The minimum simulation time of the CFD analysis must be at least  $t_{sim}$ .

### 4.2.3 Gradient Generator – Pore Diffusion

In the GG the area of interest was reduced to enable a simplified but, yet representative model of the actual VEGF gradient sensed by EC in the GG membrane in red of Figure 4.13. This model aims to estimate the diffusion time of a given solute species in a pure volume solution to check if the membrane pore replicates the concentration profile of the cross section intended to the EC.

As mentioned previously, incompressible fluid flow and convective/diffusive transport of passively advected scalar field are governed by the ( 2.16 ) continuity, ( 2.17 ) Navier-Stokes and ( 2.27 ) species transport equations. In Table 3.1, are the dimensions used for GG foot print area ( $3000 \times 100 \mu\text{m}^2$ ) and for SS foot print area ( $4500 \times 100 \mu\text{m}^2$ ). The minimum and maximum velocities ( $U$ ) considered were of

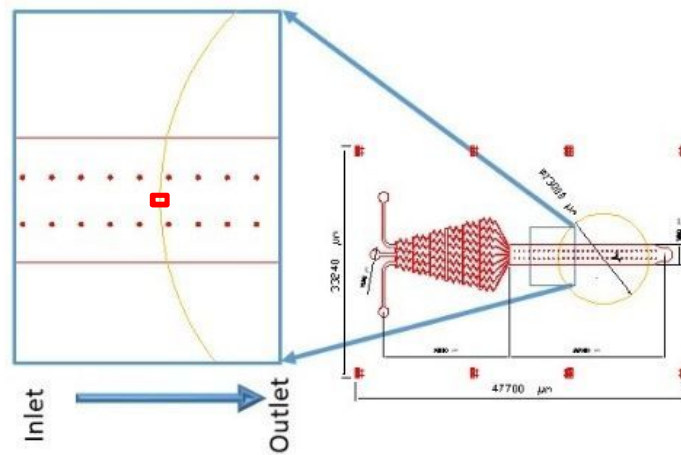


Figure 4.13 - Top View of Gradient Generator (Left – Zoom In | Right – Global).

$0.1 \text{ mm.s}^{-1}$  and  $20.0 \text{ mm.s}^{-1}$  that results in a low Reynolds number ( 4.3 ) for any of the cases, well inside the region of laminar flow , and for the lowest velocities a creep flow as observed in Table 4.5.

$$Re = \frac{D_h U_{avg} \rho}{\eta} \quad (4.3)$$

Table 4.5 – Reynolds Number computation for limit cases.

Device Component	Maximum Width [ $\mu\text{m}$ ]	Maximum Height [ $\mu\text{m}$ ]	Hydraulic Diameter $D_h$ [ $\mu\text{m}$ ]	Average Velocity $U_{avg}$ [ $\text{mm.s}^{-1}$ ]	Flow Rate $Q$ [ $\mu\text{L.min}^{-1}$ ]	Number $Re$ [–]
GG	3000	100	194	0,1	2,7	0,019
GG	3000	100	194	20	540,0	3,859

In this sense, it is possible to estimate a numerical solution of the full momentum balance and continuity equations for incompressible flow with a reasonable number of elements. The equations that are needed, as referred in sections 2.4.2.1 and 2.4.2.2, are presented, and simplified for the case study as:

$$\nabla v = 0$$

**Erro! A origem da referência não foi encontrada.**

$$\rho(v\nabla)v = \nabla[-pI + \eta\nabla v] \quad (4.4)$$

where  $I$  corresponds the identity matrix. Separation in this structure involves species in relatively low concentrations compared to that of the solvent, water. Assuming a binary mixture of a solute A in solvent B, concentrations up to 10 mol% of A can be considered diluted. It is admissible to use Fick's law to describe the diffusive transport inside the channel, assuming that the solute molecules interact only with water molecules and the flow is in steady state.

To simulate the mixing of different species equation ( 4.4 ) was solved for  $D = \{100, 5\} * 10^{-11} \text{ m}^2.\text{s}^{-1}$ , considering respectively the values of diffusion coefficients for small molecules like water



(Holz et al. 2000) and large proteins like VEGF using Einstein equation ( 2.10 ) that results in  $D = 6.12 \times 10^{-11} \text{ m}^2 \cdot \text{s}^{-1}$ . It is assumed that a change in solute concentration does not influence the fluid density and viscosity. This implies that it is possible to solve the Navier-Stokes equations, and then solve the mass balance equation.

The computation of the Peclet number ( 2.33 ) enables the estimation of the mass transport regime. From Table 4.6 analysis and the considerations made in section 2.4.2.5 it can be observed that for  $Pe < 1000$  the influence of the diffusive component increases in the convection-diffusion flow dispersion.

Table 4.6 – Dimensional analysis of the flow.

Solute	$U$ [mm. s <sup>-1</sup> ]	$D$ [m <sup>2</sup> . s <sup>-1</sup> ]	$Re$ [–]	$Sc$ [–]	$Pe$ [–]
$H_2O$	0,1	$100 \times 10^{-11}$	0,019	1000	19,4
$H_2O$	20	$100 \times 10^{-11}$	3,859	1000	3870
$VEGF$	0,1	$5 \times 10^{-11}$	0,019	20100	387
$VEGF$	20	$5 \times 10^{-11}$	3,859	20100	77400

The Figure 4.14 refers to relevant boundary conditions and dimensions of GG CFD model in the vicinity of the bottom wall in contact with the PETE membrane pores represented in this model by a  $4 \times 4$  array of salient cylinders.

At the inlets, the velocity field was assumed perpendicular to the boundary in the inward direction, following a paraboloid profile according to (White 1991) to match the mean velocity to those presented in Table 3.3. Similar conditions were considered in the side walls and upper wall to match the velocity profile ( 4.5 ). At the outlets, pressure condition was imposed ( 4.6 ) and due to small volume analysis, the vanishing viscous stress was discarded ( 4.7 ).

$$v = -v_0 \cdot n \quad (4.5)$$

$$p = p_0 \quad (4.6)$$

$$n \cdot \eta (\nabla v) = 0 \quad (4.7)$$

At the bottom wall and pores, no slip condition states that the velocity is zero at the wall, ( 4.8 ).

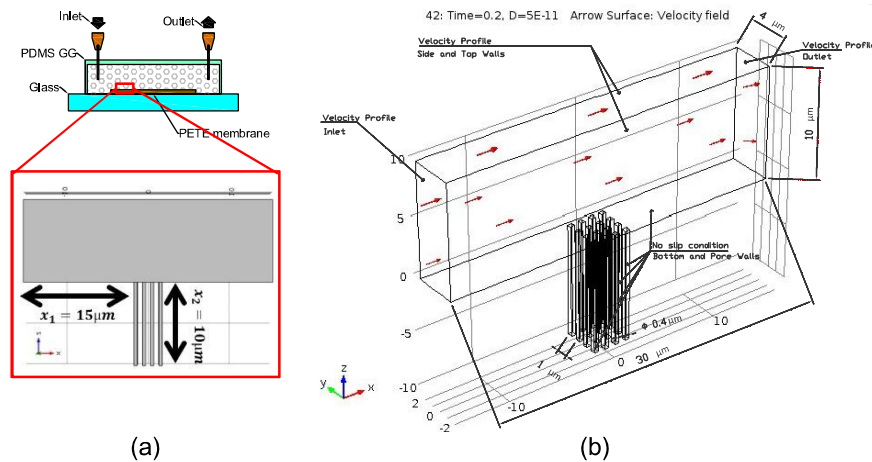


Figure 4.14 – (a) Side View schematic and zoom in of GG with PDMS system, PETE membrane and glass surface where the channel saliences represent the membrane pores (b) 3D View of GG CFD model and boundary conditions.

Considering the balance of mass, the assumption that solute molecules only interact with water molecules implies that it is sufficient to consider a single species A of concentration  $c$ . At the inlet the concentration boundary condition is  $c = c_0$  and in the volume of analysis for the initial time the concentration  $c_{t=0} = 0$  to compute the diffusing time of the species over the volume.

$$(u, v, w)_{wall} = (0, 0, 0) \quad (4.8)$$

$$c = c_0 \text{ at inlet A} \quad (4.9)$$

$$c = 0 \text{ volume of analysis for } t = 0 \quad (4.10)$$

Established the boundary conditions and given the system of partial differential equations, the FEM was considered to solve this system. In this sense, the solution domain is spatially discretized by constructing a series of interlocking nodes and elements, resulting in a finite number of elements that approximate the spatial geometry whose shape can be linear, triangular and parabolic. Using these techniques in variational calculus to satisfies the specified conditions for the construction of a partial differential equation. Then, an approximation for the field is introduced by matrix multiplying linear basis functions by unknown nodal values.

In a practical sense, the mesh size was fine tuned to enable the creation of regular elements along the volume with exception of points of interest where the discretization was increased. The mesh size roughly corresponds to the software “Fine” mesh and a control of mesh quality was performed using the software functionality to increase this parameter over the points of interest.

The determination of the overall diffusive time is crucial to assess what time is required to ensure the concentration of interest in EC cells above the membrane. The CFD simulation time estimate ( $t_{sim}$ ) derived in section 4.2.2 set an upper bound of the CFD analysis time required to observe the diffusion made in this section. A time margin was given so the diffusion process could be complete.

Since the transport will be convective-diffusive and not separately convective in the streamwise direction and diffusive in the spanwise direction the estimate will be an upper bound. The establishment time in the GG bottom wall ( $t_1$ ) was considered the time in which the concentration at GG bottom wall

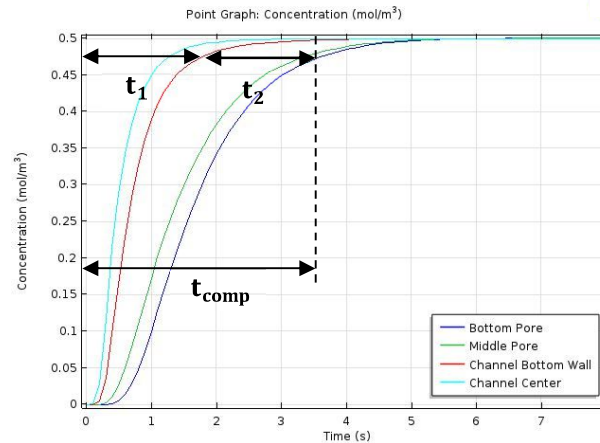


Figure 4.15 – Computation of the overall diffusion time at the membrane pore. The “particle arrival times” are the times required to guaranty 95% of concentration in the paths inlet-bottom channel  $t_1$ , pore top- pore bottom  $t_2$  and inlet-pore bottom  $t_{comp}$ .

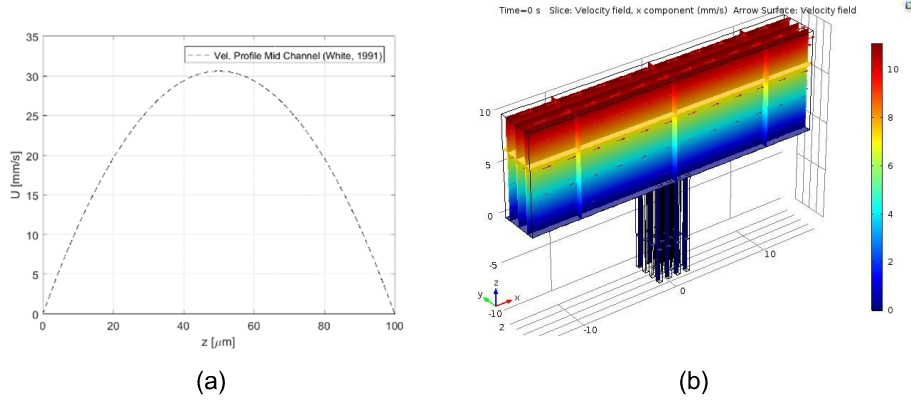


Figure 4.16 – Vertical velocity profile at GG mid channel using numerical approximation (White 1991) at left. Velocity field on the model region of interest at middle. Vertical velocity profile at GG at the model inlet, mid-section and outlet comparison with imposed conditions at right. Note that the previous results considered a profile mean velocity of  $20 \text{ mm} \cdot \text{s}^{-1}$ .

reached 95% of the concentration generated at the inlet (Figure 4.15). The establishment time in the membrane pore ( $t_2$ ) was considered the difference between the time in which the concentration between the bottom wall and the bottom of the membrane pore reached 95% of the concentration generated at the inlet (Figure 4.15). The simulation time ( $t_{sim}$ ) estimated in section 4.2.2 is further compared to the computational time ( $t_{com} = t_1 + t_2$ ).

The velocity profile imposed at the inlet considered a numerical approximation (White 1991) and is presented in Figure 4.16 (a). The velocity field determination was decoupled of the mass transport to enable a quicker simulation (Witarsa et al. 2013).

It is possible to observe the velocity field constancy over the  $x$  (longitudinal) direction and that the membrane pores have negligible effect on velocity profile (Figure 4.16 (b)).

Figure 4.17 (a) shows that the outlet boundary conditions are distorting the surface pressure near the outlet. This distortion becomes evident in the velocity profile that is maintained over the longitudinal direction with exception of the outlet which exhibits a small variation at the  $\frac{1}{4}$  and  $\frac{3}{4}$  height of the model (Figure 4.17 (b)).

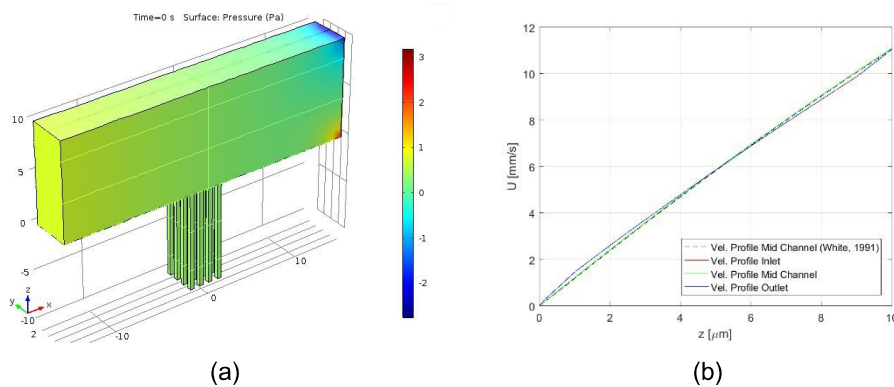


Figure 4.17 – Pressure surface on the model region of interest at left. Vertical velocity profile at GG at the model inlet, mid-section and outlet comparison with imposed conditions at right. Note that the previous results considered a profile mean velocity of  $20 \text{ mm} \cdot \text{s}^{-1}$ .

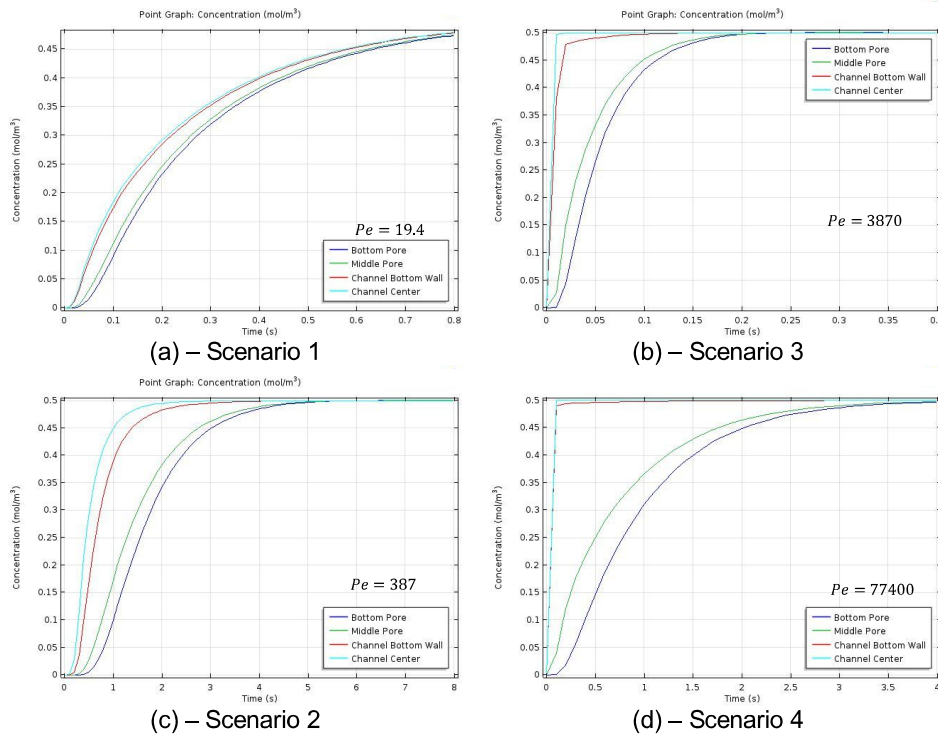


Figure 4.18 – Concentration profiles at the pore bottom, pore middle, channel bottom wall and channel center. The computation was made considering the channel bottom and pore bottom. (a) Scenario 1:  $U = 0.1 \text{ mm} \cdot \text{s}^{-1}$  &  $D = 1 \times 10^{-9} \text{ m}^2 \cdot \text{s}^{-1}$ . (c) Scenario 2:  $U = 0.1 \text{ mm} \cdot \text{s}^{-1}$  &  $D = 5 \times 10^{-11} \text{ m}^2 \cdot \text{s}^{-1}$ . (b) Scenario 3:  $U = 20 \text{ mm} \cdot \text{s}^{-1}$  &  $D = 1 \times 10^{-9} \text{ m}^2 \cdot \text{s}^{-1}$ . (d) Scenario 4:  $U = 20 \text{ mm} \cdot \text{s}^{-1}$  &  $D = 5 \times 10^{-11} \text{ m}^2 \cdot \text{s}^{-1}$ .

The computational time was computed for four scenarios, which consider the combination between two mean velocities  $U = \{0.1 ; 20.0\} \text{ mm} \cdot \text{s}^{-1}$  and two molecules of different sizes  $D = \{1 \times 10^{-9} ; 5 \times 10^{-11}\} \text{ m}^2 \cdot \text{s}^{-1}$  (Table 4.7). The CFD simulation time estimate ( $t_{sim}$ ) relative error ( $E_r$ ) is computed considering as the value computed in this section for the diffusive time ( $t_{com}$ ).

Table 4.7 – Computation of effective diffusive time in membrane pores bottom.

Scenario	$U$ [mm/s]	$D$ [m <sup>2</sup> /s] $\times 10^{-11}$	$t_1$ [s]	$t_2$ [s]	$t_{comp}$ [s]	$t_{sim}$ [s]	$E_{r,t_{sim}}$ [%]
1 Water	0,1	100	0,760	0,050	0,810	0,781	3,55%
2 VEGF	0,1	5	1,762	1,838	3,600	3,250	9,72%
3 Water	20	100	0,010	0,120	0,130	0,129	0,96%
4 VEGF	20	5	0,065	2,435	2,500	2,504	0,15%

Table 4.7 analysis show that the estimates made for the diffusive time ( $t_{sim}$ ) from inlet to bottom pore are close to those computed in the FEM model with a relative error lower than 10%. This estimate becomes less reliable when the transport is ruled both by diffusion and convection alike as it can be

observed in scenarios 1 and 2 for lower velocities. Note that the diffusive time estimates ( $t_2$ ) are accurate for scenarios 3 and 4 for higher velocities. This finding becomes clearer if the concentration profiles of the bottom wall and pore bottom are observed together, finding that in scenarios 1 and 2 the diffusion phenomena to the wall bottom has the same pace as the diffusion as the pore bottom (Figure 4.18).

#### 4.2.4 Gradient Generator - Mixer Efficiency

To study the mass transport mixer efficiency extensively a 3D numerical model should be used. The molecule of interest is a large protein VEGF with a low diffusion coefficient ( $5 \times 10^{-11} \text{m}^2.\text{s}^{-1}$ ) and the molecule that were tested lately are food colour dyes that have lower dimension and diffusion coefficients closer to the lower bound considered ( $1 \times 10^{-9} \text{m}^2.\text{s}^{-1}$ ). Studying the mass transport in this range of diffusion coefficient, therefore provides a comprehensive understanding of the phenomena.

Computing such a 3D model with accuracy would yield an excessive computational time. This way, the model complexity was reduced from 3D to 2D that require some considerations. The mass transport in an extensive model such as this should be predominantly convective in the streamwise direction and diffusive in spanwise direction. For low flow rates and high diffusion coefficients this assumption might not hold and motivated the study. With the model reduction the mass transport is assumed to change mainly in the streamwise direction and to change little in the model perpendicular spanwise direction. This assumption doesn't hold since the channel height is 30 times smaller than the channel width and the velocity profile is paraboloid specially in the transition zones. However, for regular zones distanced at least the development length the model can be considered a good approximation.

The Figure 4.19 refers to relevant boundary conditions and dimensions of GG CFD model.

At the inlets, velocity conditions were specified so the average inflow velocity match the desired flow rate at the longer channel extension. At the outlets, pressure condition was applied ( 4.6 ) and due to small volume analysis, the vanishing viscous stress was discarded ( 4.7 ).

Condition ( 4.6 ) states that the pressure is  $p_0$  at the outlet. It is a numerically stable boundary condition that admits total control of the pressure level at the whole boundary.

At the bottom wall and pores, no slip condition states that the velocity is zero, ( 4.11 ). Considering the balance of mass, the assumption that solute molecules interact, only with water molecules implies that it is sufficient to consider a single species A of concentration  $c$ . At the three inlets, two combinations of concentrations were used for the Concentration boundary condition ( 4.11 ) and for volume initial concentration ( 4.13 ).

$$(u, v) = (0, 0) \quad (4.11)$$

$$c_{I1} = \{1: 1; 1: 2\} \text{ at inlet 1} \quad (4.12)$$

$$c_{I2} = \{1: 10; 1: 20\} \text{ at inlet 2}$$

$$c_{I3} = \{1: 100; 1: 200\} \text{ at inlet 3}$$

$$c = 0 \text{ volume of analysis for } t = 0 \quad (4.13)$$

The combinations used matched those used later in the experimental setup. The finite elements shape used was triangular to approximate the intricate spatial geometry. The mesh size corresponds to the software “Finer” mesh with  $10\ \mu\text{m}$  over the points of interest and  $50\ \mu\text{m}$  in the regular ones.

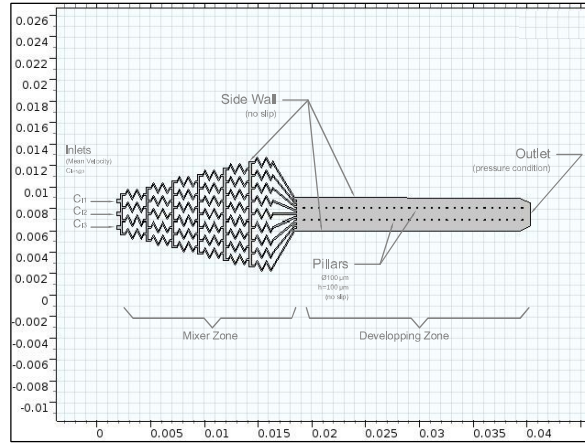


Figure 4.19 - 2D View of Gradient Generator CFD model and boundary conditions.

Concluded the process depicted in section 4.2.3, the system simulation was conducted for the two inlets concentration combinations, four average flow velocities  $\{0.1 ; 1.5 ; 10.5 ; 20.0\} \text{ mm.s}^{-1}$  and two diffusion coefficients  $\{1 \times 10^{-9} ; 5 \times 10^{-11}\} \text{ m}^2.\text{s}^{-1}$ .

The CFD analysis was made for eight scenarios that were tested experimentally. The results presented in this section refer to a situation closer to serviceability conditions with average flow velocity of  $20.0 \text{ mm.s}^{-1}$  and diffusion coefficient of  $5 \times 10^{-11} \text{ m}^2.\text{s}^{-1}$ . The velocity field over the GG system is depicted in Figure 4.20.

Figure 4.20 shows that the velocity profile varies according to section constriction. In Figure 4.20 – (c) the velocity in the first ramifications is close to  $240 \text{ mm.s}^{-1}$  whilst in the channel developing zone Figure 4.20– (b) and (d) the velocities are below  $40 \text{ mm.s}^{-1}$ . The anti-fouling pillars cause a midchannel constriction that causes the flow to subdivide in three sections that remain approximately constant over the developing zone decreasing the homogeneity of the flow and resemblance to the expected paraboloid profile.

The pressure over the GG system is depicted in Figure 4.21 that enables a validation of some findings made in section 4.2.1.

The pressure drop is larger over the mixer zone of  $\Delta p_{GG-2a} = 2800 \text{ Pa}$  and in the developing zone of  $\Delta p_{GG-2b+2c} = 200 \text{ Pa}$  (Figure 4.21). The pressure drop computed in section 4.2.1 for the mixer zone is lower  $\Delta p_{GG-2a} = 2366 \text{ Pa}$  and is higher for the developing zone  $\Delta p_{GG-2b+2c} = 562 \text{ Pa}$ . This discrepancy can be attributed to the simplifications made in the two models.

In the Bernoulli approach the mixer zone was deeply simplified and the anti-fouling pillars were excluded. Both extension and channel geometry could be further discriminated in the mixer zone and in the developing zone an additional constraint could be imposed dividing the flow in three subsections and imposing mass and energy balance in flow and pressure drop in these subsections.



In the CFD approach, the reduction of dimension excludes the influence of top and bottom walls that isn't negligible. Despite the major simplifications, both models provide valuable insights that can be used consecutively in the design process without contradiction.

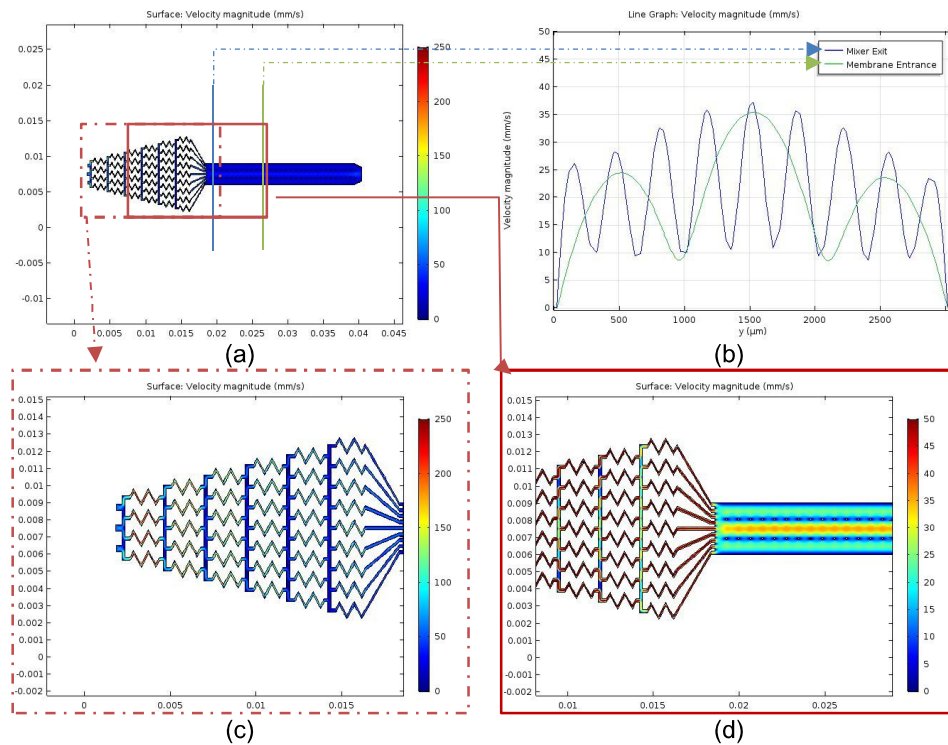


Figure 4.20 – (a) Top view of velocity profile of GG. (b) Spanwise velocity profile at GG mixer exit and membrane entrance. (c) Top view of velocity profile of GG at mixer exit. (d) Top view of velocity profile of GG at membrane entrance. Note that the previous results considered a profile mean velocity of  $20 \text{ mm} \cdot \text{s}^{-1}$ .

The surface concentration and concentration profile, over the mixer exit and PETE membrane entrance are presented in in Figure 4.22 with the extreme combinations of flow rate mean velocity and diffusion coefficient to highlight the importance of a fine tuning these variables.

Figure 4.22 (a) and (c) show that at the mixer exit area the diffusion coefficient apparently has little influence in the higher and lower concentrations, however in the developing zone, near the outlet, these concentrations become more diffuse for (c) and apparently constant for (a). Figure 4.22 (b) and (d) highlight the previous finding for the membrane entrance where the lower concentration is sustained in

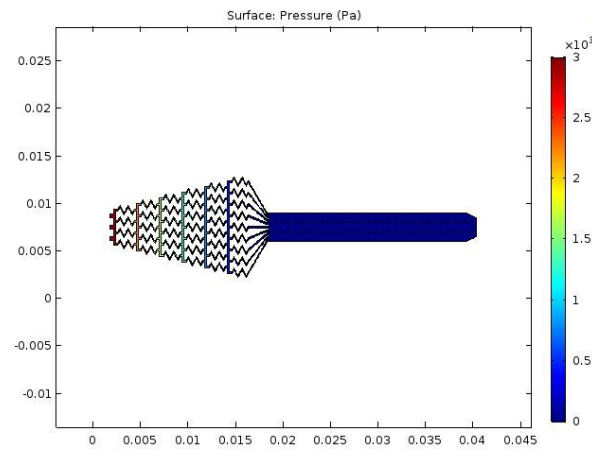


Figure 4.21 – Top view of pressure profile of GG. Note that the previous results considered a profile mean velocity of  $20 \text{ mm.s}^{-1}$ .

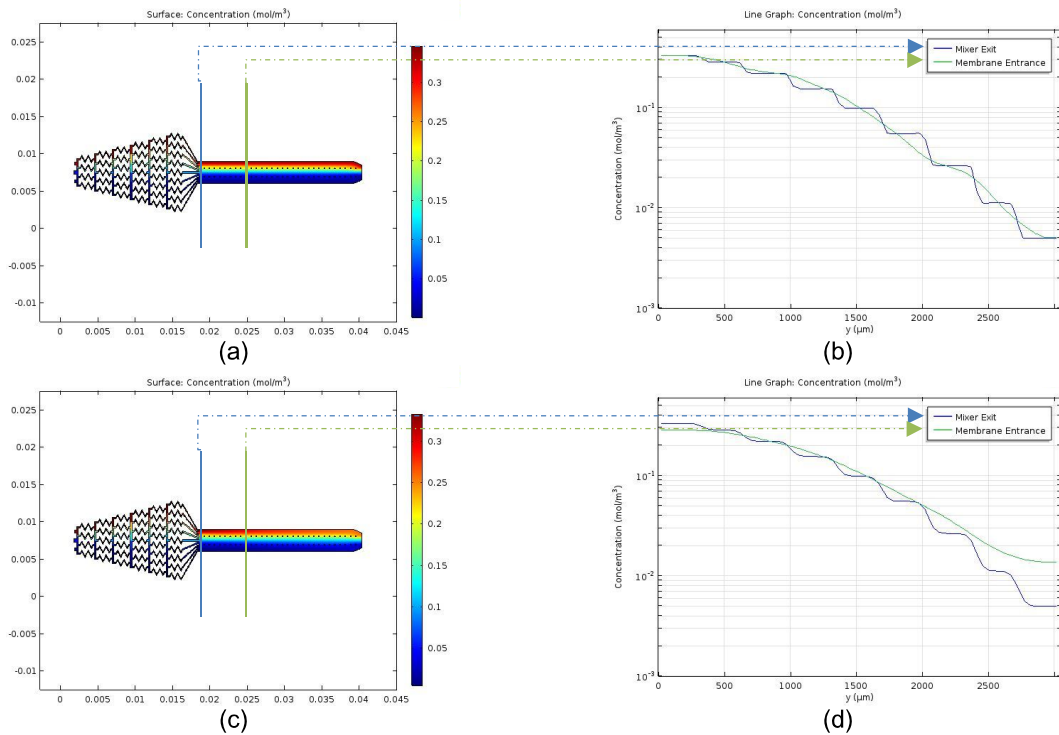


Figure 4.22 – The following results are obtained for inlets concentration of  $c_{I1} = 1:2$ ,  $c_{I2} = 1:20$  and  $c_{I3} = 1:200$ . (a) Top view of concentration profile of GG. (b) Spanwise concentration profile at GG mixer exit and membrane entrance. (a) and (b) considered a profile mean velocity of  $20 \text{ mm.s}^{-1}$  and for a VEGF diffusion coefficient  $5 \times 10^{-11} \text{ m}^2.\text{s}^{-1}$ . (c) Top view of concentration profile of GG. (d) Spanwise concentration profile at GG mixer exit and membrane entrance. (c) and (d) considered a profile mean velocity of  $0,1 \text{ mm.s}^{-1}$  and for a small molecule diffusion coefficient  $1 \times 10^{-9} \text{ m}^2.\text{s}^{-1}$ .

$0.005 \text{ mol.m}^{-3}$  in (b) and increases for  $0.012 \text{ mol.m}^{-3}$  for (d). The influence of convective transport is more prominent in the latter given the lower velocity and higher diffusibility. A closer look in the concentration profile development in the mixer zone exit results in smoother steps for (d) when compared with (b). These findings make clear that establishing the velocity and molecule of diffusion serviceability range should be defined for the microfluidic system end-user.



## 4.2.5 Shear Stress

This simulation aims to estimate the variation of shear stress along the EC array.

In the shear stress generator, the area used in these simulations is only a portion of the entire system for computational simplification, however it is a representative model of the actual shear stress experienced by EC above the PETE membrane in red at Figure 4.23.

The minimum and maximum velocities ( $U$ ) considered were of  $0.1 \text{ mm/s}$  and  $20.0 \text{ mm.s}^{-1}$  that results in Reynolds number below  $Re < 10$  for any of the cases, that sustain the hypothesis of laminar flow observed in Table 4.8. For the lowest velocity  $U_{avg} = 0.1 \text{ mm.s}^{-1}$  creeping flow hypothesis is valid.

At the inlets, velocity conditions were specified by the normal inflow velocity, i.e. the velocity in the inward direction normal to the boundary, in a paraboloid profile to match the mean velocity to those and

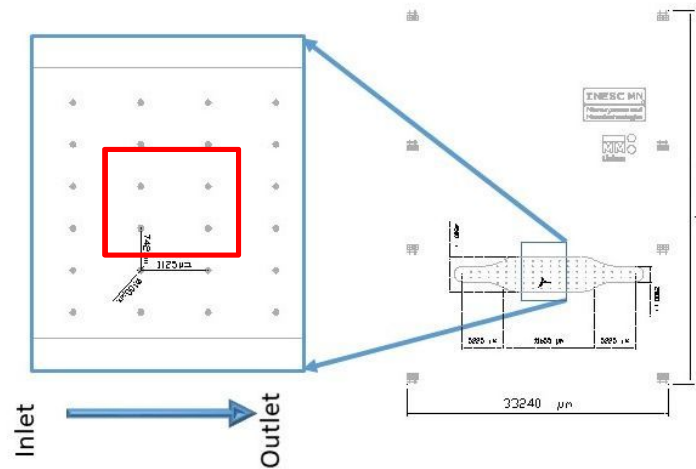


Figure 4.23 - Top View of Shear Stress Generator (Left – Zoom In | Right – Global).

due to small volume analysis, the vanishing viscous stress was discarded ( 4.7 ). This boundary condition states that the pressure is  $p_0$ . It is a numerically stable boundary condition that admits total control of the pressure level at the whole boundary. At the bottom and top walls, no slip condition states that the velocity is zero,( 4.8 ). The boundary conditions of SS CFD model can be observed in Figure 4.24.

Table 4.8 – Reynolds Number computation for limit cases.

Device Component	Width [μm]	Height [μm]	Hydraulic Diameter $D_h$ [μm]	Average Velocity $U_{avg}$ [mm/s]	Reynolds [-]
SS	4500	100	196	0,1	0,020
SS	4500	100	196	20	3,901

EC semi-ellipsoidal shape, with  $15 \mu\text{m}$  high and  $50 \mu\text{m}$  of diameter, exhibits a non-uniform wall shear stress with a higher shear stress on top and lower at bottom that motivated its parametrization. This way

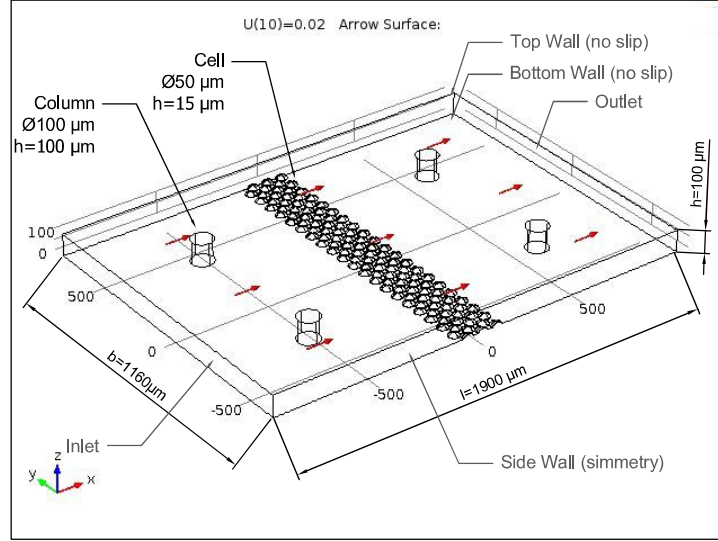


Figure 4.24 - 3D View of Shear Stress Generator CFD model and boundary conditions.

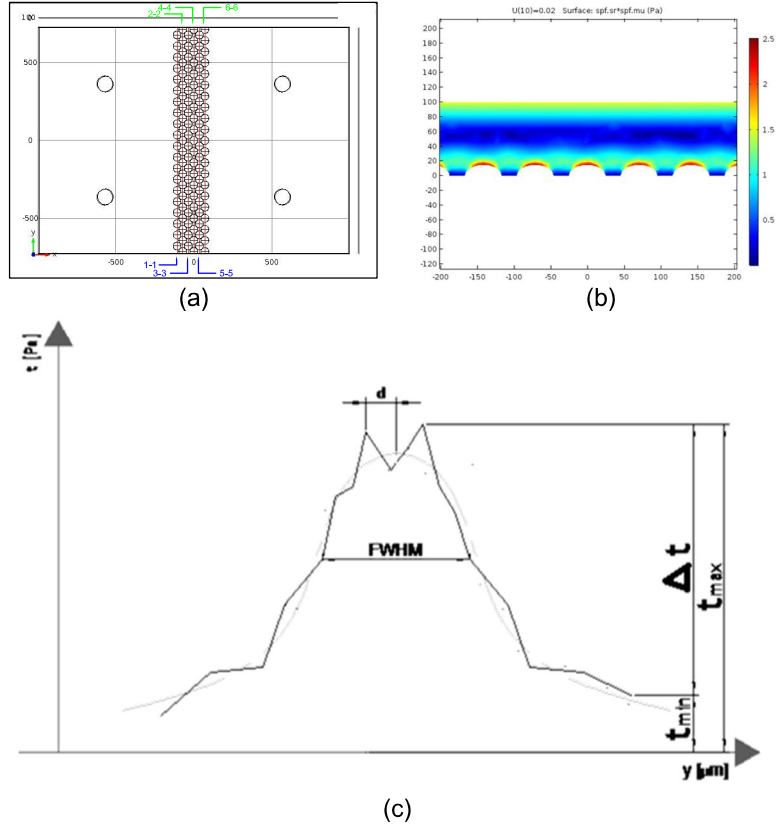


Figure 4.25 – (a) Top view of SS with 1D cuts at 15  $\mu\text{m}$  height. (b) Front view cut of shear stress. (c) Parametrization of shear stress in a cell.

using the six EC alignments, the shear stress was evaluated at a constant height that corresponded to the cell height. The shear stress in these horizontal alignments followed a sigmoidal shape with peaks coincident with cell zenith. The variables accessed were the maximum shear stress  $\tau_{max}$ , minimum shear stress  $\tau_{min}$ , full width at half maximum  $FWHM$ , the lateral deviation to the cell zenith  $\delta$  and the shear stress prominence  $\Delta\tau = \tau_{max} - \tau_{min}$  that can be observed in Figure 4.25 (c).

Cell disposition and cell spacing influence both magnitude and shape of the shear stress distribution in cells. To enable the comprehension of the cell distribution a parametric study was made considering cell to cell distance and cell orientation related to flow direction as depicted in Figure 4.26.

The seven models created that enabled this study are depicted in Figure 4.27 and tackle the influence

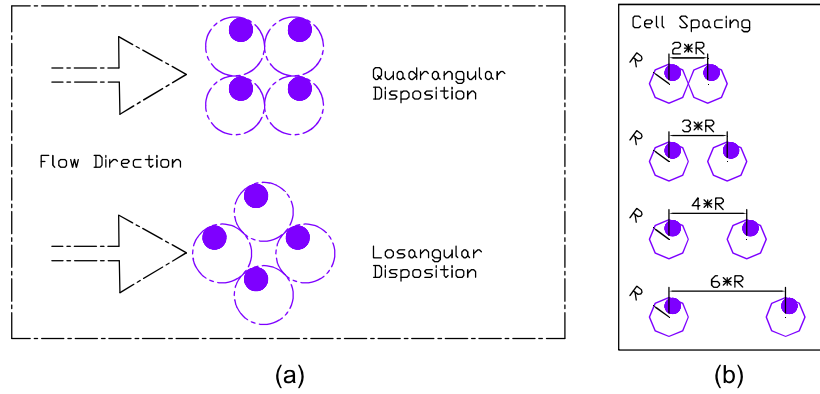


Figure 4.26 - Cell disposition (a) and Cell spacing (b) schemes.

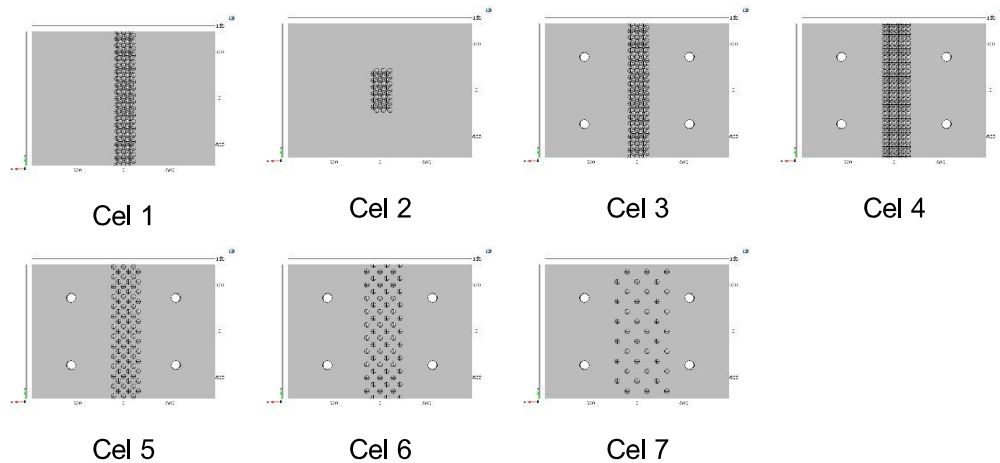


Figure 4.27 - Top view of Shear Stress Generator in 7 configurations of cell disposition and cell spacing.

of packing of cells in the channel width, influence of positioning of anti-fouling pillars and cell spacing (Table 4.9).

The effective wall shear stress experienced by EC must be within physiological parameters which was the second requirement for the system work mode.

The wall shear stress evaluation was subdivided in two sections. The first section consisted in the validation of the mesh size that enabled a reasonable tradeoff between accuracy and computational time. The second section studied the influence of cell disposition with the mesh size previously defined. These analyses considered a parametrization on the wall shear stress features enabling an effective characterization.

Table 4.9 – Cell configurations in shear stress CFD model.

Configuration	Spacing between cells	Disposition of cells	Packing of cells in channel width	Presence of pillars
---------------	--------------------------	-------------------------	--------------------------------------	------------------------

<b>Cel 1</b>	2 <i>R</i>	Diamond	Full	No
<b>Cel 2</b>	2 <i>R</i>	Diamond	Partial	No
<b>Cel 3</b>	2 <i>R</i>	Diamond	Full	Yes
<b>Cel 4</b>	2 <i>R</i>	Quadrangular	Full	Yes
<b>Cel 5</b>	3 <i>R</i>	Diamond	Full	Yes
<b>Cel 6</b>	4 <i>R</i>	Diamond	Full	Yes
<b>Cel 7</b>	6 <i>R</i>	Diamond	Full	Yes

#### 4.2.5.1 Mesh size parametrization

The mesh size is a key feature to optimize since a coarser mesh can produce fast and inaccurate models and the refined one a slow but accurate one. Engineering in FEM is about compromise, guarantying that the model represents at some extent the physical parameters of interest in adequate computation time.

The software has a powerful mesh generator by default adequate for standard geometries and adequate tools to test them (e.g. mesh quality). Since the model geometry is relatively regular the volume elements meshing relying solely in automatic meshing revealed inaccurate and don't comply with meshing good practices. Both symmetry, mesh size propagation from singularities and homogeneity weren't fulfilled in automatic meshing. This way three mesh sizes lower than model dimensions were adequate for regular and larger areas. In singular elements like ellipsoidal shaped the EC the mesh size was refined by at least 1/8 of the previous size ensuring that singularities discretization was adequate. With the adjustments made previously the mesh sizes named "Coarse", "Normal" and "Fine" depicted in Table 4.10. The finite elements shape is hexahedral.

*Table 4.10 - Resume table of simulation parameters in mesh size parametrization.*

	<b>Coarse</b>	<b>Normal</b>	<b>Fine</b>
Mesh Size	6 $\mu\text{m}$	3 $\mu\text{m}$	1,5 $\mu\text{m}$
# Finite Elements	78k	126k	370k
Computation Time	2h 38min	3h 40min	16h 21min
Average Mesh Quality	0,590	0,607	0,667
Minimum Mesh Quality	0,014	0,015	0,030

Table 4.10 shows that increasing refinement leads to the number of finite element increase, from 78k to 370k. The computational time also increases from 2h: 38min to 16h: 21min with the refinement. The parameters of average and minimum mesh quality given by the software also increase with the refinement. The fact that "Coarse" and "Normal" refinements have minor differences in mesh qualities can, in some extent explain the lower increase observed in computational time. Looking at the wall shear stress parameters presented in Figure 4.28 individually an apparent constancy of the parameters is observed except for the wall shear stress lateral deviation to the cell zenith.

The maximum shear stress ( $\tau_{max} \approx 2.5Pa$ ) exhibited a value slightly higher to that presented in Table 4.3 ( $\tau_{avg} = 2.0Pa$ ). This happens because EC cause a channel constriction and therefore in these

salient elements the wall shear stress is higher. The  $\tau_{max}$  average and standard deviation increases slightly with mesh refinement that could be imputed to the slight channel constriction caused by higher

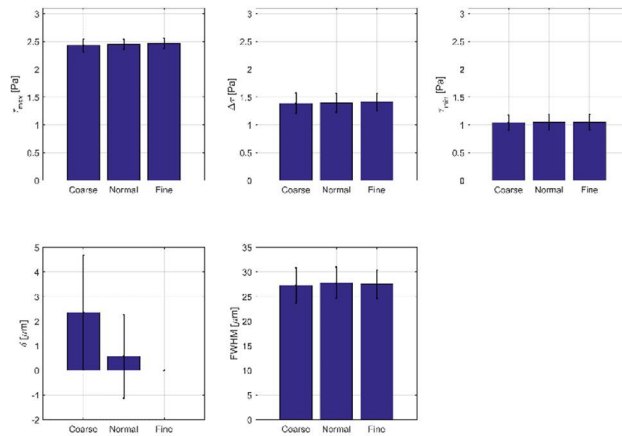


Figure 4.28 - Bar charts of shear stress parameters analysis in mesh size parametrization with average values and standard deviation.

discretization of EC finite elements. Both the stress prominence ( $\Delta\tau$ ) and minimum shear stress ( $\tau_{min}$ ) are relatively stable with values of  $\Delta\tau \approx 1.5Pa$  and  $\tau_{min} \approx 1.0Pa$ . The full width at half maximum  $FWHM$  exhibited constancy along the three mesh refinement both in average and standard deviation. The  $FWHM \approx 28\mu m$  is close to the cell radius. Both  $\Delta\tau$ ,  $\tau_{min}$  and  $FWHM$  show little sensitivity to mesh refinement since these values are probed between two EC cells where the mesh discretization is less relevant.

The only wall shear stress parameter that wasn't stable and decreased dramatically from the "Coarse" to the "Fine" model was wall shear stress lateral deviation with respectively  $\delta \approx 2\mu m$  and  $\delta \approx 0\mu m$ . This parameter should be ideally zero since little lateral deviations should be observed in steady state conditions since it is expected that the cell zenith exhibits the higher wall shear stress due to lower protection and model symmetry. The fact that this lateral deviation decreases with mesh refinement also supports that this finding is derived from numerical errors. With exception of lateral deviation, all parameters fulfil the Chi-square distribution detailed in Table 4.11 for "Coarse" and "Normal" mesh.

Table 4.11 – Shear stress parametrization for mesh size analysis on Coarse, Normal and Fine meshes. Last two columns refer respectively to Chi-square inverse cumulative distribution function and condition verification with a 95% confidence.

Parameter	Model	Average	Standard Deviation	Chi-Square	Test Chi-Square
<b>Max. SS</b> $\tau_{max} [Pa]$	Coarse	2,43	0,12	0,78	1
	Normal	2,45	0,09	0,44	1
	Fine	2,46	0,09	0,46	1
<b>Ass. Dist.</b> $\delta [\mu m]$	Coarse	2,35	2,32	324	0
	Normal	0,57	1,71	719	0
	Fine	0,00	0,00	0,00	1
<b>Prominence</b>	Coarse	1,39	0,19	113	1

$\Delta\tau$ [Pa]	Normal	1,40	0,17	114	1
	Fine	1,41	0,16	112	1
Width FWHM [ $\mu\text{m}$ ]	Coarse	27,26	3,58	67	1
	Normal	27,81	3,18	52	1
	Fine	27,52	2,93	44	1
Min. SS $\tau_{\text{max}}$ [Pa]	Coarse	1,04	0,14	2,68	1
	Normal	1,05	0,14	2,55	1
	Fine	1,05	0,14	2,50	1

All parameters were stable only if using the “Fine” mesh. This was chosen to continue the study although it meant increasing the computational cost. The introduction of singular elements in the analysis increased even further the computation time as detailed in the following section.

#### 4.2.5.2 Cell disposition parametrization

The influence of cell disposition can influence the shear stress, supposed at the cell wall. Therefore, several parameters were studied to understand this influence. They are: cell distance, presence of anti-fouling pillars, the unit cell organization and cell array size. The seven CFD model simulation parameters are presented in Table 4.12.

Table 4.12 - Resume table of simulation parameters in cell disposition parametrization.

Configuration	Cel 1	Cel 2	Cel 3	Cel 4	Cel 5	Cel 6	Cel 7
Number of Cells	120	42	120	168	78	60	42
% of Cell Area in Flow							
Area	27,3%	9,6%	27,3%	38,2%	17,8%	13,7%	9,6%
Mesh Size [ $\mu\text{m}$ ]	1,5	1,5	1,5	1,5	1,5	1,5	1,5
# Finite Elements	370k	321k	387k	435k	360k	344k	326k
Computation Time [hh:mm]	16:21	11:38	15:47	17:48	12:46	12:20	11:30
Average Mesh Quality	0,667	0,677	0,632	0,607	0,635	0,645	0,658
Minimum Mesh Quality	0,030	0,012	0,004	0,0005	0,0069	0,0041	0,0055

The number of finite elements was obtained between 321k and 435k. The computation time decreases as distance increases the model since complexity reduces singular points between EC contact are fewer. Note that Cel 2 has the smallest quantity of cells because the average mesh quality is similar amongst the models, however the minimum mesh quality increases for Cel 1 and Cel 2. Mesh quality decreased one order of magnitude with the inclusion of anti-fouling pillars from Cel 3 to 7 that can be attributed to the emergence of additional singular elements.

The wall shear stress parameters analysis for the cell disposition parametrization is presented in Figure 4.29 and Table 4.13.

Table 4.13 – Shear stress parametrization for different cell configurations.

Configuration	Cel 1	Cel 2	Cel 3	Cel 4	Cel 5	Cel 6	Cel 7
Max. SS $\tau_{max} [Pa]$	$2,46 \pm 0,09$	$2,28 \pm 0,12$	$2,46 \pm 0,09$	$2,53 \pm 0,09$	$2,60 \pm 0,08$	$2,57 \pm 0,07$	$2,52 \pm 0,08$
Ass. Dist. $\delta [\mu m]$	$0 \pm 0$	$0 \pm 0$	$0 \pm 0$	$1,27 \pm 1,71$	$1,40 \pm 1,91$	$1,18 \pm 1,82$	$1,65 \pm 2,18$
Prominence $\Delta\tau [Pa]$	$1,41 \pm 0,16$	$1,37 \pm 0,15$	$1,41 \pm 0,16$	$1,59 \pm 0,15$	$1,77 \pm 0,08$	$1,67 \pm 0,26$	$1,71 \pm 0,07$
Width $FWHM [\mu m]$	$27,52 \pm 2,93$	$28,13 \pm 1,85$	$27,52 \pm 2,93$	$29,43 \pm 1,77$	$32,14 \pm 0,87$	$31,63 \pm 4,6$	$33,31 \pm 0,66$
Min. SS $\tau_{min} [Pa]$	$1,05 \pm 0,14$	$0,91 \pm 0,03$	$1,05 \pm 0,14$	$0,95 \pm 0,11$	$0,83 \pm 0,02$	$0,90 \pm 0,27$	$0,80 \pm 0,02$

The maximum shear stress ( $\tau_{max} = 2.60 \pm 0,08 Pa$ ) and prominence ( $\Delta\tau = 1,77 \pm 0,08 Pa$ ) is observed for cel 5 with spacing between cell of 3 times the radius of the cell ( $3R$ ). Cel 2 when compared to Cel 1 exhibits the influence of the channel constriction that must be ignored since there is a small flow readjustment to bypass the EC group. The minimum shear stress exhibited between cells, appears to decrease with increasing distance that is in line with the reduction of the channel constriction. The full width at half maximum  $FWHM$  increases from  $2R$  to  $3R$  spacing to stabilize for larger spacings denoting its reduced influence for lower EC density. The lateral deviation for Cel 4 to 7 distribution exhibit large

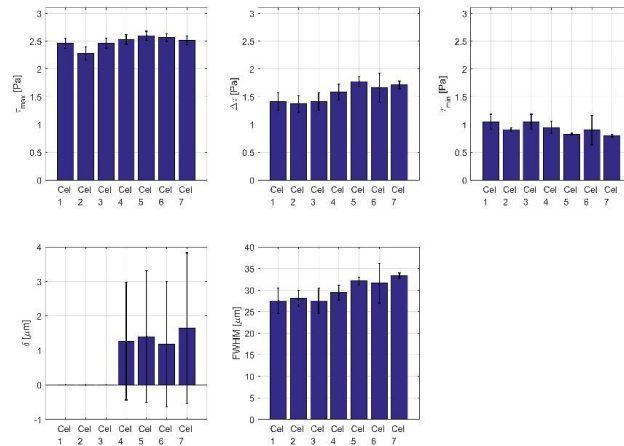


Figure 4.29 - Bar charts of shear stress analysis for different cell configurations.

values (ranging from  $1.18\mu m$  to  $1.65\mu m$ ) that don't comply with a normal distribution given supported by chi-square test. Refining the mesh could be a solution to comply with chi-square test. Quadrangular configuration increases both maximum shear stress ( $\tau_{max}$ ) and prominence ( $\Delta\tau$ ) relative to the diamond configuration. The latter can be derived from the fact that a diamond configuration creates a heterogeneous surface roughness in the streamwise configuration whilst the quadrangular one creates rifts between EC in this direction contributing for higher flow variations in these areas and consequently the shear stress. The lateral deviation is lower in the diamond shape due to the higher distance along the orthogonal directions  $x$  and  $y$ . The wall shear stress magnitude is comparable to the estimated  $\tau_{avg} \approx 2.0 Pa$  presented in Table 4.3 using (2.9).

## 4.3 Experimental Validation

To validate the results from GG concentration profile simulations, it was necessary to fabricate and test the device as explained earlier. The next two sub-chapters will describe the results regarding fabrication and experimental validation.

The validation of the conditions of both GG and SS that constitute the microfluidic device was made separately to enable the detachment of the interaction between the two PDMS parts. Experiments consist on the determination of the GG concentration profile based on the relative image light intensity and flow rate measurement. The flow rate imposed by the syringe pump was previously calibrated based on the mass of liquid and time it took to fill a 1mL Eppendorf.

### 4.3.1 Concentration gradient determination

The concentration gradient determination required the prior model calibration for the six images taken in GG (Figure 3.16) using a non-linear model homogenized to a DI water solution. The following step consisted determining of the effective concentration at any point of the alignment and establish a comparison between the mixer exit and the membrane entrance. Finally the gradient of concentration was compared to previous work started of Brandão & Silvério (2016).

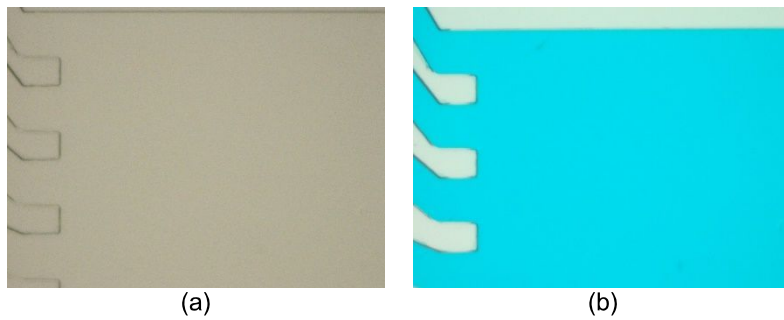


Figure 4.30 – (a) Image light intensity obtained for GG with DI water in all inlets at mixer exit in zone 1 ( $I_0$ ). (b) Image light intensity obtained for GG with dye solution with concentration 1:20 in all inlets in zone 1 ( $I_i$ ).

#### 4.3.1.1 Model calibration

The average image light intensity for the different concentrations tested were corrected by the reference light intensity obtained for the system with DI water to enable the model calibration (Figure 4.30). The calibration starts with image alignment, intensity computation ( $I_i$ ), relative intensity computation ( $I_i/I_0$ ), that requires a previous image alignment, and estimation of the intensity dependence  $I_i/I_0$  from concentration  $c_i$ .

The results of the relative image light intensity and fit are presented in Figure 4.31 and Table 4.14 and show that most of relative intensity is precise with exception of 1: 10 dilution that presents a higher standard deviation (0,058). It is also relevant that between the concentration 1: 100 and 1: 200 there are virtually no differences that can cause model discrepancies for low concentrations.

Table 4.14 – Mean values and standard deviations for relative intensity.



Concentration	Mean	Standard deviation
1:200	0,920	0,009
1:100	0,920	0,022
1:20	0,882	0,025
1:10	0,838	0,058
1:2	0,705	0,032
1:1	0,672	0,017

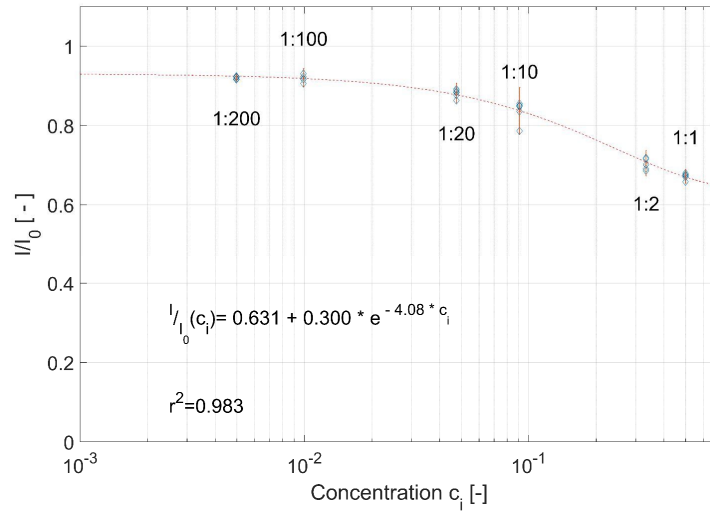


Figure 4.31 - Parametrization of relative light intensity with solution concentration.

The  $r^2$  value is nearly 1 (Table 4.15), however, the interval of confidence of the fit parameters have a relative standard deviation ranging from 5% to 25% indicating that it is critical to accommodate the extreme concentrations of 1: 200 and 1: 1. The model parameter values and interval of confidence are presented in Table 4.15.

Table 4.15 – Model fit parameter and interval of confidence.

Value	Value	Standard Deviation
<b>a</b>	0.6311	0.0306
<b>b</b>	0.2996	0.0274
<b>c</b>	4.079	1.028
<b>r<sup>2</sup></b>	0.9832	-

#### 4.3.1.2 Determination of concentration gradient in the gradient generator

The concentration gradient was obtained along the two alignments of reference, the GG mixer exit and the PETE membrane entrance. The three images alignment and the constancy of the vector length intensity was an issue that was resolved in two steps. The first step consisted in the selection of an alignment without bubbles and detection of common visual markers between consecutive images by inspection that enabled the matching between the three images (Figure 4.32). The second step consisted in the truncation of the intensity vectors according to the smaller vector length for images taken in the same area. This compromise enabled the correct matching between pixels and further homogenization of brightness.

Figure 4.33 depict the images taken from zones 1 to 6, its alignment markers, the relative intensity profile along the alignment and finally an estimate of the concentration based on fit parameters from

Table 4.15. Along with the concentration profile, the CFD results obtained in section 4.2.4 are presented, enabling a direct comparison between numerical and experimental results. These figures consider the experimental setup ranges for the lower and higher velocities  $U = \{0.1 ; 20\} \text{ mm.s}^{-1}$  to highlight its influence in mass transport. The complete experimental setup consider two additional velocities and is depicted in Figure A.3 and Figure A.4.

Figure 4.33 show that the alignment amongst images in the mixer outlet (zone 1 to 3) and membrane entrance (zone 4 to 6) was maintained and that artifacts like bubbles were avoided.

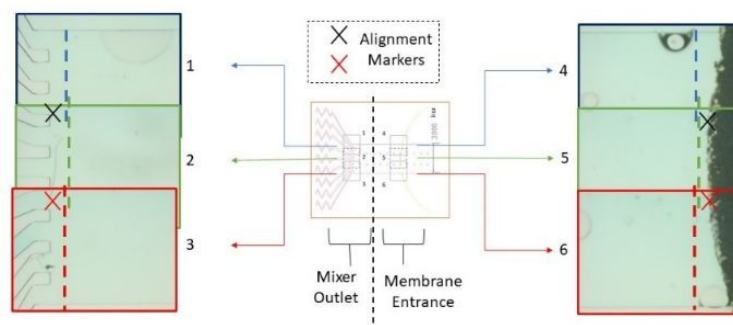


Figure 4.32 – Image alignment in mixer outlet (zones 1,2 and 3) and membrane entrance (zones 4, 5 and 6). The coloured dash lines were slightly misaligned in the scheme to favour visualization.

Observing the concentration profiles of Figure 4.33 (a) and Figure 4.34 (a) of five transition areas that are coincident with areas where two microchannels converge. However, it is not possible to see the eighth transition areas provided by the CFD analysis, speacilly for higher concentrations (zone 1). The mixer performs better with lower velocities which agrees with the increasing of the Peclet number, derived Reynolds number increase due to the increasing velocity that makes the mass transport less sensible to the diffusion. In Figure 4.33 (c) and Figure 4.34 (c), that have higher velocity ( $U = 20.0 \text{ mm.s}^{-1}$ ), it is possible to see only two transition that don't comply with the CFD analysis provide different results and yeld the same eight transition areas. This difference can be atributed to both model simplifications in the CFD analysis or a defective PDMS-glass bonding in the mixer area. Comparing the CFD analysis of (a) with (c) images the concentration range is sligtly wider in the transition areas due to the influence fo convective transport for lower velocities ((a)  $U = 0.1 \text{ mm.s}^{-1}$ ).

Looking at concentrarion profiles of Figure 4.33 (b) and Figure 4.34 (d) there aren't clear transition areas that are compliant with the CFD analysis. For lower velocities ( $U = 0.1 \text{ mm.s}^{-1}$ ), Figure 4.31 (b) and Figure 4.34 (b) it is possible to see that the experimental results are compliant with CFD analysis in most of the section profile. For higher velocities ( $U = 20.0 \text{ mm.s}^{-1}$ ), for Figure 4.33 (d) and Figure 4.34 (d) the concentration profile should be very similar to the ones presented in the mixer outlet zone (Figure 4.33 (c) and Figure 4.34 (c)) due to the lower influence of diffusive transport that is supported by the CFD analysis. A possible explanation for this deviation is that the membrane zone for higher flow rate, and consequently higher pressures could have been empolated in zone 6 and exhibited a higher relative intensity that yelds a lower concentration. This hypothesis is supported by the weak bonding between PETE membrane and both PDMS and glass ((Aran et al. 2010)). Another cause can be atributed to the fact that the PETE membrane creates a constriction in the channel and influences the flow upstream. The existance of the PDMS pillars are assumed to be perfectly circular and aligned but in the fabrication

process the PDMS peeling could have caused volume modifications and with irregularities the flow virtual subsectioning in the developing zone could be more diffuse and enhanced the spanwise diffusion contributing for the higher degradation of the concentration profile.

Despite the image alignment the relative intensity along the superposition areas exhibit a vertical drift which indicates that the brightness homogeneization failed partially. This vertical drift results in a concentration difference that differs less than one order of magnitude.

Another important finding is that the concentration profile is comprised between the concentration boundaries in most of the experimental results. The only exceptions are those in Figure A.3 in the membrane entrance ((e) and (h)) for  $U = \{10.5; 20\} \text{ mm.s}^{-1}$  and in Figure A.4 ((d),(e) and (h)) for  $U = \{1.5; 10.5; 20\} \text{ mm.s}^{-1}$  for the lower concentration range. Comparing the right ((a), (c), (e) and (g)) to the left ((b), (d), (f) and (h)) figures the last finding is relevant to observe the increasing influence of diffusion in smaller velocities with the degradation of the concentration profile to a flatter one. This finding cannot be observed for all velocities due to the vertical drift evoked previously.

The relative uncertainty of the concentration method was computed for the six zones in the different experiments performed in Table 4.16. shows that the zones with higher concentration (zone 1 and 4) in the influence of inlet  $c_{I1}$  and  $c_{I2}$  are more accurate than lower concentration zones. The concentration evaluation at the mixer outlet (zones 1 to 3) is more precise and homogeneous globally than the

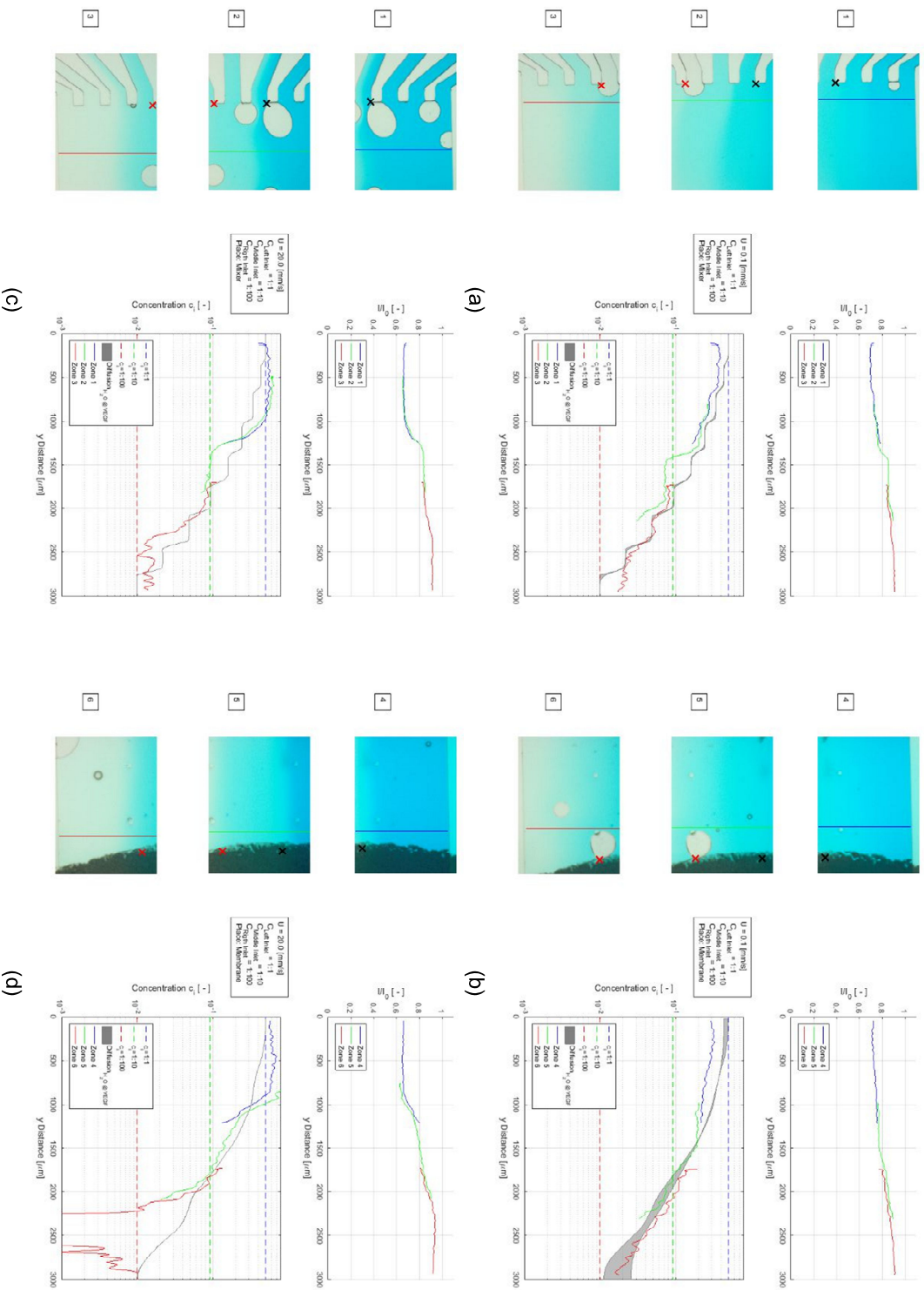


Figure 4.33 – Concentration gradient determination in the mixer based on the relative light intensity for inlets with concentration ( $c_1 = 1:1$  ;  $c_2 = 1:10$  ;  $c_3 = 1:100$ ). Parametrization on velocity from top to bottom ( $U = \{0.1 ; 20.0\} \text{mm.s}^{-1}$ ). Measurement taken at mixer exit and membrane entrance, respectively left and right images.

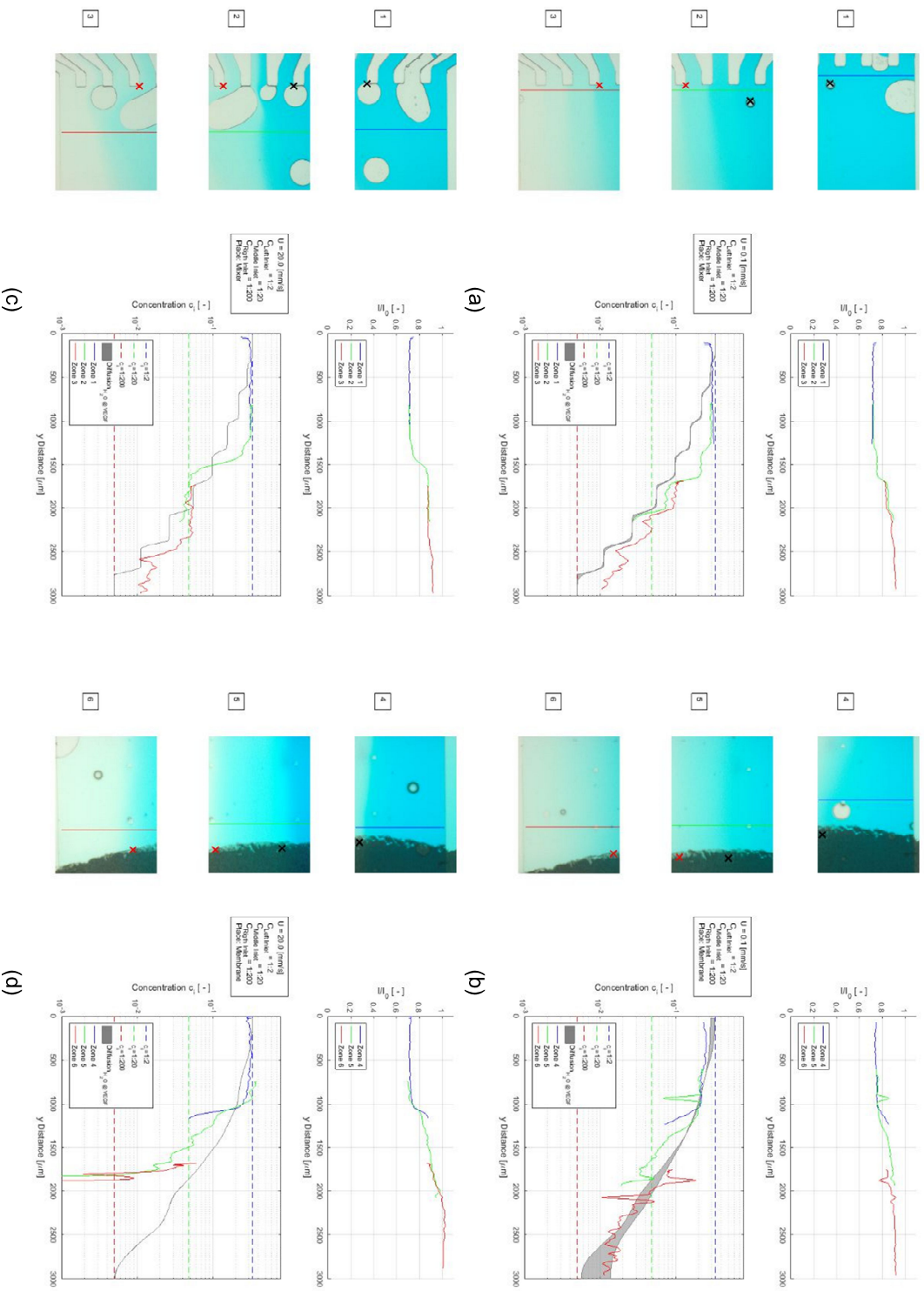


Figure 4.34 – Concentration gradient determination in the mixer based on the relative light intensity for inlets with concentration ( $c_1 = 1:2$  ;  $c_2 = 1:20$  ;  $c_3 = 1:200$ ). Parametrization on velocity from top to bottom ( $U = \{0.1 ; 20.0\}mm.s^{-1}$ ). Measurement taken at mixer exit and membrane entrance, respectively left and right images.

membrane entrance (zones 4 to 6). However, if Figure 4.33 (d) is considered to be an outlier ( $\delta_r = 292\%$ ) and is removed from the analysis the systems have similar performance, ( $\delta_{r,Outlet} = 44\%$ ) in the mixer outlet and ( $\delta_{r,Membrane} = 41\%$ ) in the membrane entrance.

*Table 4.16 – Relative uncertainty of concentration determination for the six zones of GG and figures correspondence.*

Inlet Concentration	Mean Velocity	Zone 1	Zone 2	Zone 3	Zone 4	Zone 5	Zone 6		
$c_{I1} ; c_{I2} ; c_{I3} [-]$	$U [mm/s]$	$\delta_r [\%]$	$\delta_r [\%]$	$\delta_r [\%]$	$\delta_r [\%]$	$\delta_r [\%]$	$\delta_r [\%]$	Figure	Annexes
1:1 ; 1:10 ; 1:100	0,1	38%	66%	80%	13%	27%	26%	4.31 (a) (b)	A.20 (a) (b)
1:2 ; 1:20 ; 1:200	0,1	35%	43%	32%	11%	51%	69%	4.32 (a) (b)	A.21 (a) (b)
1:1 ; 1:10 ; 1:100	1,5	51%	53%	47%	26%	53%	87%	-	A.20 (c) (d)
1:2 ; 1:20 ; 1:200	1,5	35%	54%	80%	18%	65%	292%	-	A.21 (c) (d)
1:1 ; 1:10 ; 1:100	10,5	19%	30%	26%	28%	16%	15%	-	A.20 (e) (f)
1:2 ; 1:20 ; 1:200	10,5	25%	57%	51%	28%	37%	43%	-	A.21 (e) (f)
1:1 ; 1:10 ; 1:100	20	13%	51%	53%	15%	52%	80%	4.31 (c) (d)	A.20 (g) (h)
1:2 ; 1:20 ; 1:200	20	36%	44%	29%	38%	49%	64%	4.32 (c) (d)	A.21 (g) (h)
		<b>32%</b>	<b>50%</b>	<b>50%</b>	<b>22%</b>	<b>44%</b>	<b>85%</b>		

## 4.3.2 Flow rate measurement

### 4.3.2.1 Shear stress generator

The volumes obtained for SS experiment is presented in Table 4.17. Despite the initial goal was to obtain a  $1mL$  volume the measurements for  $U = \{0.1, 1.5, 10.50, 20\} mm.s^{-1}$  that wasn't maintained in all specially in the slower setup ( $U = 0.1mm.s^{-1}$ ) that would yield almost five hours. The volume computation was made considering a water density at  $20^\circ C$  ( $\rho = 998.2 kg.m^{-3}$ ).

*Table 4.17 - Flow estimation in Shear Stress Generator.*

$Q_{set}$ [uL / min]	$U_{set}$ [mm/s]	$\Delta m \pm \sigma_{\Delta m}$ [g]	$V \pm \sigma_V$ [uL]	$t \pm \sigma_t$ [min]	$Q_{meas} \pm \sigma_Q$ [uL / min]	$\delta r_Q$ [%]	$Er_Q$ [%]
2,7	0,1	$0,5555 \pm 0,0004$	$556,5 \pm 0,4$	$215,00 \pm 0,02$	$2,588 \pm 0,003$	0,1%	4,1%
40,5	1,5	$0,8733 \pm 0,0007$	$874,9 \pm 0,7$	$22,75 \pm 0,02$	$38,46 \pm 0,04$	0,1%	5,0%
283,5	10,5	$0,8680 \pm 0,0008$	$870,0 \pm 1,0$	$3,17 \pm 0,02$	$274,6 \pm 0,4$	0,1%	3,1%
540	20	$0,8088 \pm 0,0006$	$810,0 \pm 1,0$	$1,60 \pm 0,02$	$506,0 \pm 1,0$	0,1%	6,2%

The flow rate was obtained for the different velocities with error increasing for higher flow rates. This could be to the fact that the measured time and volume filled stopping operation must be performed simultaneously that can result in a small discrepancy. The largest error is slightly superior than 6% that isn't explained by the relative deviation of the experimental setup, that is about 0.1%

### 4.3.2.2 Gradient generator

The volumes obtained for GG experiment is presented in Table 4.18. Despite the initial goal was to obtain a  $1mL$  volume the measurements for  $U = \{0.1, 1.5, 10.50, 20\} mm.s^{-1}$  that wasn't maintained in all specially in the slower setup ( $U = 0.1mm.s^{-1}$ ) that would yield almost six hours.

Table 4.18 - Flow estimation in Gradient Generator.

$Q_{set}$ [ $\mu\text{L} / \text{min}$ ]	$U_{set}$ [ $\text{mm/s}$ ]	$\Delta m \pm \sigma_{\Delta m}$ [ $\text{g}$ ]	$V \pm \sigma_V$ [ $\mu\text{L}$ ]	$t \pm \sigma_t$ [ $\text{min}$ ]	$Q_{meas} \pm \sigma_Q$ [ $\mu\text{L} / \text{min}$ ]	$\delta r_Q$ [%]	$Er_Q$ [%]
1,8	0,1	$0,4804 \pm 0,0003$	$481,2 \pm 0,3$	$277,00 \pm 0,02$	$1,737 \pm 0,002$	0,1%	3,5%
27	1,5	$1,0718 \pm 0,0006$	$1073,7 \pm 0,6$	$40,67 \pm 0,02$	$26,40 \pm 0,02$	0,1%	2,2%
189	10,5	$0,9831 \pm 0,0012$	$985,0 \pm 1,0$	$5,30 \pm 0,02$	$185,8 \pm 0,3$	0,2%	1,7%
360	20	$0,9733 \pm 0,0052$	$975,0 \pm 5,0$	$2,82 \pm 0,02$	$346,0 \pm 3,0$	0,8%	3,8%

The flow rate was estimated for the several velocities with an increasing error for faster flow rates. This could be to the fact that the measured time and volume filled stopping operation must be performed simultaneously that can result in a small discrepancy. The largest error is lower than 4% that isn't explained by the relative deviation of the experimental setup, that is about 0.8% in the worst case. Note that the volume contained in the PTFE tubing is lower than 9000 [ $\mu\text{L}$ ]. This way even the smaller droplet can influence the results.





## 5 Conclusions and Future Work

Microfluidic technology has been disseminated in cellular applications due to the ease of fabrication, better parameter control and low cost. Presently, the emergence of the Organ-on-a-Chip concept is pushing specialists from different fields, like engineering and life sciences, to work together to mimic physiological conditions adequately and defy the state of the art.

The goal of this project was to design and fabricate a microfluidic device at INESC-MN facilities that generate simultaneously a VEGF gradient and a shear stress experienced by a group of EC in response of this competing stimulus in cell polarization proposed by IMM.

The microfluidic device was designed considering the geometric and logistic limitations of the PETE membrane where the EC were to be expand. The microfluidic device had to enable a reversible bonding between the SS and GG to allow reproducibility of the experiments. The EC on the PETE membrane face the SS microchannel and both devices included anti-fouling columns to avoid the channels ablation due to larger channel aspect ratio that can be respectively 30: 1 and 45: 1 in GG and SS.

Both device components were drawn in CAD software, simulated in FEM commercial software, fabricated and tested in INESC-MN cleanroom and biolab facilities, respectively. The microfluidic pattern design respected the m.f.s. of the fabrication process, the maximum dimensions allowed by the standard substrate dimensions  $5 \times 5 \text{ cm}^2$  including margins and alignment marks. The fabrication of the microfluidic components was made in PDMS using soft-lithography techniques, starting with a deposition of Aluminium thin film patterned in a glass substrate, PDMS molding with a SU-8 resist in a Silica substrate and finally the PDMS casting.

The device components required a sealing to work properly that could be reversible or irreversible. The reversible sealing was attained with a three component PMMA holder assembled through passing holes with bolts and nuts. This setup enabled an adjustable mechanical sealing and adequate microscope observation. The irreversible sealing setup was achieved coupling one of the PDMS structures (SS or GG) to the PETE membrane and a glass substrate. This setup was required for the experimental setup. The bonding of PETE membrane to both PDMS and glass substrate isn't guaranteed exhibiting fluid accumulations for higher pressures.

The design of the microfluidic device was assisted by the simulation of the GG and SS in FEM commercial software and additional simplified computations to estimate the model parameters and its magnitude. The first computation included the estimate of flow rate relation between SS and GG ( $0.8 \times Q_{SS} \approx Q_{GG}$ ) to balance the PETE membrane pressure preventing leakages between microchannels and the magnitude of wall shear stress in SS ( $\tau_{SS} \approx 2 \text{ Pa}$ ). The second computation included the estimate of the effective diffusive time to know in advance the minimum simulation time of the GG model that should be larger than  $0.13 \text{ s}$  for  $U = 20 \text{ mm.s}^{-1}$  and  $D = 1 \times 10^{-9} \text{ m}^2.\text{s}^{-1}$  and  $3.6 \text{ s}$  for  $U = 0.1 \text{ mm.s}^{-1}$  and  $D = 5 \times 10^{-11} \text{ m}^2.\text{s}^{-1}$ .

The determination of the effective diffusive time in the in the GG CFD model validated that for the range of flow rate intended the establishment of a transient regime was inferior to  $4 \text{ s}$  in the model and

in working conditions should be inferior to the convective time in the streamwise direction added to the convection time in the spanwise direction. The SS CFD model allowed the model validation and the determination of the wall shear stress in the EC. Initially, the model meshing was fine tuned to ensure that the wall shear stress parameters variation followed a distribution independent of numerical errors. The second analysis considered several cell dispositions and presence of anti-fouling columns. From this analysis it was possible to assess that the WSS magnitude  $\tau_{max} \approx 2.5 Pa$  was superior to the reference wall shear stress for a EC free channel estimated to be  $\tau_{avg} \approx 2.0 Pa$ . From the study it was also possible to conclude that related to the wall shear stress magnitude of the anti-fouling columns increases it due to the section constriction that increases the flow rate in the effective area. The diamond cell disposition induces lower wall shear stress than square disposition that can be attributed to the creation of rifts between EC in the streamwise direction contributing for higher flow variations in these areas and consequently the shear stress.

Regarding the cell spacing the  $3R$  spacing lead to the higher value of wall shear stress magnitude. The full width at half maximum *FWHM* increases from  $2R$  to  $3R$  spacing to stabilize for higher spacing denoting the reduced influence of cell spacing with lower degree of EC density.

The validation of GG and SS conditions was made separately to enable the detachment of the interaction between the two PDMS devices.

The first experiment consisted on the determination of the concentration profile based on the relative intensity resorting to basic imaging processing techniques. The homogenization standardization processes allowed the intensity correction and later model fit determination. However, contributed for the appearance of discrepancies in the superposition areas between consecutive images and led to a minor loss of information, namely the reduction of the vector length. For low flow rates the mass transport is diffusive-convective for lower velocities and the transport is convective for higher flow rates.

The experimental results exhibit some concordance with CFD analysis for lower velocities  $U = \{0.1; 1.5\} mm.s^{-1}$  in a qualitative way, supported by the definition of transition areas coincident with the mixer outlet microchannels confluence. In the membrane entrance the concentration profile for these velocities exhibit a larger degradation that could be due to enhanced mixing derived from the PDMS peeling. The latter could cause velocity field modification that enhance diffusion in the spanwise direction.

For higher velocities  $U = \{10.5; 20.0\} mm.s^{-1}$  the mixer performed poorly without the definition of all transition areas contemplated in the CFD analysis in the mixer outlet. This finding could be due to CFD model simplification, defective PDMS-glass bonding in the mixer area or PDMS hydrophobic nature that reduces effective cross section area increasing flow rate mean velocity. Additionally, discounting the mixer efficiency, the concentration profiles between profiles computed in the mixer outlet and membrane entrance should be similar due to the dominance of convective transport. These deviations could be attributed to the presence of PETE membrane whose bonding is weak and cause blister in the area. This blister causes a spanwise fluid dispersion, a virtual increase in the relative intensity and lower concentration that result in larger variations to the concentration profile obtained in CFD analysis.

The second experiment consisted in the measurement of the flow rate and with known microfluidic device channels dimensions to determine the average velocity. The experiment validated the flow rate with error by defect with relative errors lower than 6.2% for SS and 3.8% for GG. This tendency for having lower flow rates than expected can be derived from faulty detachment of water droplets and desynchronization between pump and clock start and stop instants.

Some improvements could be made to increase the microfluidic device effectiveness. Bearing in mind that prototyping is an iterative process, testing the microfluidic device with EC would be benefic for the design process since it would lead to the solution of problems derived from its usage.

Since minor leakages between SS and GG were observed for some experimental conditions, namely for higher flow rates that lead to high pressures, testing the microfluidic device with an impermeable layer or with EC could solve this issue. To solve the membrane ablation problem a different anti-fouling column disposition in diamond could be experimented. Despite leading to a uniform shear stress spatially, it would lead to the appearance of two dominant directions with a 45° angle from the streamwise direction. Another strategy that could be used for the gradient generation would be the seeding of EC in a membrane embedded in VEGF gradient that required only one channel to fulfil the requirements.

Regarding the experimental setup, the use of a flowmeter would be benefic, and it would allow the determination of the transient flow rate response due to the syringe pump than can lead to a non-constant flow rate. To increase the reliability, a pressure pump could be used constituting however an expensive solution.

Regarding the model simulation, the CFD model will lead to a higher bound of the shear stress, since the EC have a hydrodynamic shape that leads to lower shear stresses. Another key issue is that cells are constituted by a cellular membrane that isn't rigid and can exhibit a dynamic response according to the flow rate imposed. In physiological conditions the flow rate can be approximated to a pulsatile flow and an additional feature to consider would be the Fluid-Structure Interaction that could lead to important findings. The cellular membrane stiffness could be calibrated determining the cell dynamic response to several stimuli using 3D microscopy with a minimum time resolution of 10Hz.



## 6 References

- Abaxis. 1995. "VetScan." 1995. <https://www.abaxis.com/veterinary/products/vetscan-vs2>.
- Aran, Kiana, Lawrence A Sasso, Neal Kamdar, and Jeffrey D Zahn. 2010. "Irreversible, Direct Bonding of Nanoporous Polymer Membranes to PDMS or Glass Microdevices" 10 (5):548–52. <https://doi.org/10.1039/b924816a.Irreversible>.
- Beebe, David J., Glennys A. Mensing, and Glenn M. Walker. 2002. "Physics and Applications of Microfluidics in Biology." *Annual Review of Biomedical Engineering* 4 (1):261–86. <https://doi.org/10.1146/annurev.bioeng.4.112601.125916>.
- Bel-Art™. 2017. "BEL-ART 'Space Saver' Vacuum Desiccator; 0.31 CU. FT." 2017. <https://www.belart.com/bel-art-f42032-0000-space-saver-polycarbonate-pp-desiccator-9-i-d-10-flange-o-d-12-height-14cm-plate-diameter.html>.
- Bernoulli, Daniel. 1738. *Hydrodynamica*. University Heidelberg.
- Berthier, J, and P Silberzan. 2006. *Microfluidics for Biotechnology. Artech House Microelectromechanical Systems MEMS Series*. Vol. 1. [https://doi.org/10.1002/1521-3773\(20010316\)40:6<9823::AID-ANIE9823>3.3.CO;2-C](https://doi.org/10.1002/1521-3773(20010316)40:6<9823::AID-ANIE9823>3.3.CO;2-C).
- Brandão, Pedro, and Vânia Silvério. 2016. *Gradient Generator - Instructions for Usage*. 1sted. Lisbon: INESC-MN.
- Bruus, Henrik. 2006. *Theoretical Microfluidics. DTU Lectures*. <https://doi.org/10.1111/j.1574-6968.2009.01808.x>.
- . 2007. *Theoretical Microfluidics. Oxford Master Series*. 2nded. Vol. 1. Oxford: Oxford University Press. <https://doi.org/10.1017/CBO9781107415324.004>.
- C&D Semiconductor Services™. 2017. "SVG8x Track System Datasheet." 2017. <https://cdsemi.com/wp-content/uploads/2016/07/SVG8X-V2-Datasheet.pdf>.
- Cooksey, Gregory A, Anne L Plant, and Javier Atencia. 2009. "A Vacuum Manifold for Rapid World-to-Chip Connectivity of Complex PDMS Microdevices" 1 (301):1298–1300. <https://doi.org/10.1039/b820683j>.
- Cussler, E.L. 2007. *Diffusion: Mass Transfer in Fluid System*. 3rd ed. Cambridge: Cambridge University Press.
- Dektak™. 2001. "Dektak 3030 Profilometer." 2001. <http://www.sitekprocess.com/ccp4501-dektak-3030-profilometers-dektak-3030-profiler-50174.htm>.
- DISCO™. 2011. "Disco DAD 321 Dicing Saw." 2011. <http://www.labx.com/item/like-new-disco-dad-321-dicing-saw/3992183>.
- Dow Corning™. 2017a. "SYLGARD® 184 Pack - Base." 2017.
- . 2017b. "SYLGARD® 184 Pack - Curing Agent." 2017.
- Drake, Christopher J. 2003. "Embryonic and Adult Vasculogenesis." *Birth Defects Research Part C: Embryo Today: Reviews* 69 (1). Wiley Subscription Services, Inc., A Wiley Company:73–82. <https://doi.org/10.1002/bdrc.10003>.
- Elveflow. 2011. "FastGene Project." Elveflow. 2011. <http://www.elveflow.com/microfluidic-innovation-center/microfluidics-research-projects/fastgene-microfluidic-lab-on-chip-qpcr-qrtPCR/>.
- FASTER™. 2017. "FlowFAST V." 2017. <http://www.faster-air.com/en/products/laminar-airflow-cabinets/vertical-laminar-airflow-cabinets/flowfast-v>.
- Franco, Claudio A., Martin L. Jones, Miguel O. Bernabeu, Anne Clemence Vion, Pedro Barbacena, Jieqing Fan, Thomas Mathivet, et al. n.d. "Non-Canonical Wnt Signalling Modulates the Endothelial Shear Stress Flow Sensor in Vascular Remodelling." *eLife* 5:1–22. <https://doi.org/10.7554/eLife.07727>.
- Giroux, S., M. Tremblay, D. Bernard, J. F. Cadrin-Girard, S. Aubry, L. Larouche, S. Rousseau, et al. 1999. "Embryonic Death of Mek1-Deficient Mice Reveals a Role for This Kinase in Angiogenesis in the Labyrinthine Region of the Placenta." *Current Biology* 9 (7):369–72. [https://doi.org/10.1016/S0960-9822\(99\)80164-X](https://doi.org/10.1016/S0960-9822(99)80164-X).
- Guysen™. 2017. "MKC Ultrasonic Bath - MKC22." 2017. <https://www.guyson.co.uk/finishing-equipment/ultrasonic-cleaning-baths-tanks/kerry-ultrasonic-cleaning-baths-kc-mkc/mkc22>.
- Harrick Plasma™. 2017. "Plasma Cleaner PDC 002." 2017. <http://harrickplasma.com/products/expanded-plasma-cleaner>.
- Henriksson, Johanna Tukler, Alison M. McDermott, and J. P G Bergmanson. 2009. "Dimensions and Morphology of the Cornea in Three Strains of Mice." *Investigative Ophthalmology and Visual Science* 50 (8):3648–54. <https://doi.org/10.1167/iov.08-2941>.
- Herbert, Shane P., and Didier Y.R. Stainier. 2012. "Molecular Control of Endothelial Cell Behavior during Blood Vessel Morphogenesis." *Nature Reviews. Molecular Cellular Biology* 12 (9):551–64.

- <https://doi.org/10.1038/nrm3176>.Molecular.
- Holz, Manfred, Stefan R. Heil, and Antonio Sacco. 2000. "Temperature-Dependent Self-Diffusion Coefficients of Water and Six Selected Molecular Liquids for Calibration in Accurate 1H NMR PFG Measurements." *Physical Chemistry Chemical Physics* 2 (20):4740–42. <https://doi.org/10.1039/b005319h>.
- Hong, Jong Wook, Vincent Studer, Gao Hang, W French Anderson, and Stephen R Quake. 2004. "A Nanoliter-Scale Nucleic Acid Processor with Parallel Architecture." *Nature Biotechnology* 22 (4):435–39. <https://doi.org/10.1038/nbt951>.
- Hou, Xu, Yu Shrike Zhang, Grissel Trujillo-de Santiago, Mario Moisés Alvarez, João Ribas, Steven J Jonas, Paul S Weiss, Anne M Andrews, Joanna Aizenberg, and Ali Khademhosseini. 2017. "Interplay between Materials and Microfluidics." *Nature Reviews Materials* 2 (5):17016. <https://doi.org/10.1038/natrevmats.2017.16>.
- Huysmans, Marijke, and Alain Dassargues. 2005. "Review of the Use of Péclet Numbers to Determine the Relative Importance of Advection and Diffusion in Low Permeability Environments." *Hydrogeology Journal* 13 (5–6):895–904. <https://doi.org/10.1007/s10040-004-0387-4>.
- Ingber, Donald E. 2003. "Tensegrity II. How Structural Networks Influence Cellular Information Processing Networks." *Journal of Cell Science* 116 (8):1397–1408. <https://doi.org/10.1242/jcs.00360>.
- Jamal, Mustapha, Aasiyeh M Zarafshar, and David H Gracias. 2011. "Differentially Photo-Crosslinked Polymers Enable Self-Assembling Microfluidics." *Nature Communications* 2. Nature Publishing Group:526–27. <https://doi.org/10.1038/ncomms1531>.
- JeLight™. 2015. "UV Cleaning Machine 144AX." 2015. <http://www.jelight.com/uv-ozone-cleaning.html>.
- Jesus, Júlia de, Sofia Oliveira, and Tânia Ferreira. 2012. "Chaminés Industriais." Portugal: Lugar do Real. <http://lugardoreal.com/video/chaminés-industriais>.
- Klemke, R L, S Cai, A L Giannini, P J Gallagher, P de Lanerolle, and D A Cheresh. 1997. "Regulation of Cell Motility by Mitogen-Activated Protein Kinase." *The Journal of Cell Biology* 137 (2):481–92. <https://doi.org/10.1083/jcb.137.2.481>.
- Kwak, Tae Joon, Young Gyu Nam, Maria Alejandra Najera, Sang Woo Lee, J. Rudi Strickler, and Woo-jin Chang. 2016. "Convex Grooves in Staggered Herringbone Mixer Improve Mixing Efficiency of Laminar Flow in Microchannel." Edited by Josué Sznitman. *PLOS ONE* 11 (11):e0166068. <https://doi.org/10.1371/journal.pone.0166068>.
- Lamalice, Laurent, Fabrice Le Boeuf, and Jacques Huot. 2007. "Endothelial Cell Migration during Angiogenesis." *Circulation Research* 100 (6):782–94. <https://doi.org/10.1161/01.RES.0000259593.07661.1e>.
- Laurell™. 2017. "WS-650-23 Spin Coater." 2017. <http://www.laurell.com/spin-coater/?model=WS-650-23>.
- Lee, C. Y., and V. L. Bautch. 2011. "Ups and Downs of Guided Vessel Sprouting: The Role of Polarity." *Physiology* 26:326–33. <https://doi.org/10.1152/physiol.00018.2011>.
- Lee, Hyungseok, and Dong-Woo Cho. 2016. "One-Step Fabrication of an Organ-on-a-Chip with Spatial Heterogeneity Using a 3D Bioprinting Technology." *Lab on a Chip* 16. Royal Society of Chemistry:2618–25. <https://doi.org/10.1039/C6LC00450D>.
- Li, Song, Ngan F. Huang, and Steven Hsu. 2005. "Mechanotransduction in Endothelial Cell Migration." *Journal of Cellular Biochemistry* 96 (6):1110–26. <https://doi.org/10.1002/jcb.20614>.
- Lin, Benjamin, and Andre Levchenko. 2015. "Spatial Manipulation with Microfluidics" 3 (April):1–6. <https://doi.org/10.3389/fbioe.2015.00039>.
- Magnomics. 2013. "Magnomics Products." 2013. <http://www.magnomics.pt/#>.
- Makanya, Andrew N, Daniela Stauffer, Domenico Ribatti, Peter H Burri, and Valentin Djonov. 2005. "Microvascular Growth, Development, and Remodeling in the Embryonic Avian Kidney: The Interplay between Sprouting and Intussusceptive Angiogenic Mechanisms." *Microscopy Research and Technique* 66 (6). United States:275–88. <https://doi.org/10.1002/jemt.20169>.
- Memmert™. 2007. "Universal Oven U." 2007. <https://www.memmert.com/products/heating-drying-ovens/universal-oven/#!filters=%7B%7D>.
- MicroChem™. 2000. "SU-8 Negative Tone Photoresist." 2000. [http://www.microchem.com/pdf/SU8\\_50-100.pdf](http://www.microchem.com/pdf/SU8_50-100.pdf).
- Micronit. 2017. "Microreactors." 2017. <https://www.micronit.de/microfluidic-chips/microreactors/>.
- Nguyen, Nam, and Steven Wereley. 2002. *Fundamentals and Applications of Microfluidics*. 1sted. Norwood: Artech House, Inc.
- Nordiko™. 2014. "Nordiko 7000 Datasheet." <http://www.nordiko.com/products/Nordiko-7000.html>.
- Olympus™. 2000. "Olympus BH3-MJT Microscope Datasheet." 2000. <http://www.alanwood.net/downloads/olympus-bh3-mjla-mjlt-instructions.pdf>.

- . 2017. "Olympus XC30." 2017. <https://www.olympus-lifescience.com/ru/camera/color/xc30/>.
- Rayner's™. 2011. "Rayner's - Blue - Concentrated Food Colouring - 28mL." 2011. <https://www.healthyfoods-online.com/rayner-s-blue-concentrated-food-colouring-28ml>.
- Rosa, Patrícia. 2010. "Microfluidic Devices - Gradient Generation and Control of Local Cellular Environmental for Biomedical Applications." University of Lisbon. <https://doi.org/10.3390/molecules16108368>.
- Ruiz, Ana, Emmanuel Delamarche, and Michela Matteoli. 2012. "Overflow Microfluidic Networks: Application to the Biochemical Analysis of Brain Cell Interactions in Complex Neuroinflammatory Scenarios."
- Ryu, Kee Suk, Kashan Shaikh, Edgar Goluch, Zhifang Fan, and Chang Liu. 2004. "Micro Magnetic Stir-Bar Mixer Integrated with Parylene Microfluidic Channels." *Lab Chip* 4 (6). The Royal Society of Chemistry:608–13. <https://doi.org/10.1039/B403305A>.
- Samiei, Ehsan, Maryam Tabrizian, and Mina Hoorfar. 2016. "A Review of Digital Microfluidics as Portable Platforms for Lab-on a-Chip Applications." *Lab on a Chip* 16. Royal Society of Chemistry:2376–96. <https://doi.org/10.1039/C6LC00387G>.
- Sciencetech™. 2017. "Sciencetech Laboratory Balance SA-80." 2017. <http://balance.balances.com/scales/23>.
- Shah, R K, and A L London. 1978. "PREFACE BT - Laminar Flow Forced Convection in Ducts." In , 197–200. Academic Press. <https://doi.org/http://dx.doi.org/10.1016/B978-0-12-020051-1.50005-X>.
- Sigma-Aldrich. 2017. "Microreactor Explorer Kit." 2017. <http://www.sigmaaldrich.com/chemistry/chemical-synthesis/technology-spotlights/microreactor-explorer-kit/kit-19979.html>.
- Sigma-Aldrich™. 2017. "Poly(glycidyl Methacrylate)." 2017. <http://www.sigmaaldrich.com/catalog/product/aldrich/705314?lang=pt&region=PT>.
- Silverio, Vania, and Susana Cardoso De Freitas. 2017. *Complex Fluid-Flows in Microfluidics*. Edited by Francisco José Galindo-Rosales. *Complex Fluid-Flows in Microfluidics*. 1sted. Porto: Springer International Publishing. <https://doi.org/10.1007/978-3-319-59593-1>.
- Spiegelaere, Ward De, Christophe Casteleyn, Wim Van den Broeck, Johanna Plendl, Mahtab Bahramsoltani, Paul Simoens, Valentin Djonov, and Pieter Cornillie. 2012. "Intussusceptive Angiogenesis: A Biologically Relevant Form of Angiogenesis." *Journal of Vascular Research* 49 (5). Switzerland:390–404. <https://doi.org/10.1159/000338278>.
- SterliTech™. 2017. "POLYESTER (PETE) MEMBRANE FILTERS, 0.4 MICRON, 13MM, 100/PK." 2017. <https://www.sterlitech.com/polyester-membrane-filter-pet0413100.html>.
- Stetten, Felix Von, Daniel Mark, and Stefan Haeberle. 2010. "Microfluidic Lab-on-a-Chip Platforms: Requirements, Characteristics and Applications." *Chemical Society Reviews*, no. 3. <https://doi.org/10.1039/b820557b>.
- Stuart™. 2017. "Hotplate 16x16cm, Digital, SD160." 2017. <http://www.stuart-equipment.com/product.asp?dsl=94>.
- SyringePump.com™. 2017. "Syringe Pump NE-300 Just Infusion." 2017. <https://www.syringepump.com/NE-300.php>.
- Tabeling, Patrick. 2005. *Introduction to Microfluidics*. Paris: Oxford University Press.
- Temiz, Yuksel, Robert D Lovchik, Govind V Kaigala, and Emmanuel Delamarche. 2015. "Microelectronic Engineering Lab-on-a-Chip Devices: How to Close and Plug the Lab?" *MICROELECTRONIC ENGINEERING* 132. Elsevier B.V.:156–75. <https://doi.org/10.1016/j.mee.2014.10.013>.
- Tenkor™. 2015. "Profilometer - Tencor Alpha Step 200." 2015. <https://www.buffalo.edu/shared-facilities-equip/facilities-equipment/SearchEquipment.host.html/content/shared/www/shared-facilities-equip/equipment-list/ProfilometerTencorAlphaStep200Metrology.detail.html>.
- Theodoros, Papaioannou, and Stefanadis Christodoulos. 2005. "Vascular Wall Shear Stress: Basic Principles and Methods." *Hellenic Journal of Cardiology*, 9–15.
- Tkachenko, Eugene, Edgar Gutierrez, Mark H. Ginsberg, and Alex Groisman. 2009. "An Easy to Assemble Microfluidic Perfusion Device with a Magnetic Clamp." *Lab on a Chip* 9 (8):1085. <https://doi.org/10.1039/b812184b>.
- Tortora, Gerard J., and Bryan Derrickson. 2010. *Introduction to the Human Body, the Essentials of Anatomy and Physiology*. 8thed. New York: John Wiley & Sons, Inc.
- UV-light Technology™. 2017. "UV 800W Curing Flood Lamp." 2017.
- Veleri, Shobi, Csilla H Lazar, Bo Chang, Paul A Sieving, Eyal Barin, and Anand Swaroop. 2015. "Biology and Therapy of Inherited Retinal Degenerative Disease: Insights from Mouse Models." *Disease Models and Mechanisms* 8 (2):109–29. <https://doi.org/10.1242/dmm.017913>.
- Venancio-Marques, Anna, Fanny Barbaud, and Damien Baigl. 2013. "Microfluidic Mixing Triggered by

- an External LED Illumination." *Journal of the American Chemical Society* 135 (8):3218–23. <https://doi.org/10.1021/ja311837r>.
- Ward, Kevin, and Z Hugh Fan. 2016. "Mixing in Microfluidic Devices and Enhancement Methods." *Micromechanics and Microengineering* 25 (9):1–33. <https://doi.org/10.1088/0960-1317/25/9/094001>. Mixing.
- Wei-Cheng, Tian, and Erin Finehout. 2009. *Microfluidics for Biological Applications*. Vol. 3. Springer. <https://doi.org/10.1002/0470011149.ch7>.
- White, Frank M. 1991. *Viscous Fluid Flow*. 1sted. Rhode Island: McGraw-Hill Education.
- Witarsa, Albert, and Bruce Finlayson. 2013. "Controlled Diffusion Micromixer." COMSOL.
- Wu, Jing, and Nae Yoon Lee. 2014. "One-Step Surface Modification for Irreversible Bonding of Various Plastics with a Poly(dimethylsiloxane) Elastomer at Room Temperature." *The Royal Society of Chemistry*, 1564–71. <https://doi.org/10.1039/c3lc51324f>.
- Yang, Zhen, and Ryutaro Maeda. 2003. "Socket with Built-in Valves for the Interconnection of Microfluidic Chips to Macro Constituents." *Journal of Chromatography A* 1013 (1–2):29–33. [https://doi.org/10.1016/S0021-9673\(03\)01125-7](https://doi.org/10.1016/S0021-9673(03)01125-7).
- Yield Engineering Systems™. 2017. "YES-310TA." 2017. <http://www.yieldengineering.com/Products/HMDS-Prime-Ovens/TA-Series>.
- Z. Tahergorabi, and M. Khazaei. 2012. "A Review on Angiogenesis and Its Assays." *Iranian Journal of Basic Medical Sciences* 15 (6):1110–26.
- Zhang, Yu Shrike, Julio Aleman, Su Ryon Shin, Tugba Kilic, Duckjin Kim, Seyed Ali Mousavi Shaegh, Solange Massa, et al. 2017. "Multisensor-Integrated Organs-on-Chips Platform for Automated and Continual in Situ Monitoring of Organoid Behaviors." *Proceedings of the National Academy of Sciences of the United States of America* 114 (12). United States:E2293–2302. <https://doi.org/10.1073/pnas.1612906114>.



## A. Annexes

### Group Photo



*Figure A.1 – INESC-MN group picture taken in 2017-10-23.*

## Results and Discussion

Table A.1 – Diffusion coefficient computation of water and VEGF-A molecules.

Molecule	Water	VEGF-A
Length [–]	-	232 a.a.
Mass [Da]	18	27042
Diameter [nm]	0,096	4,240
Diffusion Coefficient [m <sup>2</sup> .s <sup>-1</sup> ] × 10 <sup>-11</sup>	236,4	5,35

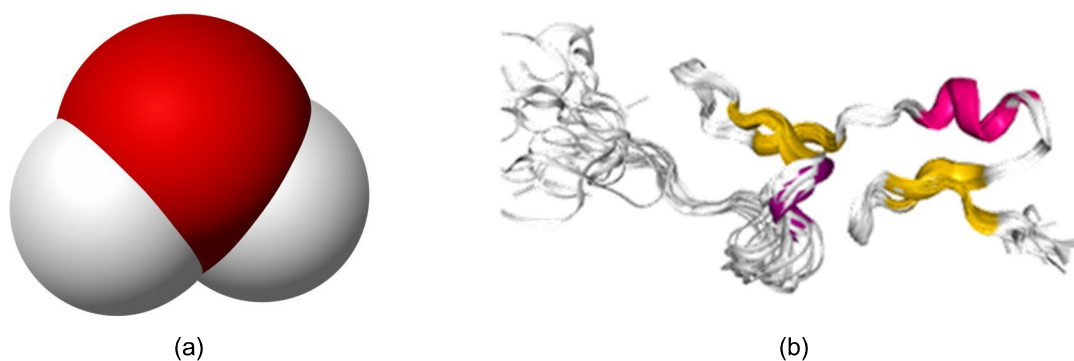


Figure A.2 – 3D representation of water and VEGF-A molecules.

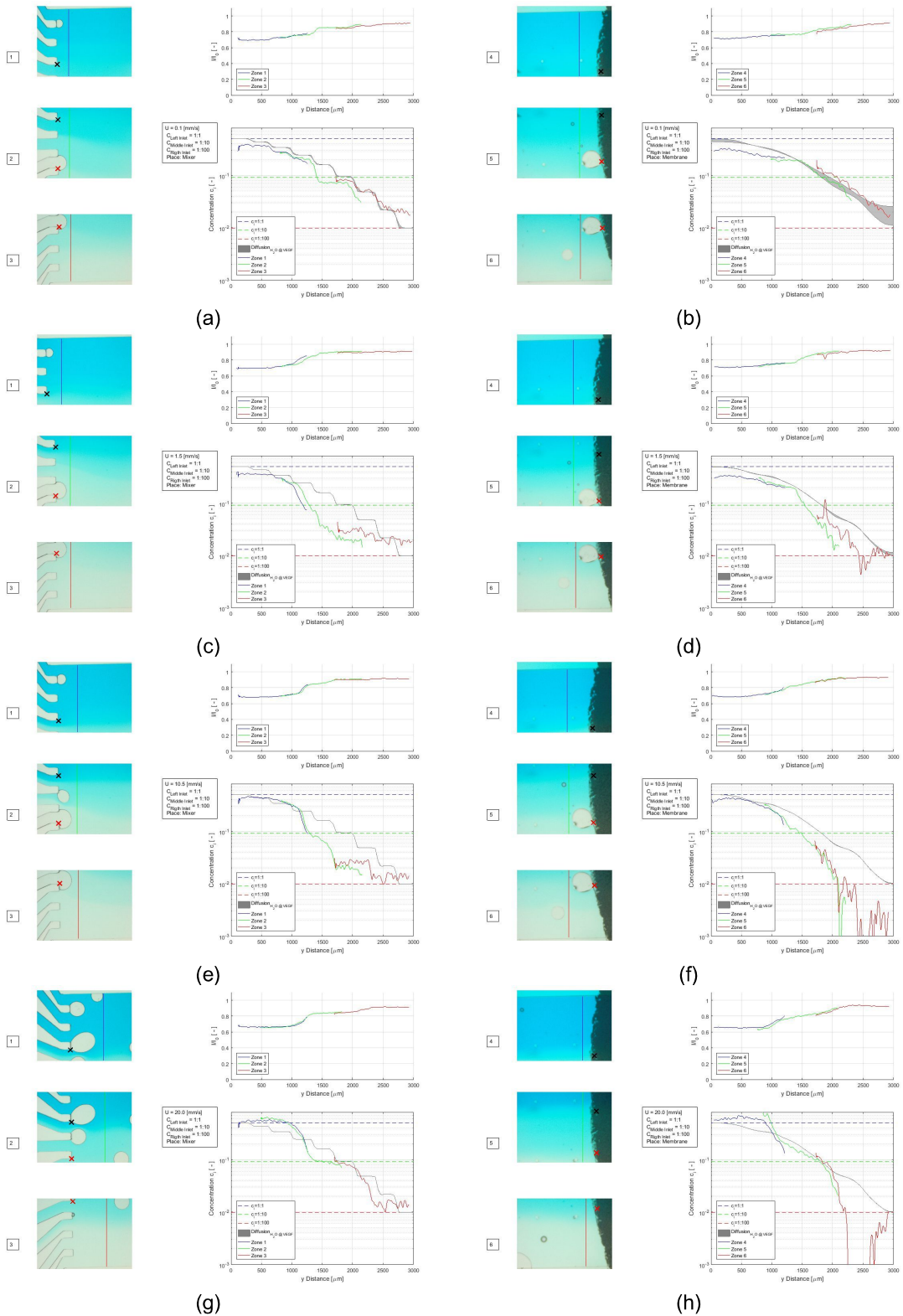


Figure A.3 – Concentration gradient determination in the mixer based on the relative light intensity for an inlet with concentration (Left Inlet 1:1 | Middle Inlet 1:10 | Right Inlet 1:100). Parametrization on velocity from top to bottom ( $U = \{0.1; 1.5; 10.5; 20.0\} mm.s^{-1}$ ). Measurement taken at mixer exit and membrane entrance, respectively left and right images.

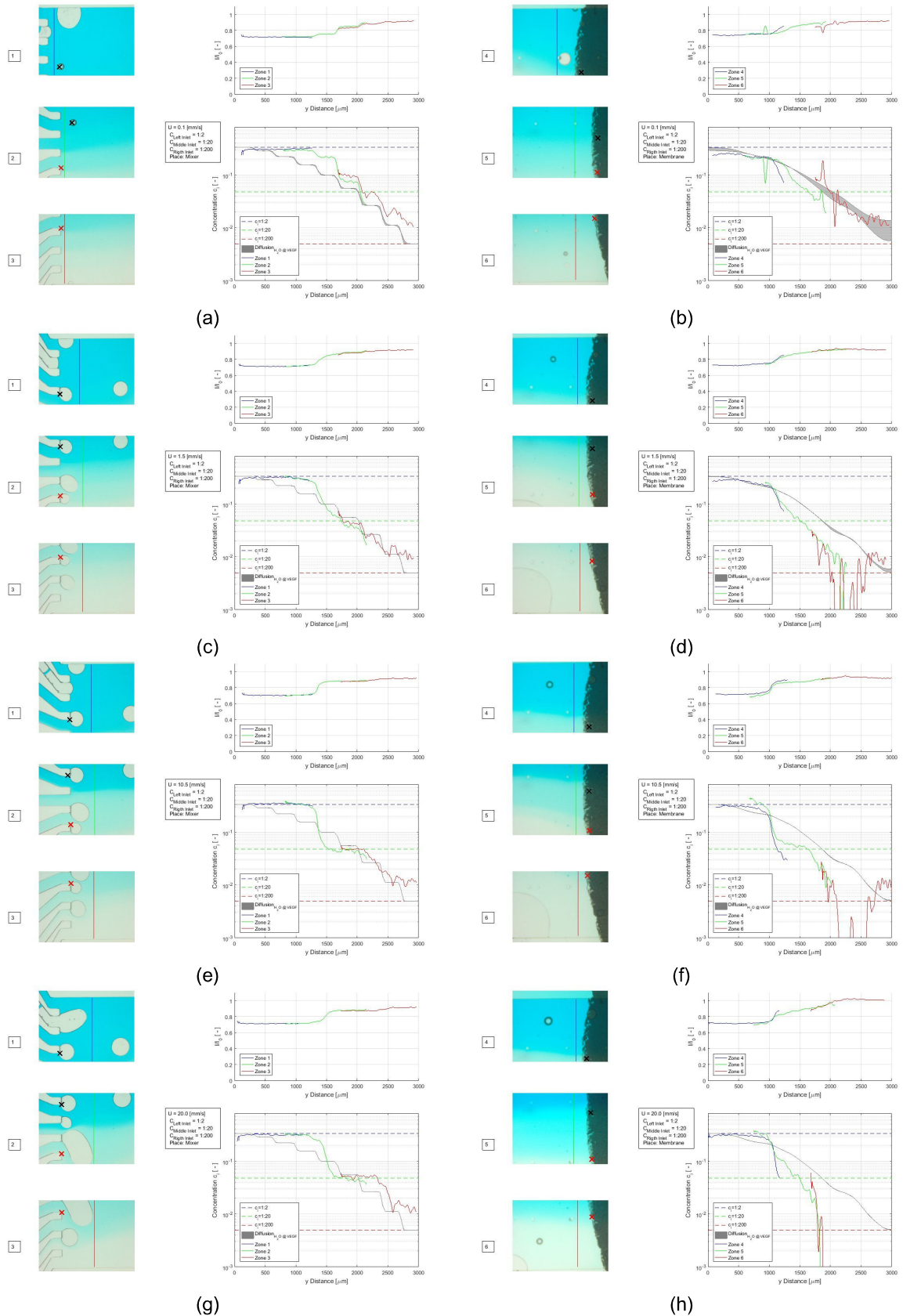


Figure A.4 – Concentration gradient determination in the mixer based on the relative light intensity for an inlet with concentration (Left Inlet 1:2 | Middle Inlet 1:20 | Right Inlet 1:200). Parametrization on velocity from top to bottom ( $U = \{0.1; 1.5; 10.5; 20.0\} \text{ mm.s}^{-1}$ ). Measurement taken at mixer exit and membrane entrance, respectively left and right images.